The Energy Capture Analysis of a Cylindrical Wave Energy Converter

By

Mohamed Hariri Nokob

A Thesis Presented to the
Masdar Institute of Science and Technology
in Partial Fulfillment of the Requirements for the Degree of
Master of Science
in
Mechanical Engineering

AUTHOR'S DECLARATION

I understand that copyright in my thesis is transferred to Masdar Institute of Science and Technology.

ACCEPTANCE DECLARATION

This thesis has been accepted and approved by Masdar Institute of Science and Technology on January 01, 2011.

EXAMINATION COMMITTEE MEMBERS

Youssef Shatilla, Committee Chair, Masdar Institute of Science and Technology
Dick K.-P. Yue, Co-Advisor, Massachusetts Institute of Technology
Peter Armstrong, Masdar Institute of Science and Technology
Mohamed Mekias, Masdar Institute of Science and Technology

Abstract

The field of ocean wave energy is very diverse in terms of design. It is the purpose of this work to model the energy conversion characteristics of a circular cylinder set to oscillate in gentle ocean waves. A semi-analytical eigenfunction expansion method is used to compute the hydrodynamic forces on the body. The fluid potentials and normal velocities are matched at the boundary separating the internal region beneath the floating cylinder (or above it if the cylinder is submerged) and the external region which includes the rest of the fluid.

Three different configurations will be considered. The first is the case of a buoy that is constrained to oscillate in heave by a concentric pole fixed to the seafloor. The pole can be used to lower the buoy during a storm or can be the tower of an offshore wind turbine. Results in monochromatic waves shed light on the effect of the pole size on the hydrodynamic forces acting on the cylinder and on the power output of a linear power takeoff mechanism. The power output from irregular stochastic sea waves is also discussed. The results show that the effect of the pole is to increase the power output at high frequencies. Furthermore, the same power output can be achieved at some frequency for a given pole size by choosing the appropriate buoy size. In irregular waves, numerical results presented for the power indicate that the pole can be advantageous for certain geometries. An increased power per unit mass is also observed. The results can be used to design the buoy to achieve optimum performance.

The second configuration to be discussed is the case of a cable-moored buoy set to oscillate in the vertical plane. Again a linear model is used to assess the power output from regular and irregular waves. Power is extracted from both the heave and pitch modes while particular attention is given to the effect of the pitch mode and to help answer the question of how beneficial it maybe to employ the added degrees of freedom. The results show that the share of pitch power is most notable at high frequencies when the heave power decreases sharply. The results also highlight the effects of some parameters such as the buoy radius, height and floatation level on the power output. The

power per unit mass in irregular waves (directly related to cost) is found to admit a maximum at a fixed buoy height-to-radius ratio.

The third configuration of interest is the case when the sea bottom-mounted cylinder is completely submerged with water. This is a simplified model of the so called Archimedes Wave Swing device used to extract wave energy. The work studies the effect of an added internal mass-spring system on the general performance of the device. The idea is to make the exterior cover of the device almost stationary to protect from wear while moving all the energy to the internal mass. The results show the difficulty of achieving that goal and therefore the ineffectiveness of the idea.

Finally, the work tackles some of the numerical aspects of the problems at hand; mainly the speed of convergence of the Fourier series and how to make use of the Richardson Extrapolation method to speed convergence. A general comparison of the three configurations and conclusions are included.

This research was supported by the Government of Abu Dhabi to help fulfill the vision of the late President Sheikh Zayed Bin Sultan Al Nayhan for sustainable development and empowerment of the UAE and humankind

Acknowledgments

I would like to show my sincere gratitude for my thesis supervisor Professor Youssef Shatilla for his continuous support and care. You have been most generous to accept me as your student.

I would like to extend my gratitude to Professor Dick Yue at MIT. It has been a very enriching experience and a very exciting time of my life to be working under your supervision. Your valuable comments changed the way I look at things and shaped this dissertation to what it is today.

I have a special thanks to Professor Ali Tabaei who supervised the initial stages of my work. You helped me get started and you left a deep impact in my life. To that, I am truly grateful.

I would also like to thank my committee member Professor Peter Armstrong and Dr. Mohamed Mekias for their help and support. I also thank Dr. Mohammad-Reza Alam who reviewed part of the derivations presented here.

I definitely have to thank my parents for paving the road for me to reach this far. Finally I thank all my friends and colleagues for the wonderful experience I had here at Masdar Institute.

Table of Contents

List of Figures

List of Tables

Nomenclature

a: Radius of wave energy converter

A_n, A_n^*: Fourier coefficients

b: Pole radius

B: Buoyancy force

B_{ij}: Radiation damping coefficient

$\mathbf{B^a}$: Damping matrix

c: Power takeoff damping

C_{nk}: Coupling coefficient

$\mathbf{C}$: Stiffness matrix

d: floatation level

D: Depth function

E: Wave power spectrum

E_N^{5j}: Error term

f: Dimensionless diffraction force

F_i^D: Diffraction force

$\mathbf{F}$: External force vector

g: Acceleration of gravity

h: Water depth

H: Height of wave energy converter

H_s: Significant wave height

$I_{xx} + I_{zz}$: Mass moment of inertia

I_x^A: 1st moment of area about x-axis

I_{xx}^A: 2nd moment of area about y-axis

I_z^V: 1st moment of volume about z-axis

J: Energy flux

k_i: Spring constant

$\mathbf{K}$: System matrix

l_i: Displacement constraint

m_0: Wavenumber of incident wave

m_k: Wavenumber of evanescent mode

M: Mass of wave energy converter

M_{ij}: Radiation added mass coefficient

$\mathbf{M}$: Mass matrix

$\mathbf{M^a}$: Added mass matrix

p: pressure

P: Power output from regular waves

P_t: Total power from irregular waves

r: Radial coordinate

R_k: External potential radial modal function

S: Buoyancy per unit displacement

t: time coordinate

T_b: Bottom torque

T_e: Energy period

T_s: Side torque

u: Body velocity

U: Body displacement

v: Dimensionless frequency squared

v_p: Dimensionless peak frequency squared

V_s: Shallow water velocity

W: Capture width

x: Wave direction coordinate

x_m, z_m: Center of mass coordinates

z: Vertical coordinate

Z_k: External potential vertical modal function

Greek symbols

α_n, α_n^*: Fourier coefficients

δ: Dimensionless initial displacement

Δ: Initial displacement

ε_{pn}: Combined Jacobi functions

ϵ_p: Jacobi symbol

ζ: Surface displacement

ζ_0: Incident wave amplitude

η_0^A: Dimensionless buoyancy coefficient

η_i: Dimensionless spring constant

$\eta_{xx} + \eta_{zz}$: Dimensionless mass moment of inertia

η_{xx}^A: Dimensionless 1st area moment

η_z^V: Dimensionless 1st volume moment

θ: Angular coordinate

λ_k: Eigenvalue

λ_c, λ_i: Dimensionless Power takeoff damping

λ_{ij}: Dimensionless damping coefficient

Λ_N^{5j}: Conversion Test function

μ: Dimensionless body mass

μ_{ij}: Dimensionless added mass

ξ_k: Internal potential vertical modal function

ρ: Water density

σ: Dimensionless diffraction force

ς: Dimensionless displacement

ς_m: Dimensionless mass center coordinate

Σ_N^{5j}: Richardson Extrapolate error

ϕ: Velocity potential

ϕ^I: Incident wave potential

ϕ^s: Scattered wave potential

ϕ^r: Radiated wave potential

ϕ_i: Internal region potential

ϕ_e: External region potential

ϕ_h: Homogeneous potential

ϕ_p: Particular potential

χ: Body specific gravity

χ_M: Mass distribution ratio

ψ_k: Internal potential radial modal function

ω: Wave/Oscillation frequency

ω_p: Spectrum peak frequency

Ω_N^{5j}: Richardson Extrapolate

Chapter 1 General Introduction

With the advance of civilization, our need for energy is always on the rise. The problem is that our major current supplies of energy come from fossil fuels which are both non sustainable energy wise and planet wise. Nontraditional resources such as renewable or nuclear sources, therefore, become more attractive to consider. One of the promising renewable technologies is ocean wave energy extraction.

The ocean represents a huge potential of untapped energy. It is estimated that the ocean stores enough energy to meet the demands of the whole world several times [1]. With the highest potential compared to the other ocean energy [2] and even some other renewable technologies [3], ocean wave energy should be seriously developed to meet today's and tomorrow's energy needs. The infancy of the technologies present, as compared to solar or wind, is a strong motive to look into this sustainable eco-friendly solution to our needs.

As Abu Dhabi, through Masdar, aspires to become a leader in the renewable energy field, all renewable resources should be considered. Wave energy is an important field that is gaining interest in Western Europe and more recently in the US. Although the coasts of Abu Dhabi are not very attractive with regards to exploiting their wave resources, researching in the field pushes the country forward towards becoming a knowledge exporting country. Many people are willing to buy this knowledge once available. The moderate resources should not be a drawback to starting any wave projects in Abu Dhabi; in the end, it is the aim of research to develop devices that are economical in places like Abu Dhabi. Assessment of the resources available should be easy as most of the information needed is available from experience with building the breakwaters or from the oil drilling operations offshore. Many of the world coasts have similar wave resources to Abu Dhabi and any breakthrough here will be highly appreciated elsewhere.

1.1 From the Literature

Renewable energy research has so far mainly focused on wind, solar, geothermal and biofuels. The best energy policy must focus on all types of renewable including ocean energy. Energy from the ocean is both clean and abundant. It fits exactly into the definition of renewable and sustainable energy. It is up to us to figure out what is the best way to harness this resource. There are four major forms of energy present in the ocean that are mainly under investigation. These are:

1. Wave energy which represents the energy content in waves that form because of the wind interaction with the surface. Several techniques have been developed to convert it into a more useful form of energy.
2. Tidal energy which represents the potential energy accumulated during the high tide and dissipated during the low tide and which cycles approximately every 12 hours. This increase in potential is then used to drive a hydro-turbine as in the case of traditional hydropower [4]. This technique has the advantage of being highly predictable.
3. Ocean thermal energy which is the use of the temperature gradient across the ocean depth to drive a conventional power cycle. This temperature gradient is usually low but a mere 20° C are enough to drive the cycle. This is accomplished by ocean thermal energy conversion (OTEC) techniques. It is estimated that up to 10000 GW of energy practical to exploit from OTEC is possible offshore in the world's oceans [2].
4. Ocean current energy is that kinetic form present in the motion of the ocean currents. It makes use of this motion to drive turbines similar to wind turbines.

We focus on the first type which also offers the highest potential of available energy [2]. The concept of a wave is simple. A wave is an oscillation in some quantity and how this oscillation propagates. For ocean waves, the oscillation is a feature of the fluid displacement. Crucial to the existence of a wave is the presence of restoring forces. To make an electric oscillator, both a capacitor and an inductor are required to "push" the current back and forth. The inertial and the spring forces of a mechanical oscillator

transfer the energy in between causing the oscillatory behavior of the system. For ocean waves, the restoring force is gravity (hence the name gravity waves) which is literally pushing the fluid against the buoyant force. When these waves initiate at the surface, we call them surface gravity waves or simply surface waves [5]. Surface waves are the main resource used for wave energy conversion.

Ocean waves form as a result of the interaction of wind with the water surface. Therefore, they can be regarded as an indirect form of solar energy. The energy from the sun concentrates in the form of air motion forming wind that has a higher energy potential per unit area than solar. The wind energy then concentrates forming water waves which have an even higher potential. It is this high concentration of energy potential that makes wave energy attractive. More energy can be extracted from a given area which means smaller and less expensive equipment. Ocean waves are also known to be unpredictable in general; a trait carried over from wind. Waves are more consistent than wind though because when the wind stops blowing, waves still surge across the ocean.

The energy in waves is generally measured in terms of power per unit length (kW/m) of wave crest. Sites with annual average values between 20 and 70 kW/m are considered as good deployment places for wave energy projects. Places like western Europe are rich in the wave resource, but places in the southern hemisphere, where lower seasonal variations occur, like South America, Africa or Australia are considered to be the best sites for extracting energy [6].

It is estimated that the power potential that hits the coasts of the world is of the order of 1 TW [7]. Many wave energy converters (WEC's) were proposed to harness this type of energy [6][8]. The highly efficient Salter Duck was the device that triggered interest in ocean wave energy [9]. Its rounded backside limits the formation of transmitted waves, theoretically allowing complete energy extraction. Efficiencies as high as 80% have been achieved in the lab but the performance was not as good in the open ocean. An important category of the devices available is the oscillating water columns which use the difference in air pressure caused by the oscillation of the waves to drive a Wells unidirectional turbine [6]. Many other devices exist as well such as Pelamis which was

the first device to be connected to the grid and the Archimedes Wave Swing (AWS) which has already been implemented on a 2 MW scale. These are exceptions though as wave devices found it difficult to move from the stage of theoretical and numerical modeling to experimentation largely due to difficulty of implementation and lack of funding.

Proper classification of WEC's is essential for design and standardization. In particular, floating WEC's can be classified into three categories: point absorbers, terminators and attenuators. This classification is based on the geometrical scales of the devices and on their orientation with respect to the incoming waves. Terminators and attenuators have one length scale much larger than the other. The difference is that the terminators are oriented perpendicular to the wave propagation blocking the incoming waves while attenuators are oriented parallel to the direction of wave propagation attenuating the wave as it passes along. Point absorbers, which we restrict our focus on, have their length scales much smaller than the wavelength of the incoming waves which makes them seem like a point from the wave perspective [10]. These were first considered by Budal and Falnes in [11]. These are likely to be the most economical among the WEC's [12].

Circular cylindrical buoys form an important category of point absorbers. They are important from a practical point of view and they are an obvious choice for theoretical studies because of their simplicity. These buoys resemble circular platforms in the ocean and use can be made of the analysis done on these platforms. Essential to determine the power extracted by any WEC is to estimate the resulting hydrodynamic forces. These forces result from the interaction with the incoming waves and from the oscillation of the body itself in the fluid. We call these forces the excitation and radiation forces respectively. Linear theory allows solving for these forces separately making the problem much easier to handle. The science of computing these forces is a major track of modern hydrodynamics.

The first type of forces considered results from the body oscillation itself. As the buoy oscillates in the absence of any incident waves, it radiates energy away in the form of waves. Solving for the governing fluid potential in this case is called the radiation

problem and the resulting forces on the body are called the radiation forces. For the buoy considered in this work, the radiation problem has been studied in [13] and [14] using the classical eigenfunction expansion method in the frequency domain. These forces are usually represented in the form of an added mass-acceleration product and a damping coefficient-velocity product in the frequency domain or convolution integrals in the time domain. Numerical methods such as the FEM are usually used to compute these forces for complicated geometries or for fully nonlinear problems [15]. The buoy has also been studied numerically in [16][17] but in general, numerical methods are not as accurate, they require more time and are more difficult to program compared to analytical techniques [18].

The diffraction problem involves the forces on the buoy due to the incoming and scattered waves when the buoy is held stationary. In cases when the body is small in size, diffraction is insignificant and the force component resulting from the scattered waves can be neglected. This is a direct result of the point absorber theory [19]. The remaining component, a result of the incident wave only, is termed the Froude-Krylov force. This is very convenient in situations where it applies as the diffraction problem need not be solved anymore. For a general body, scattered waves must be considered. For the cases presented in this work for example, this was solved analytically in [20][21] and numerically in [22][23] . The general problem of a buoy excited by an incident wave is the result of the superposition of the radiation and diffraction potentials. A dynamic balance of forces on the buoy allows computing the displacements and velocities of the body. The power output relation follows. This has been studied numerically in [24] for infinite water depth.

It is of interest to study cylindrical buoys because of their simple geometries and common usages in ocean technologies. Many variations are possible and a rigorous treatment requires the analysis of each case separately. Particularly for wave energy conversion, these variations may indeed have profound influence on the performance. It is the purpose of this work to study some of these variations when used for power conversion. Different motivations lead to interest in analyzing the cases presented here.

Many WECs, such as the Norwegian heaving buoy [6], employ a spar to support the floating body. This motivates studying the effect of this spar on the power absorption characteristics of the system. In the case we present, the spar can have many usages. It may be a substitute for mooring or could be used to lower the device during a storm. It could be further used to store the power takeoff (PTO) equipment or even more exotically represent the tower of an offshore wind turbine-WEC hybrid system. This will be the motivation for the first case studied in this work.

A body can have up to six independent degrees of freedom in 3D space. For a body lying in a fluid, these are usually termed surge, sway and heave for the translational modes of motion along the three coordinate axes and roll, pitch and yaw for the rotational modes about these axes [19]. For a body symmetric about a vertical axis like a circular cylinder, there is no appreciable difference between the surge and sway motions and between the roll and pitch rotations. In the absence of viscosity, the yaw motion causes no variation in the fluid field and is of no interest. This makes the analysis of these bodies easier as fewer modes have to be considered. For the cylinder in our case, it is interesting to know how much more power can be extracted by employing the added pitch degree of freedom. This motivates the second design considered in this thesis.

The third device of interest is the AWS. It consists of two main submerged parts: the stationary part called the silo and the oscillating part called the floater [10]. The concept is simple; when a wave crest passes over the device, a gas that is trapped inside the silo is compressed as the floater moves down in response to the increased hydrostatic pressure. The reverse happens during a wave trough and the expanding gas pushes the floater upward. This oscillatory motion of the floater is used to run a linear electric generator which produces electricity. The AWS has also been studied thoroughly and in fact a 2 MW prototype has already been tested close to the Portuguese coast [10]. A frequency domain analysis of the device was performed in [25] and then a time domain approach followed in [26]. The experimental results of the device testing can be found in [27]. The AWS is also the first WEC device to employ a linear generator. This has been the subject of a lot of research since its development [28].

For linear problems, the analysis inevitably starts with regular waves; that is, waves propagating with a single frequency. These monochromatic waves are good models to naturally occurring fully developed waves called swells [5]. This consideration, by itself, is not very representative of natural conditions of interest, although it is important from a theoretical standpoint. It is the beauty of linear problems that allows computing the power output from multiple frequencies by simply summing the contributions from each frequency. This condition fails to be the case in nonlinear problems, as the individual waves corresponding to the different frequencies interact to form new waves with new frequencies, which up to the second order, are sums and differences of the individual frequencies [29][30]. That means that new waves are created and the energy available is redistributed among the present waves. This situation may be of importance to wave energy problems because body responses are affected by mooring schemes and natural frequencies of the system may be significantly different from that of the body itself. In fact, resonance, which is the condition when the wave frequency matches the dynamic system natural frequency, may occur at the sum or difference frequency making the linear analysis inadequate.

In linear problems, natural conditions are modeled so that all positive frequencies are permitted, and the concept of a power spectrum becomes handy. A spectrum is similar to a probability density function for the power content of the waves. When the power transfer function (power from unit amplitude monochromatic waves) is weighted by this spectrum and integrated over the frequency range of interest, the total power is obtained. Spectrums are in general directional, which means that the power available depends on the direction of the incident waves. For the axisymmetric cases considered here, directionality is unimportant and need not be considered. Waves that are modeled by some statistical distribution are usually termed irregular waves.

Generally speaking, the forces on the PTOs are nonlinear and their treatment requires a time domain analysis (see [31]). The hydrodynamic forces from linear theory are still used though. For simplicity and to keep our analysis within the frequency domain, the PTOs are modeled by linear translational and rotational dashpots for the heave and pitch modes respectively. The PTO can also be designed to alter the motion of the buoy into a

more suitable manner. This follows from the fact that practical sizes of these buoys tend to have natural frequencies that are higher than those present naturally in the waves. The theory of WEC's requires the near matching of these two frequencies to achieve optimal and economical performance. By proper design, a PTO can be used to lower the natural frequency of a body. Equations of motion, such as those that will be presented in this text, indicate that negative springiness values may be necessary to reach that goal; a result that is not very practical to implement except by elaborate control methods. Control of WEC's is usually called phase control because it forces the oscillation velocity to be in phase with the wave force. Different kinds of control strategies were developed [32]. One important method is called latching because it acts to keep the device stationary in place for a short while and releases it so as to achieve the same phase of oscillation as the wave force. This has been found to be difficult in practice and requires prediction of the wave amplitudes some short while into the future because the system is not causal [19].

The general statement of the problem at hand is to model wave energy extraction devices and to point to the design areas that can make these devices more efficient, cost effective and reliable. The basic WEC element that is considered is a vertical truncated circular cylinder oscillating in water of finite depth. Three different modifications of this basic element are considered. The first is a floating cylinder that oscillates in heave about a fixed pole. The effect of the pole causes changes to the power absorption characteristics of the device and a thorough understanding of its effect is needed. The second modification allows the floating cylinder to move in the heave and pitch modes simultaneously. These two modes are uncoupled, as we will see, and therefore a definite increase of power is expected. The third modification is meant to model the well known Archimedes Wave Swing which is a submerged device. An improvement of the work of the device is thought possible by introducing an internal mass that alters the dynamics as a whole. The device is designed so that its external structure oscillates with minimum amplitude as all the power is moved to the internal mass.

The objective of this work is to study the different designs of wave energy converters mentioned and to form a suitable model that represents them. The model will help understand the physics of wave converters and will aid the designer to choose the most

suitable geometries that best suit his or her requirements. These will usually be to yield the maximum power absorption or the maximum power density. The study will only tackle the mechanical behavior of the devices and will not consider the details of the electric generators or electric distribution systems that are used.

The thesis is divided into this introduction and four main parts. The first part will talk about the buoy supported by the pole and will study the effect of this pole on the hydrodynamics (Chapter 2) and on the power output of the device in regular and irregular waves (Chapter 3). The second part is dedicated to the analysis of the multi degree of freedom system with a special emphasis on the role of the pitch mode on the power extraction. The hydrodynamics of the heave and surge modes are discussed in part one of this work and in the literature. Only the analysis for the pitch mode is presented (Chapter 4). The power output from regular and irregular waves follows (Chapter 5) with a discussion on the role of the pitch mode and its viability as compared to the solely heaving case. The third part will discuss the model of the AWS, the imposed constraints and the power output from regular waves (Chapter 6). A comparison with the floating buoy is also included. The last part will include an account of the numerical aspects of the work that is common to all devices (Chapter 7), and a conclusion that recaps all the work and discusses the advantages of employing each design with a suggestion of possible future work (Chapter 8).

Part 1 The Pole Supported Heaving Buoy

Chapter 2 Hydrodynamics of the Heave Mode

The first wave energy converter (WEC) that will be considered here is a floating buoy oscillating in water of constant depth. The buoy is supported by a fixed concentric pole which restricts the buoy motion to heave. Floating buoys have long been considered for the possibility of extracting energy from waves. Masuda developed navigation buoys that run on wave energy by driving compressed air into a turbine [33]. This was later called the floating oscillating water column (for more information see [6]).

This chapter mainly deals with the analysis of the hydrodynamic problem related to first configuration considered here henceforth referred to as the heaving buoy.

Figure 2-1: A photo of a typical buoy used for meteorological data collection from a company called Marine Data Service

2.1 Problem Description

The buoy that is considered in this work is circular cylindrical in shape with a draft that is shorter than the water depth. The motion is further constrained to heave by employing a circular pole that is concentric with the buoy and that extends to the ocean

bottom (figure 2-2). The pole is used as a fixed mooring that can be used to store the power takeoff and other auxiliary equipment away from the harsh ocean environment. Furthermore, the pole can be a model to the mast of an offshore wind turbine in a wind-wave hybrid system. It can be shown that this arrangement can be reasonably economical [34]. Obviously there are some advantages of employing this pole. The real question is, what is the effect of the pole on the performance of the device and how does it compare with the case when the pole is absent? This chapter and the next will attempt to answer these questions.

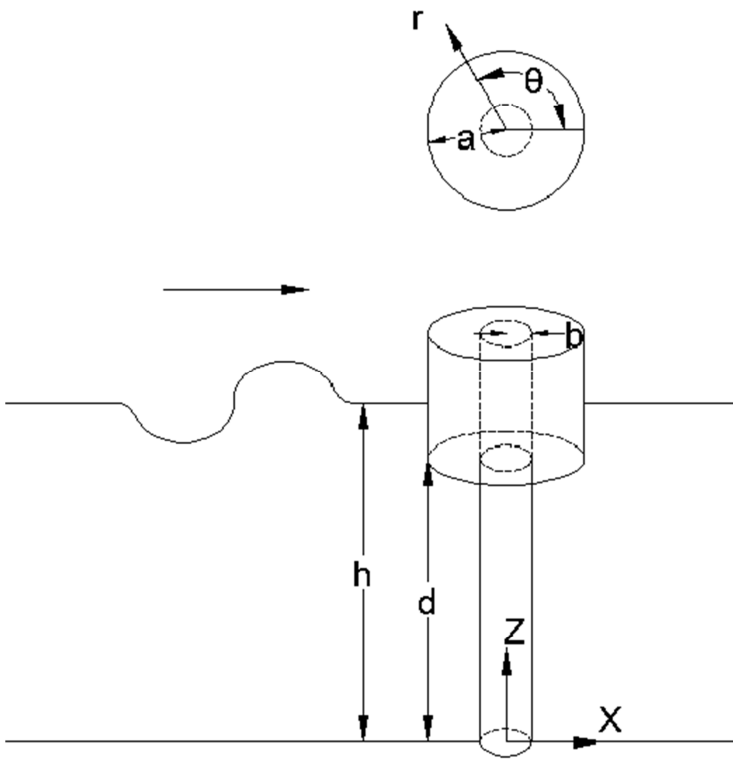

Figure 2-2: Schematic diagram of the buoy-pole system defining the different system parameters and the direction of wave propagation

We would like to estimate the power that can be extracted from such a system or arrangement. To compute the power, the forces on the device and its reaction to the incoming waves must be known. We first make some assumptions that are very common in the study of surface waves to simplify the problem. The fluid is considered to be incompressible and inviscid, which is a good approximation to sea water especially if the speeds involved are small. Furthermore, it follows from the continuity and momentum

equations that if the fluid is irrotational (has a zero vorticity) at an instant, it continues to be so afterwards [19]. That leads us to the assumption that the fluid is irrotational. Friction losses in the mechanisms are also considered to be negligible. To make the problem linear, only small amplitude oscillations and incident waves are considered. The boundary conditions are therefore simple and to a first order approximation, only mean values of the buoy position and the free surface need to be considered. The linearized Bernoulli equation can thus be applied at the surface to lead to a simple free surface condition.

These assumptions enable us to model the flow as a potential flow, that is, the velocity field at any point can be conveniently represented by the gradient of a scalar potential function ϕ. It follows from the continuity equation that ϕ is governed by the Laplace equation. Cylindrical coordinates will be used because of the geometry of the problem.

In the absence of any incident wave and as the buoy oscillates by the action of an external agent, it radiates waves in all directions. Solving for the potential in this case is termed the radiation problem. The result is the radiation potential ϕ^r. It is also governed by Laplace's equation. This potential is important as it leads to the forces on the buoy because of the reaction of the fluid. On the other hand when the buoy is held stationary in the presence of the incoming wave, forces result on the buoy because of the diffraction of the waves and these forces must be absorbed by the supporting agent. They are called the excitation forces. The problem of solving for the potential function is called the diffraction problem. The result is the summation of the incident wave potential ϕ^I (which is known a priori) and the scattered potential ϕ^s. In a real situation, the incident wave is scattered by the presence of the buoy and waves are also radiated because of its oscillatory motion. The resulting potential will therefore include the combined effects of both radiation and diffraction. However, since the problem is linear, the total potential is just the summation of the individual potentials:

$$\phi = \phi^I + \phi^s + \phi^r \,. \tag{2.1}$$

This fact makes the problem easier to handle as each potential can be solved for separately. We further assume that the velocity potential ϕ varies sinusoidally with time

as $\phi = Re\{\hat{\phi}(r,z,\theta)e^{-i\omega t}\}$ and we non-dimensionalize length parameters using the depth h such that:

$$\bar{r} = \frac{r}{h}\,, \bar{z} = \frac{z}{h}, \bar{a} = \frac{a}{h}\,, \bar{d} = \frac{d}{h}\,, \bar{b} = \frac{b}{h},$$

and the complex potential amplitude using frequency

$$\hat{\bar{\phi}} = \frac{\hat{\phi}}{h^2\omega}.$$

The velocity of the buoy is therefore sinusoidal as well and is given by:

$$\bar{u} = Re\left\{\frac{\hat{u}}{h\omega}e^{-i\omega t}\right\} = Re\{\hat{\bar{u}}e^{-i\omega t}\}.$$

The over bars will be dropped hereafter. For both the radiation and diffraction problems, the potential amplitude function can be separated into two regions, the first for $r > a$ (the exterior region) and the other one below the cylinder for $b < r < a$ (the interior region). The two resulting potentials are denoted by $\hat{\phi}_e$ and $\hat{\phi}_i$ respectively. Separation of variables is used to solve for these two functions.

The incident wave is assumed to be unidirectional propagating in the positive x direction. The corresponding free surface displacement can be represented by (see [35] for a derivation):

$$\zeta = \zeta_0 e^{im_0 x} = \zeta_0 \sum_{p=0}^{\infty} \epsilon_p i^p J_p(m_0 r)cos(p\theta)\,. \tag{2.2}$$

Here ζ_0 is the constant wave amplitude, m_0 is the wavenumber and ϵ_p is the Jacobi symbol defined to be 1 for $p = 0$ and 2 for $p > 0$. The Laplace equation:

$$\frac{\partial^2\hat{\phi}}{\partial r^2} + \frac{1}{r}\frac{\partial\hat{\phi}}{\partial r} + \frac{\partial^2\hat{\phi}}{\partial z^2} + \frac{1}{r^2}\frac{\partial^2\hat{\phi}}{\partial\theta^2} = 0\,, \tag{2.3}$$

applies with the last term dropped for the axisymmetric radiation problem. The boundary conditions needed include the linear free surface condition

$$\left.\frac{\partial\hat{\phi}}{\partial z}-\frac{\omega^2 h}{g}\hat{\phi}\right|_{z=1}=0\,, \tag{2.4}$$

which is the combination of the two kinematic and dynamic conditions required to model the surface [5]. This condition is applied at the average surface position at $z=1$ as the displacement is considered to be negligibly small and a first order approximation will suffice. The no flux conditions state that no fluid can penetrate the floating body, the pole or the bottom surface of the ocean:

$$\left.\frac{\partial\hat{\phi}}{\partial z}\right|_{z=0}=0\,, \tag{2.5}$$

$$\left.\frac{\partial\hat{\phi}}{\partial r}\right|_{r=a}=0\quad(d\le z\le 1), \tag{2.6}$$

$$\left.\frac{\partial\hat{\phi}}{\partial r}\right|_{r=b}=0\quad(0\le z\le d). \tag{2.7}$$

Slipping (nonzero velocities tangent to the body surfaces) is allowed in our model since viscosity is considered negligible. In the normal direction, the velocity of the fluid must be the same as that of the buoy so the condition on the buoy bottom must be:

$$\left.\frac{\partial\hat{\phi}}{\partial z}\right|_{z=d}=\hat{u}. \tag{2.8}$$

This velocity is set to zero for the diffraction problem. Finally, both problems must satisfy the radiation condition at infinity. This is the condition that waves must radiate in the direction away from the body (outgoing waves) and not into the body. For our problem, it can be represented formally by the requirement that [5]:

$$\lim_{r\to\infty}\frac{1}{\sqrt{m_0 r}}\left(\frac{\partial\hat{\phi}}{\partial r}-im_0\hat{\phi}\right)=0\,. \tag{2.9}$$

In what follows, we solve for the hydrodynamic coefficients (§2.2) and then for the excitation force (§2.3).

2.2 The Heave Radiation Problem

First, let us consider the radiation problem. This problem is axisymmetric which makes it easier to solve as compared to the scattering problem. This is the situation when the buoy oscillates in the water while there is no incoming wave intervention. As the buoy oscillates, it radiates (creates) waves. These waves are energy carriers and therefore the process is that of transferring the energy of the buoy away from the system and distributing it throughout the fluid. No viscous dissipation is assumed to be present and therefore all energy is lost by radiation. To make the analysis simpler, the buoy is assumed to oscillate with small amplitude. This assumption allows average values to be used for the position of the body. The errors are insignificant. Potential theory is applicable and the equations to solve are the Laplace equation and Bernoulli's equation.

The question to ask at this point is how much and in what way does this pole affect the radiation forces on the cylindrical body. The aim now is to solve the boundary value problem defined by (2.3-9).

2.2.1 Theory

As was mentioned before, the potential amplitude function is separated into exterior and interior regions and the two resulting potentials are denoted by $\hat{\phi}_e$ and $\hat{\phi}_i$ respectively. Each of the two potentials is governed by equation (2.3) (after losing the θ dependence term). Furthermore, $\hat{\phi}_i$ satisfies conditions (2.5, 7, 8) and

$$\hat{\phi}_i\big|_{r=a} = \hat{\phi}_e\big|_{r=a}\,, \tag{2.10}$$

while $\hat{\phi}_e$ must satisfy (2.4-6, 2.9) and

$$\left.\frac{\partial \hat{\phi}_e}{\partial r}\right|_{r=a} = \left.\frac{\partial \hat{\phi}_i}{\partial r}\right|_{r=a} \quad (0 \le z \le d)\,. \tag{2.11}$$

$\hat{\phi}_i$ has to satisfy one inhomogeneous condition (2.8). It can therefore be expressed as the sum of a homogeneous solution $\hat{\phi}_h$ and a particular solution $\hat{\phi}_p$ such that:

$$\hat{\phi}_i = \hat{\phi}_h + \hat{\phi}_p \,. \tag{2.12}$$

Both these potentials satisfy the Laplace equation (2.3) and the following boundary conditions. Starting with $\hat{\phi}_p$:

$$\left.\frac{\partial \hat{\phi}_p}{\partial z}\right|_{z=0} = 0 \,, \tag{2.13}$$

$$\left.\frac{\partial \hat{\phi}_p}{\partial r}\right|_{r=b} = 0 \,, \tag{2.14}$$

$$\left.\frac{\partial \hat{\phi}_p}{\partial z}\right|_{z=d} = \hat{u}_b \,, \tag{2.15}$$

and $\hat{\phi}_h$ must satisfy:

$$\left.\frac{\partial \hat{\phi}_h}{\partial z}\right|_{z=0\ \&\ d} = 0 \,, \tag{2.16}$$

$$\left.\frac{\partial \hat{\phi}_h}{\partial r}\right|_{r=b} = 0 \,, \tag{2.17}$$

$$\hat{\phi}_h\big|_{r=a} = \left(\hat{\phi}_e - \hat{\phi}_p\right)\big|_{r=a} \,. \tag{2.18}$$

By inserting a trial function of the form $\hat{\phi}_p = Az^2 + Br^2 + C\ln r$ into (2.3) and applying (2.13-15), a particular solution is given by:

$$\hat{\phi}_p = \frac{\hat{u}_b}{2d}\left(z^2 - \frac{r^2}{2} + b^2 \ln r\right). \tag{2.19}$$

Now the homogeneous solution can be solved using the method of separation of the variables. Assume the following form:

$$\hat{\phi}_h = \psi(r)\xi(z) \,. \tag{2.20}$$

Inserting (2.20) into (2.3) and rearranging:

$$\frac{\psi''}{\psi} + \frac{\psi'}{r\psi} = -\frac{\xi''}{\xi}. \tag{2.21}$$

As usual, the right side and the left side are independent and are each equal to a constant λ^2. That is

$$\xi'' + \lambda^2 \xi = 0\,, \tag{2.22}$$

$$r^2\psi'' + r\psi' - \lambda^2 r^2 \psi = 0\,. \tag{2.23}$$

Furthermore, from (2.16), the following conditions must be satisfied:

$$\xi'|_{z=0\,\&\,d} = 0\,. \tag{2.24}$$

This gives a set of solutions or eigenfunctions of the form:

$$\xi_n = \cos(\lambda_n z)\,, \quad (n = 0,1,2\ldots)\,. \tag{2.25}$$

The set of eigenvalues λ_n are given by

$$\lambda_n = \frac{n\pi}{d}\,. \tag{2.26}$$

For $n = 0$ the equation (2.23) becomes:

$$r^2\psi'' + r\psi' = 0\,, \tag{2.27}$$

and the solution of this equation is of the form:

$$\psi_0 = c_1 \ln r + c_2\,. \tag{2.28}$$

For $n \geq 1$, the solution for (2.23) is:

$$\psi_n = AI_0(\lambda_n r) + BK_0(\lambda_n r)\,, \tag{2.29}$$

where I_0 and K_0 are the modified Bessel functions of zero order and of the first and second kinds respectively and A and B are arbitrary constants. From (2.17),

$$\psi'|_{r=b} = 0\,, \tag{2.30}$$

which results in a solution of the form:

$$\psi_n(r) = \begin{cases} 1 & (n = 0)\,, \\ I_0(\lambda_n r) - \dfrac{I'_0(\lambda_n b)}{K'_0(\lambda_n b)} K_0(\lambda_n r) & (n > 0)\,. \end{cases} \tag{2.31}$$

The homogeneous solution now can be written as:

$$\hat{\phi}_h = \sum_{n=0}^{\infty} \alpha_n \frac{\psi_n(r)}{\psi_n(a)} \cos(\lambda_n z)\,. \tag{2.32}$$

Here, α_n are Fourier constants. To solve for these constants, apply (2.18):

$$\hat{\phi}_h\big|_{r=a} = \sum_{n=0}^{\infty} \alpha_n \cos(\lambda_n z) = \left(\hat{\phi}_e - \hat{\phi}_p\right)\big|_{r=a}\,. \tag{2.33}$$

Making use of the orthogonality properties of the cosine functions in (2.33):

$$\begin{aligned} &\sum_{n=1}^{\infty} \alpha_n \int_0^d \cos(\lambda_n z)\cos(\lambda_m z) dz \\ &= \int_0^d \left(\hat{\phi}_e - \hat{\phi}_p\right)\big|_{r=a} \cos(\lambda_m z) dz\,. \end{aligned} \tag{2.34}$$

This simplifies to:

$$\begin{aligned} \alpha_n &= \frac{\epsilon_n}{d} \int_0^d \left(\hat{\phi}_e - \hat{\phi}_p\right)\big|_{r=a} \cos(\lambda_n z)\, dz \\ &= \frac{\epsilon_n}{d} \int_0^d \hat{\phi}_e\big|_{r=a} \cos(\lambda_n z)\, dz - {\alpha_n}^*\,, \end{aligned} \tag{2.35}$$

such that ϵ_n is the Jacobi symbol and,

$${\alpha_n}^* = \frac{\epsilon_n}{d} \int_0^d \hat{\phi}_p\big|_{r=a} \cos(\lambda_n z)\, dz\,. \tag{2.36}$$

Now moving to solve for the external potential function, separation of variables is again to be used:

$$\hat{\phi}_e = R(r)Z(z). \tag{2.37}$$

Substituting (2.37) into (2.3) and taking the constant $(-m^2)$ to be negative this time (both cases yield the same result but it is clearer by taking the constant to be negative) :

$$Z'' - m^2 Z = 0\,, \tag{2.38}$$

$$r^2 R'' + rR' + m^2 r^2 R = 0\,. \tag{2.39}$$

Taking into consideration the boundary condition (2.5), the solution of (2.38) can be written as:

$$Z = A\cosh(mz)\,. \tag{2.40}$$

Applying condition (2.4) yields the following dispersion relation:

$$m\tanh m = \nu\,, \tag{2.41}$$

$$\nu = \frac{\omega^2 h}{g}\,. \tag{2.42}$$

Equation (2.41) has only one real positive solution m_0 and an infinite number of solutions im_k $(k \geq 1)$ that can be solved for numerically. The functions given by (2.40) are orthogonal functions and form a complete set. Since A is arbitrary, it can be chosen to yield a normalized inner product of the functions such that:

$$Z_k(z) = \begin{cases} \dfrac{\cosh(m_0 z)}{\sqrt{N_0}} & N_0 = \dfrac{1}{2} + \dfrac{\sinh(2m_0)}{4m_0} \quad (k = 0)\,, \\ \dfrac{\cos(m_k z)}{\sqrt{N_k}} & N_k = \dfrac{1}{2} + \dfrac{\sin(2m_k)}{4m_k} \quad (k \geq 1)\,, \end{cases} \tag{2.43}$$

$$\int_0^1 Z_k(z) Z_j(z) dz = \delta_{jk}\,, \tag{2.44}$$

where δ_{jk} is the Kronecker delta.

For $k = 0$, (2.39) becomes $r^2 {R_0}'' + r{R_0}' + {m_0}^2 r^2 R_0 = 0$.

For $k \geq 1$, (2.39) becomes $r^2 {R_0}'' + r{R_0}' - {m_k}^2 r^2 R_0 = 0$.

The solution for these equations is given by

$$R_k = \begin{cases} H_0(m_0 r) & (k = 0), \\ K_0(m_k r) & (k > 0), \end{cases} \tag{2.45}$$

where $H_0 = J_0 + iY_0$ is the zeroth order Hankel function of the first kind. It represents the outgoing propagating mode of the external potential. The second linearly independent solution (which is the zero order Hankel function of the second kind) is dropped out in this case since it does not satisfy the radiation condition. $K_0(m_k r)$ is the zeroth order modified Bessel function of the second kind. The second linearly independent solution (which is the zero order modified Bessel function of the first kind) is again dropped out since it is not finite as $r \to \infty$. The solution for the potential of the external region is therefore given by:

$$\hat{\phi}_e = \sum_{k=0}^{\infty} A_k R_k(r) Z_k(z)\,. \tag{2.46}$$

The last equation represents the sum of a propagating wave (the first term $k = 0$) and an infinite number of evanescent waves ($k \geq 1$) that die out with increasing distance. Conditions (2. 6) and (2.11) must be satisfied. That is:

$$\left.\frac{\partial \hat{\phi}_e}{\partial r}\right|_{r=a} = \sum_{k=0}^{\infty} A_k R_k'(a) Z_k(z) = \begin{cases} 0 & (d \leq z \leq 1)\,, \\ \dfrac{\partial \hat{\phi}_i(a,z)}{\partial r} & (0 \leq z \leq d)\,. \end{cases} \tag{2.47}$$

Making use of the orthogonal properties of the Z_k functions:

$$\sum_{k=0}^{\infty} A_k R_k'(a) \int_0^1 Z_k(z) Z_j(z) dz = \int_0^d \left.\frac{\partial \hat{\phi}_i}{\partial r}\right|_{r=a} Z_j(z) dz\,. \tag{2.48}$$

The terms where $k \neq j$ drop out on the left side and what is left is:

$$A_k = \frac{1}{R_k'(a)} \int_0^d \left.\frac{\partial \hat{\phi}_h}{\partial r}\right|_{r=a} Z_k(z) dz + A_k^*\,, \tag{2.49}$$

$$A_k^* = \frac{1}{R_k'(a)} \int_0^d \left.\frac{\partial \hat{\phi}_p}{\partial r}\right|_{r=a} Z_k(z) dz\,. \tag{2.50}$$

Using (2.32), equation (2.49) becomes:

$$A_k = \frac{1}{R_k'(a)} \sum_{n=0}^{\infty} \alpha_n \frac{\psi_n'|_{r=a}}{\psi_n(a)} C_{nk} + A_k^* \,, \tag{2.51}$$

Here the coupling coefficient C_{nk} is given by:

$$C_{nk} = \int_0^d \cos(\lambda_n z)\, Z_k(z) dz \,. \tag{2.52}$$

Now going back to equation (2.35), and inserting the external potential (2.46):

$$\alpha_n = \frac{\epsilon_n}{d} \sum_{k=0}^{\infty} A_k R_k(a)\ C_{nk} - {\alpha_n}^* \,. \tag{2.53}$$

Finally, (2.51) is inserted into (2.53) to yield the system of equations:

$$\alpha_n = \sum_{j=0}^{\infty} e_{nj} \alpha_j \ + g_n \,, \tag{2.54}$$

$$e_{nj} = \frac{\epsilon_n}{d} \sum_{k=0}^{\infty} \frac{\psi_j'|_{r=a}}{\psi_n(a)} \frac{R_k(a)}{R_k'(a)} C_{jk} C_{nk} \,, \tag{2.55}$$

$$g_n = \frac{\epsilon_n}{d} \sum_{k=0}^{\infty} A_k^* R_k(a)\ C_{nk} - {\alpha_n}^* \,. \tag{2.56}$$

This system can be truncated at any number of terms depending on the accuracy of the solutions required. Convergence is treated thoroughly in Chapter 7. This approach is equivalent to a Galerkin method.

2.2.2 Radiation Coefficients

Now the case under consideration involves oscillation in heave only. For unit velocity, the radiation damping B_{33} and added mass M_{33} are given by the integration of the pressure over S, the surface area of the cylinder [13]:

$$\omega M_{33} + i B_{33} = -\omega \rho \iint \hat{\phi} \frac{\partial \hat{\phi}}{\partial n} dS \,. \tag{2.57}$$

The subscript 33 follow from the generalized impedance matrix [19], and it indicates that only heave is considered in this case. Inserting the non-dimensional terms on the right (and dropping the over bars again):

$$\frac{M_{33} + iB_{33}/\omega}{\rho h^3} = -\iint \hat{\phi}\frac{\partial \hat{\phi}}{\partial n} dS\,.$$

Considering the external and internal regions separately, the integral becomes:

$$\frac{M_{33} + iB_{33}/\omega}{\rho h^3} = \int_0^{2\pi}\int_b^a r\hat{\phi}_i(r,d)\frac{\partial \hat{\phi}_i(r,d)}{\partial z} dr d\theta$$
$$- a\int_0^{2\pi}\int_d^1 \hat{\phi}_e(a,z)\frac{\partial \hat{\phi}_e(a,z)}{\partial r} dz d\theta\,.$$

The second integral is identically zero because of boundary condition (2.6). The first integral can be split according to (2.12) and after inserting (2.8):

$$\frac{M_{33} + iB_{33}/\omega}{\pi\rho h^3} = 2\int_b^a r\hat{\phi}_h(r,d)dr + 2\int_b^a r\hat{\phi}_p(r,d)dr\,.$$

Using (2.19) and (2.32), the parameters can be written in dimensionless form as:

$$\mu_{33} + i\lambda_{33} = \frac{2}{a^3}\sum_{n=0}^{\infty}\alpha_n(-1)^n\psi_n^* + \frac{2}{a^3}\sum_{n=0}^{\infty}\alpha_n(-1)^n R_n^*$$
$$+\frac{1}{a^3 d}\left((a^2-b^2)\left(\frac{d^2}{2} - \frac{a^2+3b^2}{8}\right)\right. \qquad (2.58)$$
$$\left. +\frac{b^2}{2}(a^2\ln a - b^2\ln b)\right),$$

$$\psi_n^* = \int_b^a r\frac{\psi_n(r)}{\psi_n(a)}dr\,, \qquad (2.59)$$

where we define:

$$\mu_{33} + i\lambda_{33} = \frac{M_{33} + iB_{33}/\omega}{\pi\rho a^3}. \qquad (2.60)$$

2.2.3 Results and Discussion

A Matlab code was built to solve all the equations at hand. The code computes the roots of the dispersion relationship (2.41) and then solves the system defined by (2.54-56). The solution is the coefficient terms α_n. With these coefficients available, it is possible to evaluate the potential at any point in the fluid. It is therefore possible to compute the velocity field or the displacement field or even the pressure (using the Bernoulli equation) at any point.

The radiation parameters are then computed using (2.58). Following Yeung's example [13], the added mass and damping coefficient are divided by the radius and plotted against the wave number-radius product. The results are shown in the following figures:

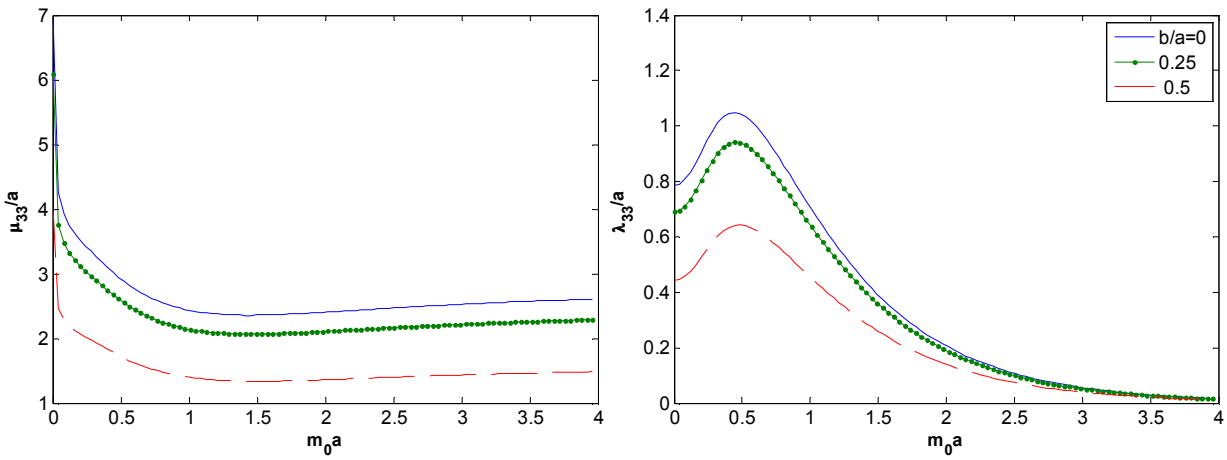

Figure 2-3: The radiation added mass (left) and damping (right) coefficients for the buoy-pole system at $a/h = 0.2$ and $H/a = 0.5$ showing clearly the effect of the pole on the radiation loads on the buoy

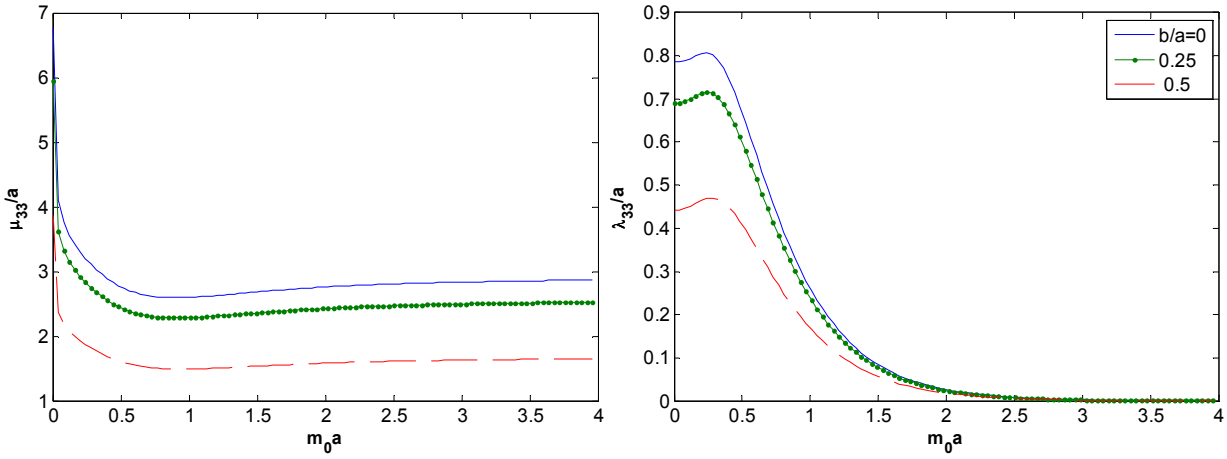

Figure 2-4: The radiation added mass (left) and damping (right) coefficients for the buoy-pole system at $a/h = 0.2$ and $H/a = 1$ showing clearly the effect of the pole on the radiation loads on the buoy

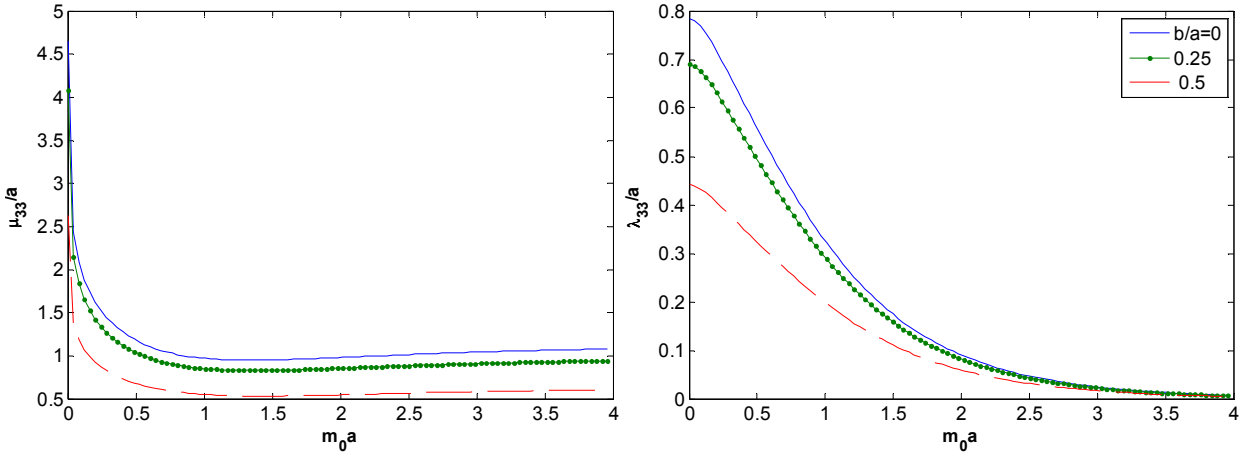

Figure 2-5: The radiation added mass (left) and damping (right) coefficients for the buoy-pole system at $a/h = 0.5$ and $H/a = 0.5$ showing clearly the effect of the pole on the radiation loads on the buoy

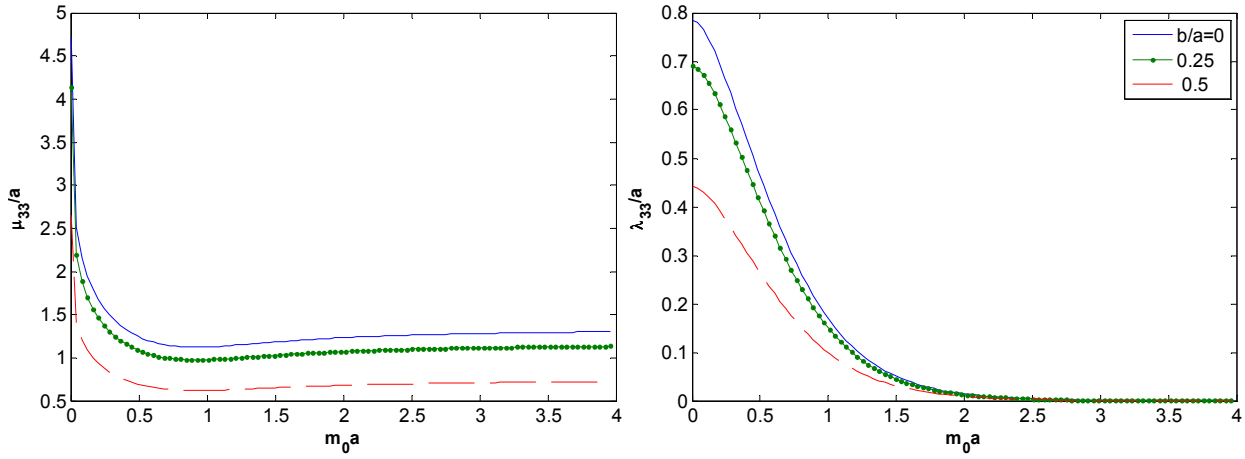

Figure 2-6: The radiation added mass (left) and damping (right) coefficients for the buoy-pole system at $a/h = 0.5$ and $H/a = 1$ showing clearly the effect of the pole on the radiation loads on the buoy

These results are found to match Yeung's results exactly (for the case when $b/a = 0$). This assures the validity of these results. It can be seen from the results that the effect of the pole is to decrease the added mass and the damping coefficient. The larger the radius of the pole compared to the radius of the buoy is, the larger is that effect.

One more point to notice is that the damping coefficient to radius ratio always starts from a fixed value. For $b/a = 0$ for example, it starts from near 0.8 (it will be shown later that this value is actually $\pi/4$ and that the reason for this follows from the Haskind relationship presented in Chapter 3).

2.3 The Heave Diffraction Problem

The diffraction problem can be considered to be the reverse process of the radiation problem. While the latter begins by the oscillation of the body which generates waves that radiate away from the body, the former involves upcoming waves that cause the otherwise stationary body to oscillate. One would therefore expect that the analysis for both case to be similar and in fact it is. The only differences are the different forcing agents and the directionality involved as the incoming wave proceeds in a specific direction. The aim of the diffraction analysis is to get the magnitudes of the forces acting

on the buoy as it is subjected to the incoming wave. This is a crucial part of the design of offshore platforms or wave energy converters. In our case, the force is important in order to calculate the power that can be extracted from the incident wave. The analysis proceeds in the same manner as for the radiation problem. The assumptions are the same.

We saw in the previous section how the presence of the pole decreases the magnitude of the radiation forces on the floating body. This was mainly because of the decreasing bottom area of the buoy. We might assume similar results for all other forces as well. Therefore, does the pole have the same effect in terms of the diffraction forces? This section will help shed some light on that. Again potential theory is applicable and the governing equation is Laplace's.

2.3.1 Theory

Equations (2.3-9) must again be satisfied. The buoy is stationary in this case and the velocity must be set to zero in (2.8). Again the potentials of the external and internal regions are denoted by $\hat{\phi}_e$ and $\hat{\phi}_i$ respectively. Each of these two potentials is governed by equation (2.3). In addition to conditions (2.5, 7), $\hat{\phi}_i$ must satisfy the following boundary conditions:

$$\left.\frac{\partial \hat{\phi}_i}{\partial z}\right|_{z=d} = 0\,, \tag{2.61}$$

$$\left.\frac{\partial \hat{\phi}_i}{\partial \theta}\right|_{\theta=\pi} = 0\,, \tag{2.62}$$

$$\left.\frac{\partial \hat{\phi}_i}{\partial \theta}\right|_{\theta=0} = 0\,, \tag{2.63}$$

$$\hat{\phi}_i\big|_{r=a} = \hat{\phi}_e\big|_{r=a}\,. \tag{2.64}$$

Conditions (2.62, 63) follow from the symmetry of the buoy. The conditions for the potential of the external region are (2.4, 5, and 6) and:

$$\left.\frac{\partial \hat{\phi}_e}{\partial \theta}\right|_{\theta=\pi} = 0\,, \tag{2.65}$$

$$\left.\frac{\partial \hat{\phi}_e}{\partial \theta}\right|_{\theta=0} = 0\,, \tag{2.66}$$

$$\left.\frac{\partial \hat{\phi}_e}{\partial r}\right|_{r=a} = \left.\frac{\partial \hat{\phi}_i}{\partial r}\right|_{r=a} \quad (0 \le z \le d)\,. \tag{2.67}$$

Finally, it must satisfy the radiation condition. The internal potential problem can be solved using separation of variables and, after applying (2.5) and (2.63), the resulting form is:

$$\hat{\phi}_i = \psi(r)\cos(\lambda z)\cos(p\theta)\,. \tag{2.68}$$

From (2.61) and (2.62),

$$\hat{\phi}_{pn} = \psi_{pn}(r)\cos(\lambda_n z)\cos(p\theta), \tag{2.69}$$

$$\lambda_n = \frac{n\pi}{d} \text{ and } p = 0,1,2\ldots. \tag{2.70}$$

The potential is the summation of the resulting potentials in (2.69). Treating each function individually then ψ_{pn} is governed by:

$$r^2\psi''_{pn} + r\psi'_{pn} - \left(\lambda_n{}^2 r^2 + p^2\right)\psi_{pn} = 0\,. \tag{2.71}$$

For $p, n = 0$ only a constant (which can be taken to be 1) satisfies (2.7).

For $n = 0$ and $p \neq 0$ equation (2.71) becomes of the form:

$$r^2\psi''_{p0} + r\psi'_{p0} - p^2\psi_{p0} = 0\,, \tag{2.72}$$

which has the solution:

$$\psi_{p0} = r^p + b^{2p}r^{-p}\,, \tag{2.73}$$

For $n \neq 0$,

$$\psi_{pn} = \lambda_n I_p(\lambda_n r) K_p'(\lambda_n b) - \lambda_n I_p'(\lambda_n b) K_p(\lambda_n r)\,. \tag{2.74}$$

I_p and K_p are the modified Bessel functions of p^{th} order and of the first and second kinds respectively. The solutions presented satisfy (2.7) directly. The internal potential is now given (in a more suitable form) by:

$$\hat{\phi}_i = \zeta_0 \sum_{p=0}^{\infty} \sum_{n=0}^{\infty} \alpha_{pn} \varepsilon_{pn} \frac{\psi_{pn}(r)}{\psi_{pn}(a)} \cos(\lambda_n z) \cos(p\theta). \tag{2.75}$$

Here ε_{pn} is defined as:

$$\varepsilon_{pn} = \frac{\epsilon_p \epsilon_n}{2\pi d}\,. \tag{2.76}$$

Condition (2.64) must be satisfied as well and by using the orthogonality property,

$$\alpha_{pn} = \frac{1}{\zeta_0} \int_0^d \int_0^{2\pi} \hat{\phi}_e\big|_{r=a} \cos(\lambda_n z) \cos(p\theta)\, d\theta dz\,. \tag{2.77}$$

The external potential is the sum of the potentials of the incident wave and the scattered wave. These are given respectively by (following the example in [20]):

$$\hat{\phi}^I = -\zeta_0 \sum_{k=0}^{\infty} \epsilon_k i^{k+1} J_k(m_0 r) \cos(k\theta) \frac{Z_0(z)}{Z_0'(1)}, \tag{2.78}$$

$$\hat{\phi}^s = \zeta_0 \sum_{j=0}^{\infty} \sum_{k=0}^{\infty} A_{kj} R_{kj}(r) \cos(k\theta)\, Z_j(z)\,, \tag{2.79}$$

such that Z_j are given in (2.43) and the wavenumbers m_k are solutions of (2.41). The functions $R_{kj}(r)$ that satisfy the Laplace equation (2.3) and the radiation condition are

$$R_{kj}(r) = \begin{cases} H_k(m_0 r) & j = 0\,, \\ K_k(m_j r) & j > 0\,, \end{cases} \tag{2.80}$$

where H_k and K_k are the k^{th} order first kind Hankel and second kind modified Bessel functions respectively. The external potential is then written in the form:

$$\hat{\phi}_e = -\zeta_0 \sum_{k=0}^{\infty} \epsilon_k i^{k+1} J_k(m_0 r)\cos(k\theta)\frac{Z_0(z)}{Z_0^{'}(1)} + \zeta_0 \sum_{j=0}^{\infty}\sum_{k=0}^{\infty} A_{kj}\cos(k\theta)\frac{R_{kj}(r)}{R_{kj}(a)}Z_j(z)\,. \tag{2.81}$$

The last equation represents the sum of a propagating wave ($j = 0$) and an infinite number of evanescent waves ($j > 0$). The equation also includes the effect of the incident wave which constitutes the source term in this case. Conditions (2.6) and (2.67) must be satisfied. That is:

$$\left.\frac{\partial\hat{\phi}_e}{\partial r}\right|_{r=a} = \left.\frac{\partial\hat{\phi}^I}{\partial r}\right|_{r=a} + \zeta_0 \sum_{j=0}^{\infty}\sum_{k=0}^{\infty} A_{kj}\cos(k\theta)\frac{R_{kj}^{'}(a)}{R_{kj}(a)}Z_j(z) = \begin{cases} 0 & (d \le z \le 1)\,, \\ \dfrac{\partial\hat{\phi}_i(a,z,\theta)}{\partial r} & (0 \le z \le d)\,. \end{cases} \tag{2.82}$$

The unknown coefficients are then given by:

$$A_{kj} + A_{kj}^{*} = \frac{\epsilon_k}{2\pi\zeta_0}\frac{R_{kj}(a)}{R_{kj}^{'}(a)}\int_0^{2\pi}\int_0^{d}\left.\frac{\partial\hat{\phi}_i}{\partial r}\right|_{r=a} Z_j(z)\cos(k\theta)\,dzd\theta\,, \tag{2.83}$$

$$A_{kj}^{*} = \frac{\epsilon_k}{2\pi\zeta_0}\frac{R_{kj}(a)}{R_{kj}^{'}(a)}\int_0^{2\pi}\int_0^{1}\left.\frac{\partial\hat{\phi}^I}{\partial r}\right|_{r=a} Z_j(z)\cos(k\theta)\,dzd\theta\,, \tag{2.84}$$

where ϵ_k is the Jacobi symbol. Now inserting the value of the internal potential function from (2.75) and integrating,

$$A_{kj} + A_{kj}^{*} = \frac{R_{kj}(a)}{R_{kj}^{'}(a)}\sum_{n=0}^{\infty}\varepsilon_{kn}\frac{\psi_{kn}^{'}(a)}{\psi_{kn}(a)}C_{nj}\alpha_{kn}\,. \tag{2.85}$$

The coupling coefficient C_{nj} was defined in (2.52). Inserting the value of the external potential (2.81) into (2.77) and simplifying then,

$$\alpha_{pn} - \alpha_{pn}^{*} = \frac{2\pi}{\epsilon_p}\sum_{j=0}^{\infty} A_{pj}C_{nj}\,, \tag{2.86}$$

$$\alpha_{pn}^{*} = \frac{1}{\zeta_0}\int_0^d \int_0^{2\pi} \hat{\phi}^I\big|_{r=a} \cos(\lambda_n z)\cos(p\theta)\, d\theta dz\,. \tag{2.87}$$

Finally inserting (2.85) into (2.86),

$$\alpha_{pn} = \sum_{l=0}^{\infty} e_{pnl}\alpha_{pl} + g_{pn}\,, \tag{2.88}$$

$$e_{pnl} = \sum_{j=0}^{\infty} \frac{\epsilon_l}{d}\frac{R_{pj}(a)}{R'_{pj}(a)}\frac{\psi'_{pl}(a)}{\psi_{pl}(a)} C_{lj}C_{nj}\,, \tag{2.89}$$

$$g_{pn} = -\frac{2\pi}{\epsilon_p}\sum_{j=0}^{\infty} A_{pj}^{*}C_{nj} + \alpha_{pn}^{*}\,. \tag{2.90}$$

These three equations represent a system of equations in the unknowns α_{pn} to be solved.

2.3.2 Forces on the Cylinder

The dimensional pressure at any point in the fluid is given by the real part of $\hat{p}(r,\theta,z)e^{-i\omega t}$ and $\hat{p}$ is given by Bernoulli's equation as:

$$\frac{\hat{p}}{\rho\omega^2 h^2} = i\hat{\phi}(r,\theta,z)\,, \tag{2.91}$$

where ρ is the density of the fluid. The force in the vertical direction on the buoy is given by the real part of $\hat{F}e^{-i\omega t}$. Here (all terms on the left are dimensional)

$$\begin{aligned}
\frac{\hat{F}^D}{\rho h^4\omega^2} &= -i\int_0^{2\pi}\int_b^a r\hat{\phi}_i(r,d,\theta)dr\, d\theta \\
&= -i\zeta_0\sum_{p=0}^{\infty}\sum_{n=0}^{\infty}\alpha_{pn}\varepsilon_{pn}\cos(\lambda_n d)\int_0^{2\pi}\int_b^a r\frac{\psi_{pn}(r)}{\psi_{pn}(a)}\cos(p\theta)\, dr\, d\theta \\
&= -2i\pi\zeta_0\sum_{n=0}^{\infty}\alpha_{0n}\varepsilon_{0n}\cos(\lambda_n d)\,\psi_n^{*}\,,
\end{aligned} \tag{2.92}$$

and ψ_n^* was defined in (2.59). If the buoyancy force B is taken to be (all parameters dimensional),

$$B = \pi(a^2 - b^2)\zeta_0 \rho g \,, \tag{2.93}$$

then the dimensionless complex force amplitude in the vertical direction is then given by:

$$\frac{\left|\hat{F}^D\right|}{B} = \frac{v}{a^2 - b^2}\left|\sum_{n=0}^{\infty}(-1)^n \alpha_{0n}\frac{\epsilon_n}{2\pi d}\psi_n^*\right|, \tag{2.94}$$

where v is defined in (2.42). Since only α_{0n} are required for the vertical force, then the system (2.88-90) to be solved reduces to:

$$\alpha_{0n} = \sum_{l=0}^{\infty} e_{0nl}\alpha_{0l} + g_{0n} \,, \tag{2.95}$$

$$e_{0nl} = \sum_{j=0}^{\infty} \frac{\epsilon_l}{d}\frac{R_{0j}(a)}{R'_{0j}(a)}\frac{\psi'_{0l}(a)}{\psi_{0l}(a)} C_{lj} C_{nj} \,, \tag{2.96}$$

$$g_{0n} = -2\pi \sum_{j=0}^{\infty} A^*_{0j} C_{nj} + \alpha^*_{0n} \,. \tag{2.97}$$

2.3.3 Results and Discussion

Again a Matlab Code was implemented to solve these equations. The code is used to solve for the roots of the dispersion relation (2.41) and then solves the system of equations defined by (2.95-97). The solution is the coefficients α_{0n}. With these coefficients available, it is possible to evaluate the potential at any point in the fluid. It is therefore possible to compute the velocity field or the displacement field or even the pressure (using the Bernoulli equation) at any point. The vertical force amplitude and phase can then be easily computed from (2.92, 94). The results of the simulation for some selected cases are presented here:

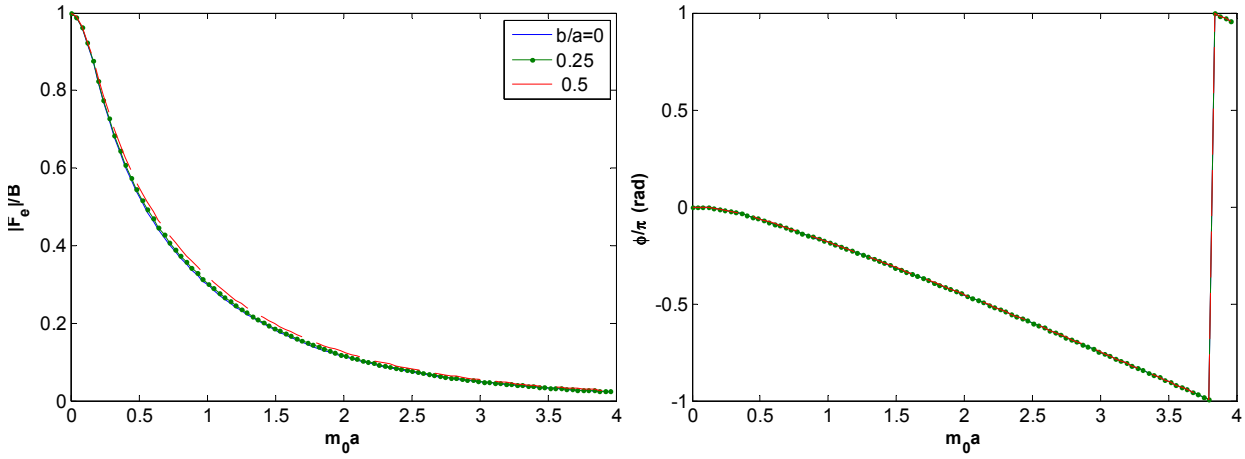

Figure 2-7: The diffraction vertical force amplitude (left) and phase divided by π (right) for the buoy-pole system at $a/h = 0.2$ and $H/a = 0.5$ showing clearly the effect of the pole on the excitation loads on the buoy

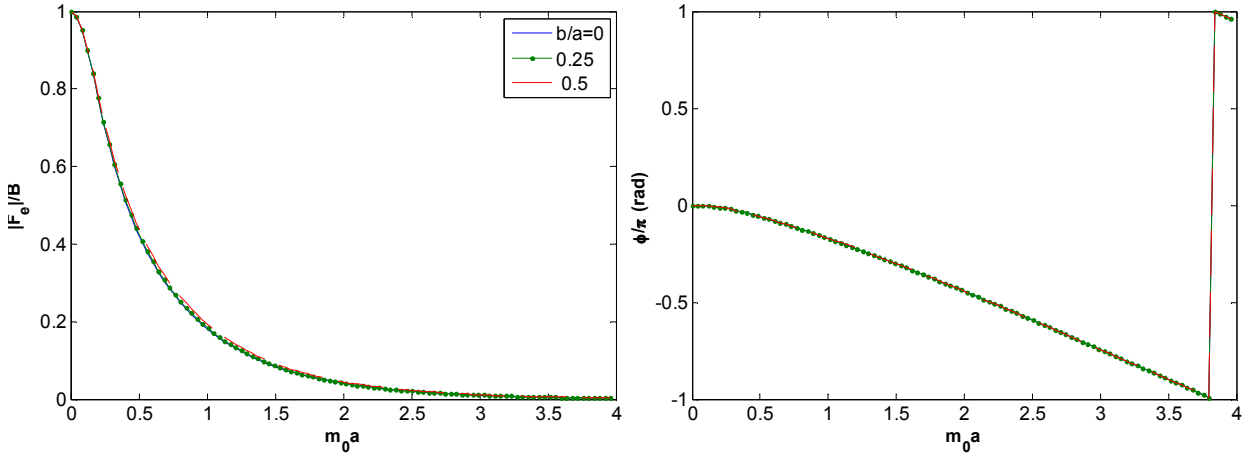

Figure 2-8: The diffraction vertical force amplitude (left) and phase divided by π (right) for the buoy-pole system at $a/h = 0.2$ and $H/a = 1$ showing clearly the effect of the pole on the excitation loads on the buoy

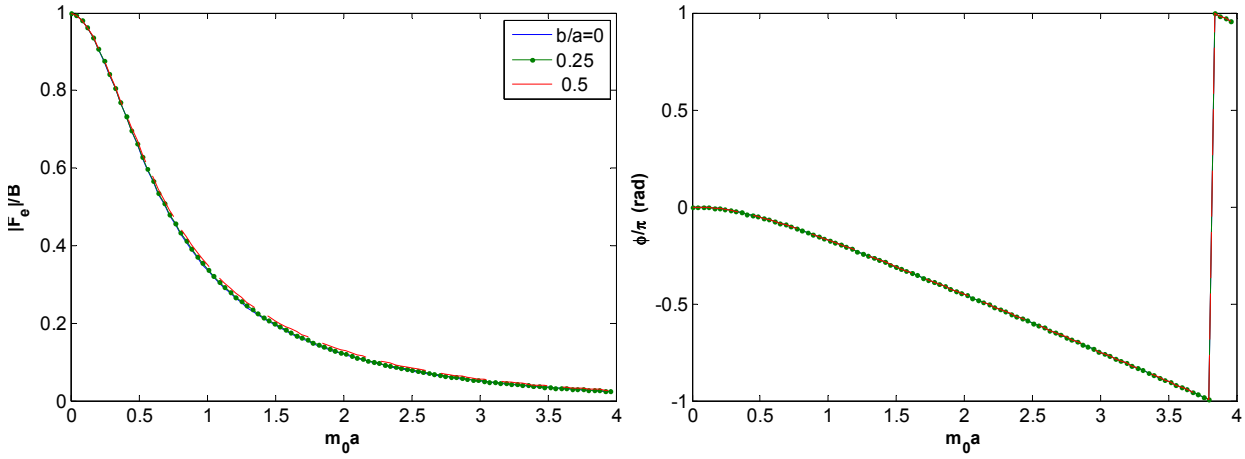

Figure 2-9: The diffraction vertical force amplitude (left) and phase divided by π (right) for the buoy-pole system at $a/h = 0.5$ and $H/a = 0.5$ showing clearly the effect of the pole on the excitation loads on the buoy

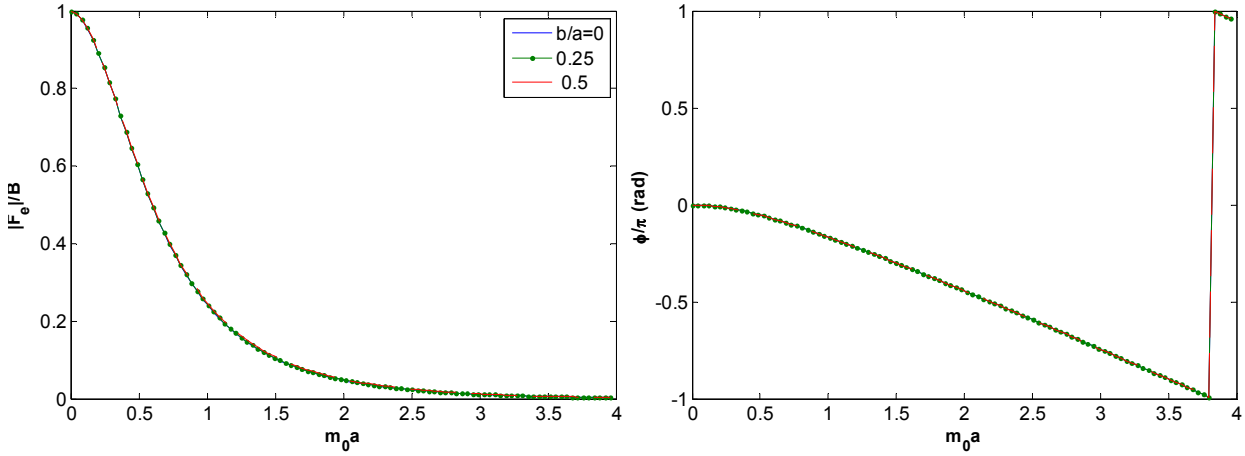

Figure 2-10: The diffraction vertical force amplitude (left) and phase divided by π (right) for the buoy-pole system at $a/h = 0.5$ and $H/a = 1$ showing clearly the effect of the pole on the excitation loads on the buoy

The results for the case when $b/a = 0$ were found to match Garret's results [21] for both the amplitude and the phase. This assures the validity of the approach which is slightly different from the formulation used by that author.

The first point to note about the results is that the force amplitude and phase barely witness any change as the pole radius increases. This does not mean that the forces are the same in that case though because the normalization used is the buoyant force from (2.93) which depends on the pole radius. In fact, the forces are found to decrease as the pole radius increases, especially at the lower frequencies. It is therefore appropriate to

assume that the vertical force on the cylinder, in the pole absence or presence, is of the order of magnitude of the buoyant force at low frequencies reaching almost half the buoyancy at $m_0 a = 0.5$. In fact, the normalized force depends mostly on the frequency with a slight increase for flat buoys at high frequencies. Another point to note is that the force is equal to the buoyant force when the incoming wave has zero frequency. This is to be expected since the incoming wave acts as a step function in this case and the only force acting is the buoyant force. A final conclusion about the force is that it is seen to decrease with frequency to attain an asymptotic limit of zero at high frequencies.

The phase divided by π is plotted in the right hand figures above. An extremely slight change in the phase can be observed for the different b/a ratios considered as well as for the different geometries. This phase starts from zero, which means it is in phase with the incident wave ([19]). It then tends towards $-m_0 a + \frac{1}{4}\pi$ as given by Garret [21] which is for the limiting case of a long cylinder. The phase can be said to depend solely on the frequency of the incoming wave. The jump in the phase value is just to remain within the range of $[-\pi, \pi]$. Otherwise, the curve is completely continuous and continues in the same direction.

2.3.4 The Haskind Relation

Although the work done so far is enough to move to the power analysis, more verification of the results is needed to proceed with confidence. It is here that the Haskind relation comes in to play. The Haskind relation allows calculating the excitation force on the bottom of the buoy from knowledge of the hydrodynamic coefficients. This eliminates the need to solve for the diffraction problem. It can also be used the other way around to get the hydrodynamic coefficients from knowledge of the excitation force.

Up to this point, we compared our work with the work of others and identical results were obtained. However, no link between the results of radiation and diffraction is certain

yet. If the Haskind relation is satisfied, then if either work is correct, the other must be so as well. From [19], the Haskind relation for a heaving body is given by,

$$B_{33} = \frac{\omega k \left|\hat{F}^D\right|^2}{2\rho g^2 D \zeta_0^2}. \tag{2.98}$$

B_{33} is the damping resistance and $|F_e|$ is the amplitude of the excitation force in the vertical direction. Here,

$$D = m_0 h\left(1 - \left(\frac{\omega^2}{g m_0}\right)^2\right) + \frac{\omega^2}{g m_0}, \tag{2.99}$$

is the depth function and in accordance with our previous definitions (§ 2.2) B_{33} is,

$$B_{33} = \pi\omega\rho a^3 \lambda_{33}, \tag{2.100}$$

where λ_{33} is the dimensionless damping coefficient. Therefore,

$$\frac{\left|\hat{F}^D\right|^2}{\pi^2 a^4 \zeta_0^2 \rho^2 g^2} = \frac{2\lambda_{33}}{\pi\bar{a}}\left(1 - \frac{v^2}{{m_0}^2 h^2} + \frac{v}{{m_0}^2 h^2}\right), \tag{2.101}$$

and using $v = m_0 h \tanh(m_0 h)$ from the dispersion relationship (2.41), then

$$\frac{\left|\hat{F}^D\right|^2}{B^2} = \frac{\bar{a}}{\bar{a}^2 - \bar{b}^2}\frac{2\lambda_{33}}{\pi}\left(1 - \tanh(m_0 h)^2 + \frac{\tanh(m_0 h)}{m_0 h}\right). \tag{2.102}$$

Once verified, this relation can be used in our code to compute the excitation force directly with the radiation analysis which would save much of the computational effort (especially later on). In fact, the results produced from this relation were seen to match those from the diffraction problem. We can be sure now that our work is fine.

An interesting point to notice about the relation is that it explains the behavior noted previously for the damping coefficient to radius ratio. The ratio was found to start from $\pi/4$ when $b/a = 0$ and less than that as the latter increases. This applies to all geometries. Equation (2.102) can also be written as:

$$\frac{\left|\hat{F}^D\right|^2}{B^2} = \frac{\bar{a}}{\bar{a}^2 - \bar{b}^2}\frac{2\lambda_{33}}{\pi}\left(1 - \tanh\left(\frac{m_0 a}{\bar{a}}\right)^2 + \frac{\tanh\left(\frac{m_0 a}{\bar{a}}\right)}{\frac{m_0 a}{\bar{a}}}\right). \tag{2.103}$$

For a finite radius value, as $m_0 a$ tends to zero, the left hand term tends to 1 (This fact was previously explained and can be readily seen from Figures (2-7 to 2-10) while the right hand term in the brackets tends to 2. The relation simply becomes:

$$\frac{\lambda_{33}}{\bar{a}} = \frac{\pi}{4}. \tag{2.104}$$

This is exactly the value observed in figures 2-3 to 2-6.

2.4 Appendices

Appendix 2.A

Evaluation of Different Expressions from Chapter 2

These are the expressions presented in Chapter 2 and not fully evaluated for brevity.

From (2.36),

$$\begin{aligned} \alpha_n{}^* &= \frac{\epsilon_n}{d}\int_0^d \frac{\hat{u}}{2d}(z^2 - \frac{a^2}{2} + b^2 \ln a)\cos(\lambda_n z)\, dz \\ &= \begin{cases} \left(\frac{1}{6} - \frac{a^2}{4d^2} + \frac{b^2}{2d^2}\ln a\right)\hat{u} & (n = 0), \\ \alpha_n{}^* = \frac{2d(-1)^n}{(n\pi)^2}\ \hat{u} & (n > 0). \end{cases} \end{aligned} \tag{2.A.1}$$

From (2.50),

$$\begin{aligned} A_k^* &= \frac{1}{R_k'(a)}\int_0^d \frac{\hat{u}}{2d}(\frac{b^2}{a} - a)Z_k(z)dz \\ &= \begin{cases} \frac{1}{R_0'(a)}\frac{\hat{u}}{2d}\left(\frac{b^2}{a} - a\right)\frac{\sinh(m_0 d)}{m_0\sqrt{N_0}} & (k = 0), \\ \frac{1}{R_k'(a)}\frac{\hat{u}}{2d}\left(\frac{b^2}{a} - a\right)\frac{\sin(m_k d)}{m_k\sqrt{N_k}} & (k > 0). \end{cases} \end{aligned} \tag{2.A.2}$$

From (2.52),

$$C_{nk} = \int_0^d \cos(\lambda_n z)\, Z_k(z) dz$$

$$= \begin{cases} \dfrac{(-1)^n \sinh(m_0 d)}{\left(1 + \left(\dfrac{n\pi}{m_0 d}\right)^2\right) m_0 \sqrt{N_0}} & (k = 0), \\ \dfrac{(-1)^n \sin(m_k d)}{\left(1 - \left(\dfrac{n\pi}{m_k d}\right)^2\right) m_k \sqrt{N_k}} & (k > 0). \end{cases} \tag{2.A.3}$$

From (2.59), for $n = 0$,

$$\psi_0^* = \int_b^a r dr = \frac{a^2}{2} - \frac{b^2}{2}, \tag{2.A.4a}$$

and for $n > 0$

$$\psi_n^* = \frac{1}{\psi_n(a)} \int_b^a r \left(I_0(\lambda_n r) - \frac{I'_0(\lambda_n b)}{K'_0(\lambda_n b)} K_0(\lambda_n r) \right) dr$$
$$= \frac{a}{\lambda_n} \frac{I_1(\lambda_n a) K_1(\lambda_n b) - I_1(\lambda_n b) K_1(\lambda_n a)}{I_0(\lambda_n a) K_1(\lambda_n b) + I_1(\lambda_n b) K_0(\lambda_n a)}. \tag{2.A.4b}$$

From (2.84),

$$A_{kj}^* = -\epsilon_k i^{k+1} J'_k(m_0 a) \frac{R_{kj}(a)}{R'_{kj}(a)} \frac{\sqrt{N_0}}{m_0 \sinh(m_0)} \delta_{0j}\,, \tag{2.A.5}$$

where δ_{0j} is the Kronecker delta function. Equation (2.98) therefore reduces to:

$$g_{0n} = -2\pi A_{00}^* C_{n0} + \alpha_{0n}^*\,. \tag{2.A.4}$$

Finally from (2.87),

$$\alpha_{pn}^*$$
$$= \frac{-1}{\zeta_0} \int_0^d \int_0^{2\pi} \zeta_0 \sum_{k=0}^{\infty} \epsilon_k i^{k+1} J_k(m_0 a) \cos(k\theta) \frac{Z_0(z)}{Z'_0(1)} \cos(\lambda_n z) \cos(p\theta)\, d\theta dz \tag{2.A.5}$$
$$= -2\pi i^{p+1} J_p(p_0 a) \frac{\sqrt{N_0}}{p_0 \sinh(p_0)} C_{n0}\,.$$

Chapter 3 Power Output from Regular and Irregular Waves

The diffraction and radiation problems are just special cases of the general behavior of a body in water. The former makes no account of any radiated waves while the latter makes no account of any incident waves. A real situation will most probably include both, and a wave energy converter will inevitably absorb and radiate waves. All the analysis performed up to this point is just a preparation to be able to compute the power extracted by the heaving cylinder. At the end, it is only the power produced that is the useful outcome and is what we really care about. This chapter starts by computing the power output of our buoy at a fixed frequency of the incident wave. This is the analysis of the dynamics in regular waves. The chapter ends by extending the analysis to the more general irregular waves.

3.1 Power Output from a Single Wave

The analysis of the power absorption characteristics of a wave energy converter in regular waves is not very representative of real sea conditions. However, experiments in the lab are usually performed using a fixed frequency source. Furthermore, the study of the dynamics in regular waves is the first step for the study in irregular waves. These facts make the former a necessary step of the analysis. This section answers the question of how much power conversion can be achieved using the proposed system and assumptions. We start with a summation of forces on the buoy which can be written as:

$$(M_{33} + M)\ddot{U} + (B_{33} + c)\dot{U} + SU = F^D \,, \tag{3.1}$$

where B_{33} and M_{33} are the radiation damping coefficient and added mass introduced in Chapter 2. M is the mass of the buoy, c is the damping of the power takeoff mechanism (PTO) and SU is the buoyancy force and is equal to $\rho g A U$ where A is the cross sectional

of the buoy in the vertical direction. Finally, F^D is the vertical excitation force caused by the incoming wave on the buoy.

The excitation force varies sinusoidally in regular waves and is given by $F^D = Re(\hat{F}^D e^{-i\omega t})$ (and the displacement is also sinusoidal given by $U = Re(\hat{U} e^{-i\omega t})$ because the system is linear), then the equation reduces to:

$$[(S - \omega^2(M_{33} + M)) - i\omega(B_{33} + c)]\hat{U} = \hat{F}^D \,. \tag{3.2}$$

The power is the product of the force and velocity. We have to differentiate here between the delivered power P_e, the radiated power P_r, and the useful power P which is the power extracted by the PTO and is given by:

$$P = P_e - P_r = \frac{1}{2} Re\left(\hat{F}^D \hat{u}^*\right) - \frac{1}{2} B_{33} \hat{u}\hat{u}^* \,, \tag{3.3}$$

where $\hat{u} = -i\omega\hat{U}$ is the complex amplitude of the velocity and * indicates complex conjugate. All these powers are time averaged. This further reduces to ([19])

$$P = \frac{1}{2} c|\hat{u}|^2 = \frac{1}{2} \frac{c\left|\hat{F}^D\right|^2}{(c + B_{33})^2 + \left(\omega M + \omega M_{33} - \frac{S}{\omega}\right)^2} \,. \tag{3.4}$$

This equation allows the calculation of the power from knowledge of the diffraction force, the hydrodynamic coefficients and the specifications of the buoy. Introducing these parameters in dimensionless form:

$$\frac{B_{33}, c}{\omega\rho\pi a^3} = \lambda_{33}, \lambda_c, \tag{3.5}$$

$$\frac{M_{33}, M}{\rho\pi a^3} = \mu_{33}, \mu, \tag{3.6}$$

$$\frac{S}{\omega^2\rho\pi a^3} = \eta_0^A \,, \tag{3.7}$$

$$\frac{\left|\hat{F}^D\right|}{\pi a^2 \zeta_0 \rho g} = \sigma \,. \tag{3.8}$$

Here, λ_{33} and μ_{33} are the hydrodynamic parameters that were the outcome of the analysis of the radiation problem presented in section 2.2 while σ is the dimensionless amplitude

of the diffraction force from section 2.3. The rest of the parameters here are defined in this manner for convenience. The power is now given by:

$$P = \frac{\pi \zeta_0^2 \rho g^2 a}{2\omega} \frac{\lambda_c \sigma^2}{(\lambda_c + \lambda_{33})^2 + (\mu + \mu_{33} - \eta_0^A)^2}. \tag{3.9}$$

This equation is used to calculate the power output from our device. If we use the shallow water velocity $V_s = \sqrt{gh}$ then the power is given in dimensionless form as:

$$\frac{P}{\frac{\pi}{2}\zeta_0^2 \rho V_s^3} = \frac{\bar{a}}{\sqrt{\nu}} \frac{\lambda_c \sigma^2}{(\lambda_c + \lambda_{33})^2 + (\mu + \mu_{33} - \eta_0^A)^2}. \tag{3.10}$$

The dimensionless power is written in this form to ensure that only the power varies on the right side of the equation as the radius or the frequency varies on the left side.

One of the most important outcomes of our analysis is the power density which is defined to be the power output we are getting per unit mass of device. Since capital cost is directly associated with mass, this indicator shows how much power we are getting per unit currency spent initially as an investment. The power density can be written as:

$$\frac{P/M}{\zeta_0^2 V_s^3/(2h^3)} = \frac{1}{\mu \bar{a}^2 \sqrt{\nu}} \frac{\lambda_c \sigma^2}{(\lambda_c + \lambda_{33})^2 + (\mu + \mu_{33} - \eta_0^A)^2}. \tag{3.11}$$

The maximum displacement of the buoy is an important indicator of how valid our linear assumption is. For the model to be valid, the displacement should be small compared to the other length parameters (wave amplitude, ocean depth …) in the problem. We consider that a displacement of the order of magnitude of the wave amplitude is acceptable. That is why we use this amplitude to write the maximum displacement in dimensionless form:

$$\frac{|\widehat{U}|}{\zeta_0} = \frac{1}{\bar{a}\nu} \frac{\sigma}{\sqrt{(\lambda_c + \lambda_{33})^2 + (\mu + \mu_{33} - \eta_0^A)^2}}. \tag{3.12}$$

The only remaining parameter is λ_c, the damping of the PTO. The damping of the PTO is chosen so as to yield the highest power value and is given by:

$$\lambda_c = \sqrt{\lambda_{33}^2 + (\mu + \mu_{33} - \eta_0^A)^2}. \tag{3.13}$$

The specific frequency that causes resonance may be misinterpreted to be when $\mu + \mu_{33} - \eta_0^A = 0$ and (3.10) gives the result well known in electric circuits that the power absorbed is maximized when the damping of the device (the load) is equivalent to the radiation damping (the source resistance). The power in this case is simply given by:

$$\frac{P}{\frac{\pi}{2}\zeta_0^2 \rho V_s^3} = \frac{\bar{a}}{\sqrt{v}} \frac{\sigma^2}{4\lambda_c}. \tag{3.14}$$

However, because the power has the extra frequency term $(1/\sqrt{v})$ in (3.10), we do not expect to get the maximum power at that point. The results show that the peak power is achieved at lower frequencies. Before moving to the results, however, here is some insightful information describing our device.

3.1.1 Complementary Information

The energy flux per unit crest width of the incoming wave is defined to be [19]:

$$J = \frac{1}{4} \frac{\rho g^2 \zeta_0^2}{\omega} D\,, \tag{3.15}$$

where D is the depth function introduced in equation (2.99). Furthermore, by substituting the definitions (3.5) and (3.8) in equation (2.98), the Haskind relation can be written as:

$$\sigma^2 = \frac{2D\lambda_{33}}{\pi m_0 a}. \tag{3.16}$$

Using the last two equations and (3.10) then,

$$m_0 W = m_0 \frac{P}{J} = \frac{4\lambda_{33}\lambda_c}{(\lambda_{33} + \lambda_c)^2 + (\mu + \mu_{33} - \eta_0^A)^2}, \tag{3.17}$$

where W is the capture width (also called the absorption width) of the buoy [9]. It measures the width of an incoming wave whose energy is equal to that absorbed by the buoy. The maximum value that (3.17) can attain is exactly unity, which occurs when the expression $\mu + \mu_{33} - \eta_0^A = 0$ is satisfied and when the PTO damping is equivalent to the

radiation damping. For our cylindrical buoy, the mass is equal to the mass of the displaced water:

$$M = \rho\pi(h-d)(a^2-b^2)\,, \tag{3.18}$$

Therefore,

$$\mu = \left(\frac{1}{\bar{a}} - \frac{\bar{d}}{\bar{a}}\right)\left(1 - \frac{\bar{b}^2}{\bar{a}^2}\right). \tag{3.19}$$

The buoyancy force can be expressed as:

$$S = \rho g\pi(a^2-b^2), \tag{3.20}$$

Therefore from (3.7),

$$\eta_0^A = \frac{1}{v\bar{a}}\left(1 - \frac{\bar{b}^2}{\bar{a}^2}\right). \tag{3.21}$$

The added mass and damping are the results of our previous analysis and the PTO damping is given by (3.13). Now we are ready to compute the power.

3.1.2 Results and Discussion

The previous equations (3.10-12) were used to calculate the power, power density and displacement of the buoy. The results are presented in dimensionless form as defined by those equations for selected values of frequencies and radii. Each of the figures represents the results for one draft to buoy radius ratio and includes the results for three different frequencies varied over a range of radii values (Figures 3-1 to 3-3) or three different radii varied over a range of frequency values(Figures 3-4 to 3-6).

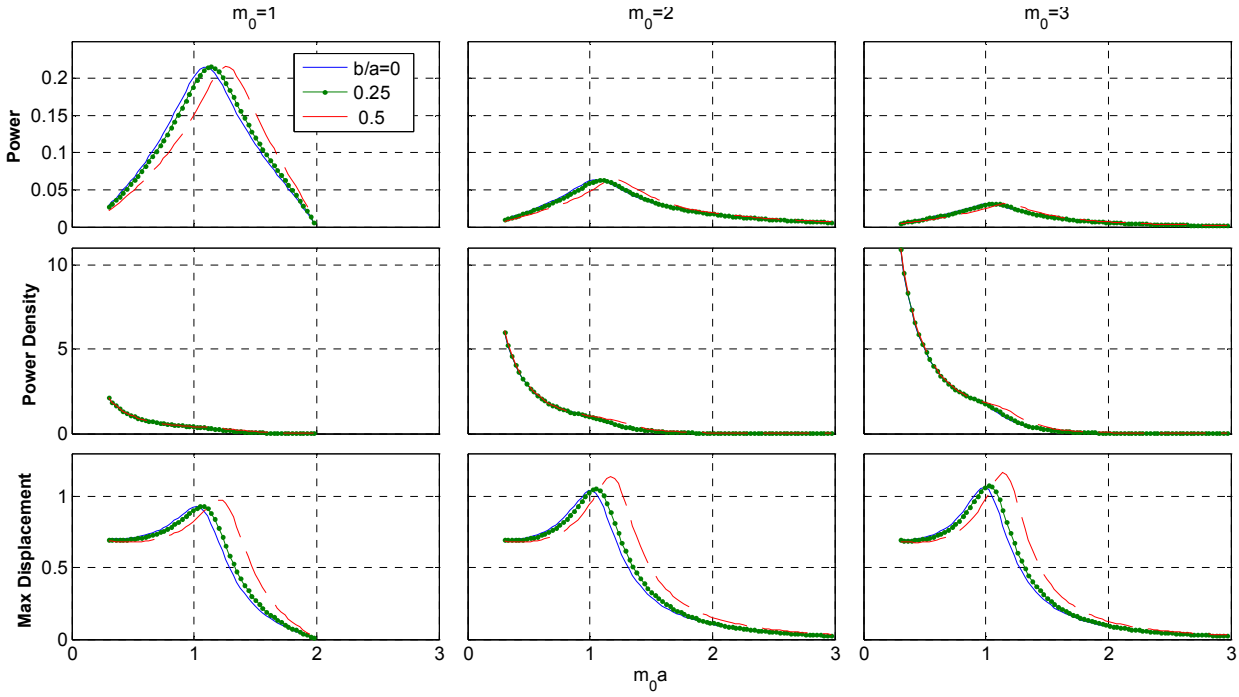

Figure 3-1: Plots of the power output (row 1), the power density (row 2), and the maximum displacement (row 3) as a function of the buoy radius (represented by $m_0 a$) for three different values of b/a and dimensionless wavenumbers m_0 at $H/a = 0.5$

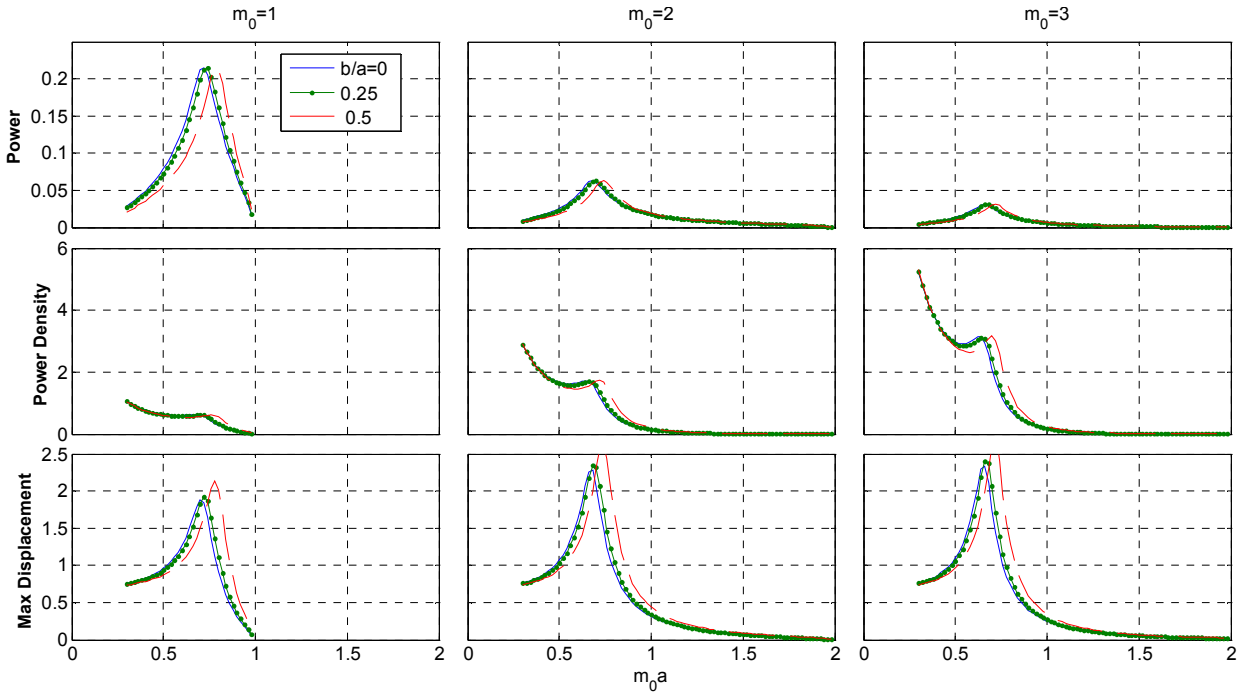

Figure 3-2: Plots of the power output (row 1), the power density (row 2), and the maximum displacement (row 3) as a function of the buoy radius (represented by $m_0 a$) for three different values of b/a and dimensionless wavenumbers m_0 at $H/a = 1$

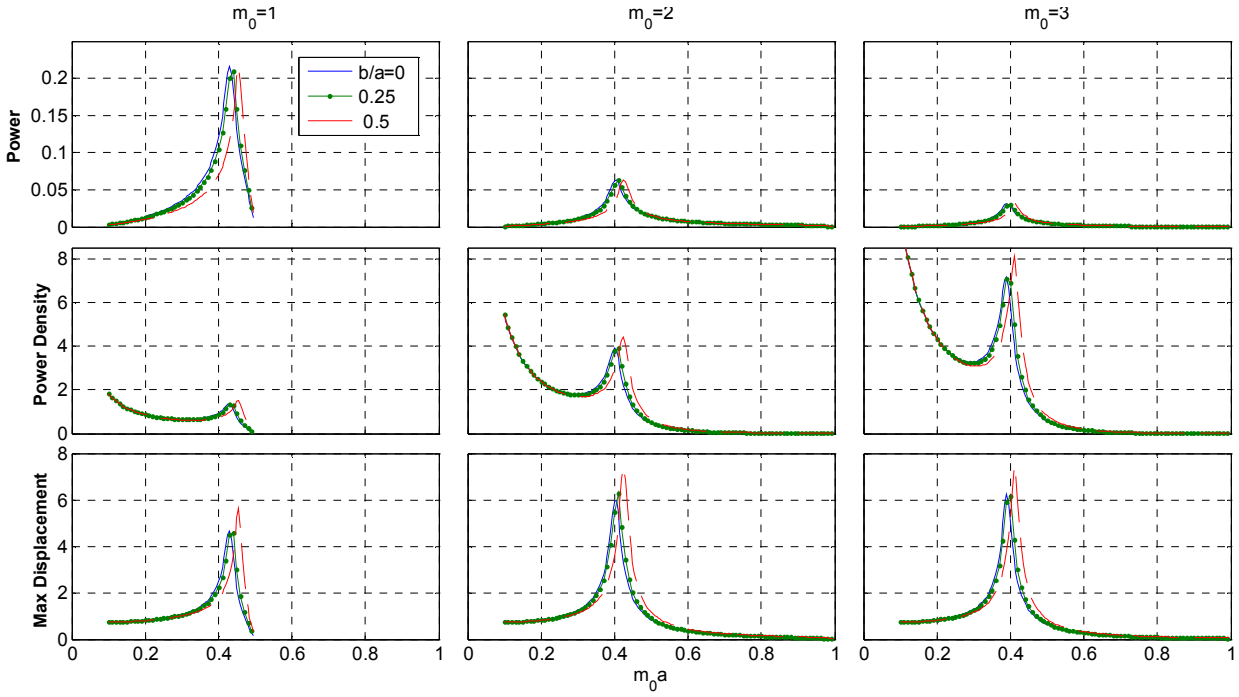

Figure 3-3: Plots of the power output (row 1), the power density (row 2), and the maximum displacement (row 3) as a function of the buoy radius (represented by $m_0 a$) for three different values of b/a and dimensionless wavenumbers m_0 at $H/a = 2$

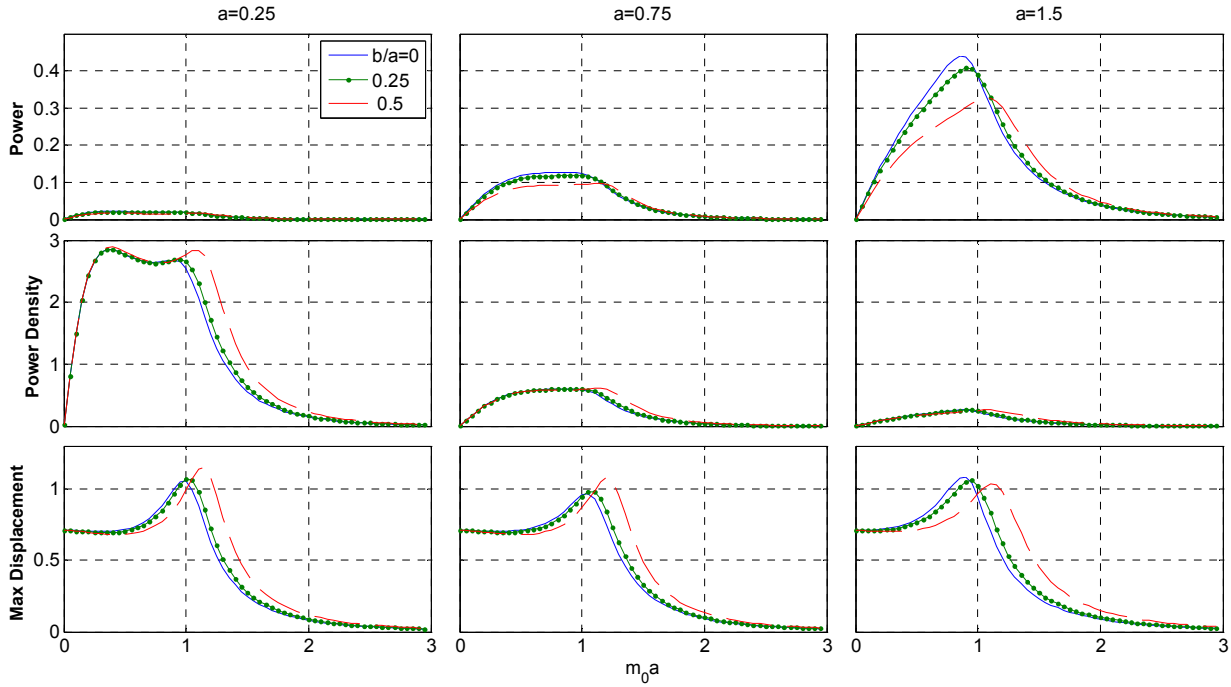

Figure 3-4: Plots of the power output (row 1), the power density (row 2), and the maximum displacement (row 3) as a function of the frequency (represented by $m_0 a$) for three different values of b/a and a/h at $H/a = 0.5$

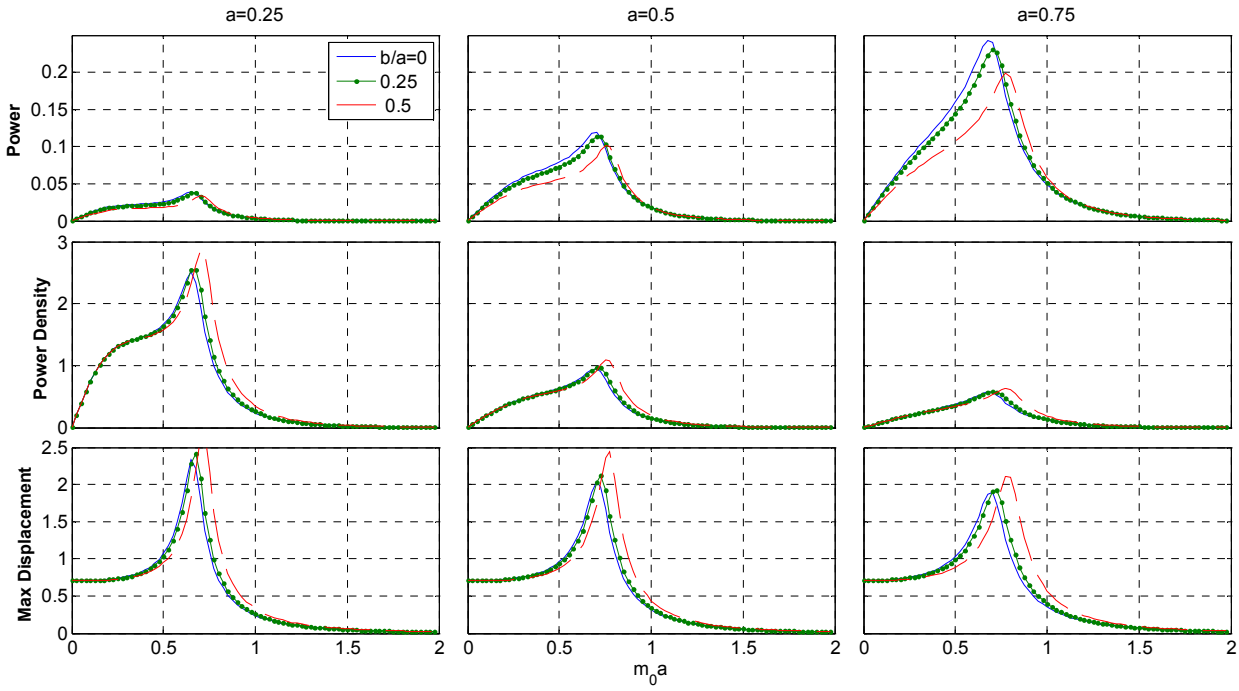

Figure 3-5: Plots of the power output (row 1), the power density (row 2), and the maximum displacement (row 3) as a function of the frequency (represented by $m_0 a$) for three different values of b/a and a/h at $H/a = 1$

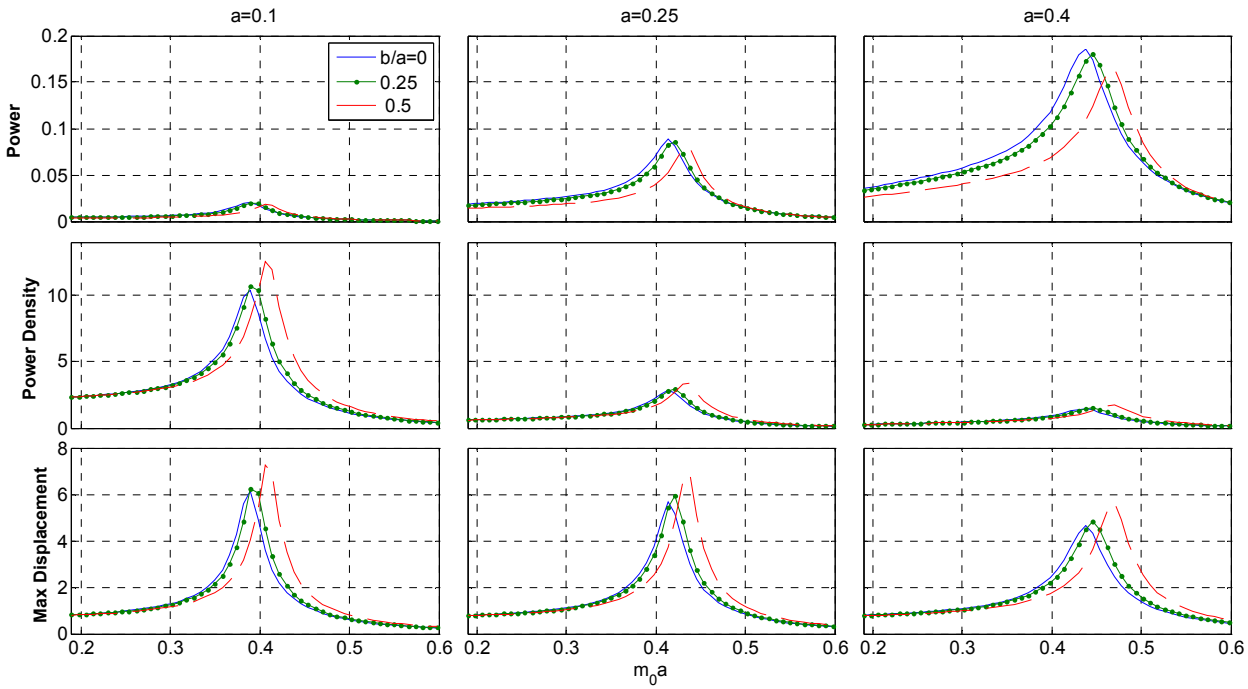

Figure 3-6: Plots of the power output (row 1), the power density (row 2), and the maximum displacement (row 3) as a function of the frequency (represented by $m_0 a$) for three different values of b/a and a/h at $H/a = 2$

Referring to figures 3-1 to 3-3, by varying the radius, we can tell that there is an optimum radius for each frequency that achieves the highest power (where resonance occurs). As the frequency increases, the value of this radius doesn't seem to change much although the corresponding power values were found to drop significantly (possibly because of the drop in the energy flux). A local maximum for the power density is found to occur at this same radius. This is especially true for slender buoys. Surprisingly, the effect of the spar is simply to shift the power peaks, with no change in their values, to higher radii. Another effect to be noted is the slight increase in power density for larger buoys. The reason for that is the otherwise dead volume of the buoy that is replaced by the spar. This fact makes it possible to design for the same power rating, with the spar present, by simply changing the geometry. The penalty, as always, is the slightly higher displacement amplitudes. It is worth mentioning that the flatter the buoy is, the wider it has to be to resonate.

The radii of figures 3-4 to 3-6 were chosen so as to ensure that the buoy draft is less than the ocean depth. Here, the effect of the spar is to decrease the power and power density for the lower and mid-range frequencies and increase them for the higher range (a fact that we could not see from figures 3-1 to 3-3). The displacement seems to follow the behavior of the power density which is to be expected. It is interesting to note the presence of two maxima for the power and power density for small buoys. The increasing slenderness of the buoy causes an increase in the peak power accompanied by a narrowing of the power and power density curves and therefore limiting the power absorption capabilities of the device.

There remains one unanswered question: What are the optimum size parameters that result in the maximum power output and power density characteristics of the system? In order to obtain these values, a simple direct search algorithm to locate the optimum values seems the reasonable answer when a closed form semi-analytical solution is available. With the resolution used, the results were more like a noisy signal superimposed on a smooth curve. Higher resolutions were not possible because of the computational time required. The search was restricted to the ranges: $= [0.1,2]$, $\mathrm{b}/\mathrm{a} = [0,0.5]$, and $\mathrm{d} = [0.1,0.9]$.

For the problem of getting the optimum parameters that maximize the power, localized simulations for narrow frequency bandwidths showed that the noisy nature is inherent in the problem itself and is not the result of lower resolutions. In fact, a sensitivity analysis for the parameters showed that very small changes in the power resulted when relatively larger changes were made to the parameters. For that reason, it was safe to curve-fit the results instead. The power values of the fits were then found to be equal to the theoretical maximums. This fact confirms that they are optimum. The fits have the additional property of providing stable power values for the reason mentioned earlier.

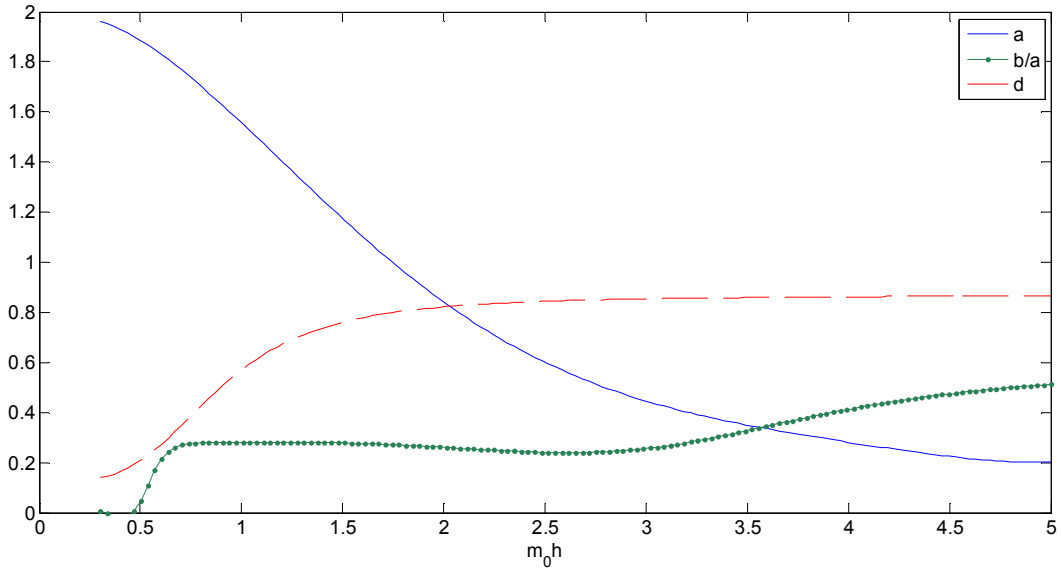

Figure 3-7: The buoy radius a/h, pole radius b/a and floatation d/h parameters optimized for maximum power at a given wavenumber of the incident wave

The problem of getting the optimum parameters that maximize the power density was more difficult. The reason is that in general, high power densities are accompanied by very high displacements. To stay within limits of linear theory and practicality, search was limited to values that resulted in displacements lower than 2.

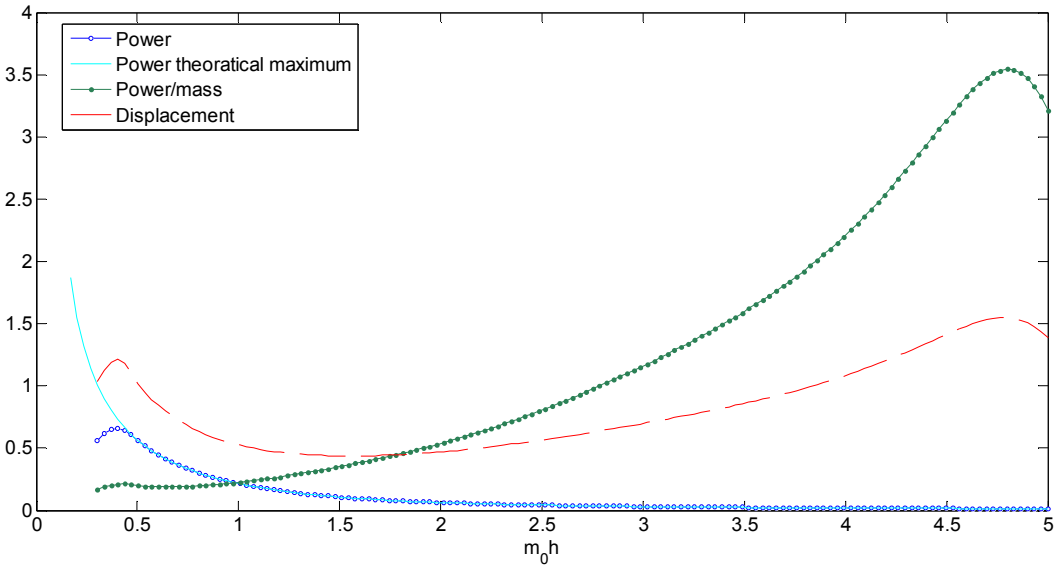

Figure 3-8: The maximum power output possible using the optimal parameters of $a, b/a$ and d and its corresponding power density and displacement plots

The results for the maximum power in Figure 3-7 show a gradual decrease of the optimum buoy radius and draft with increasing wavenumber. That is, the optimum size of the buoy is decreasing. To understand why that is happening, we have to go back to the idea of resonance. There is a specific shape and size of the buoy that has inherent oscillatory properties that render it in phase with the incoming wave. As the frequency increases (and therefore the wavelength decreases) similarity tells us that the size of the buoy should decrease as well to form a minimized image of the lower frequency situation. The question here is then, since the frequency is increasing in a linear manner, why isn't the geometry decreasing linearly as well? That's because other factors have influential effects as well. The body is now smaller as compared to the ocean depth which changes the image of the diffraction field for the incoming wave. Furthermore, although the wavenumber increases linearly, the power available for extraction changes in a nonlinear manner. The curve fits for the power problem are in terms of $x = m_0 h$ as an independent variable and were found to be:

$$a = 0.005464x^5 - 0.0843x^4 + 0.4731x^3 - 1.063x^2 + 0.2569x + 1.969\,, \tag{3.22}$$

$$\frac{b}{a} = \frac{0.6196x^5 - 4.169x^4 + 9.336x^3 - 6.449x^2 + 1.657x - 0.1325}{x^5 - 6.181x^4 + 10.78x^3 + 4.402x^2 - 10.13x + 3.194}, \tag{3.23}$$

$$d = \frac{14320x^3 - 4545x^2 + 361.6x + 1234}{x^4 + 16350x^3 - 4058x^2 - 2546x + 10200}. \tag{3.24}$$

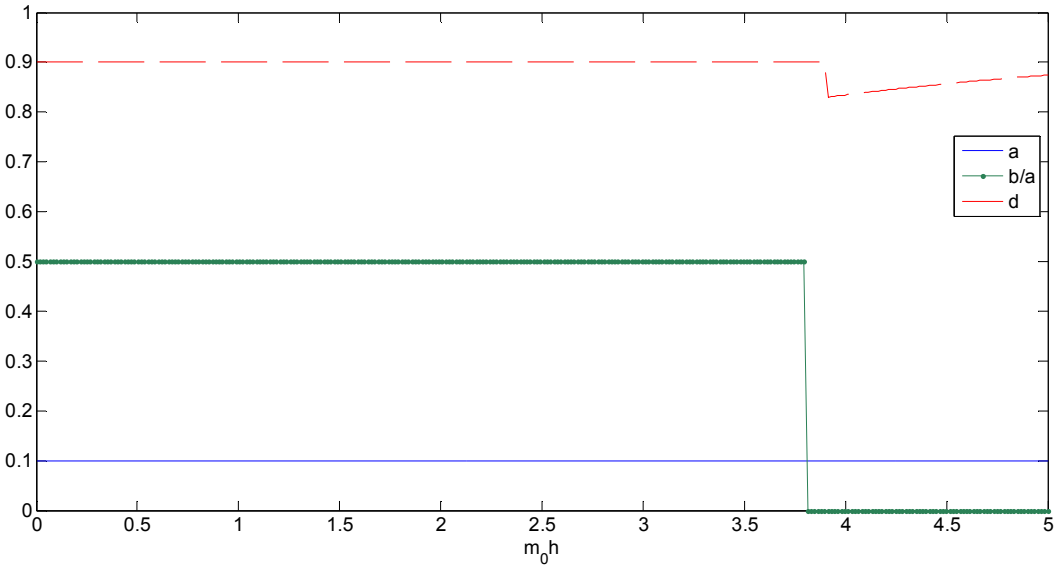

Figure 3-9: The buoy radius a/h, pole radius b/a and floatation d/h parameters optimized for maximum power density at a given wavenumber of the incident wave

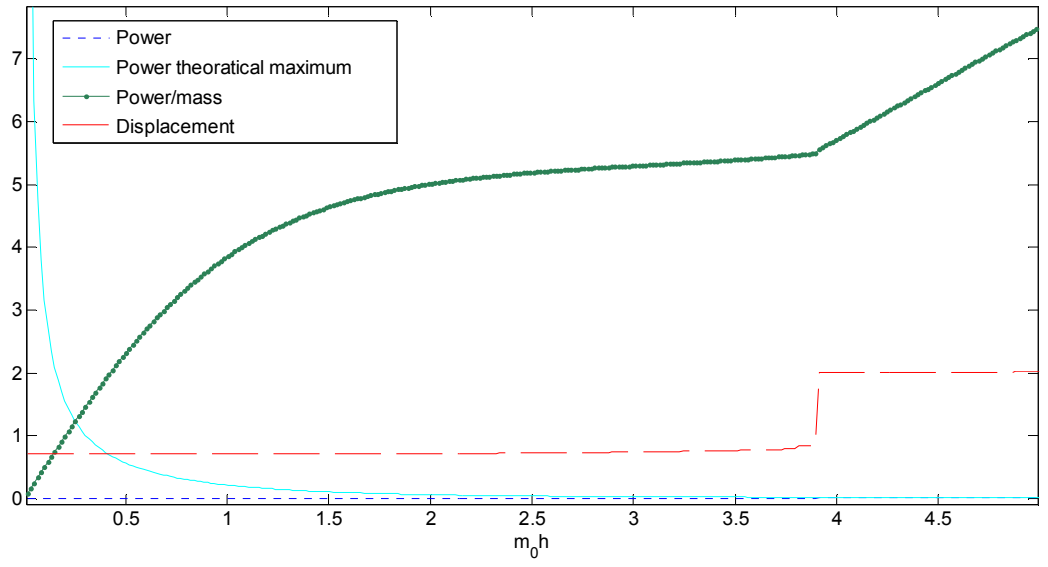

Figure 3-10: The maximum power density possible using the optimal parameters of a, b/a and d and its corresponding power density and displacement plots

The parameters optimized for maximum power per unit mass are rather constant for most of the range of frequencies considered. These are the values that lead to the lowest mass of the buoy. At the higher frequencies ($m_0 h \cong 3.8$), a discontinuity in the value of the optimum pole radius is very clear. This is not to be considered erroneous though, as optimum values may experience such discontinuities. The reason for that is that power per unit mass is a surface function of geometry and it might have values higher than others in certain places which refrain to be so at other places. This fact is confirmed when we look at the power per unit mass curve which looks more like two smooth curves attached at the discontinuity area (notice the discontinuity in the buoy bottom depth value as well). If any of these two curves is extended, then lower values result. A note to point in this case is the low power values achieved.

3.2 Power Output from a Wave Spectrum

We further proceed to study the behavior of our device in real sea conditions. Up till now, only monochromatic waves were considered but in the ocean (and within the limits of linear theory), the wave is at any time a superposition of many different frequencies. These are called random waves. What is the effect of the pole on the output in irregular waves? The answer to this important question is vital for designing this system or even considering it in the first place.

The power in this case is given by:

$$P_t = \int_0^\infty 2P(\omega)E(\omega)d\omega\,, \tag{3.25}$$

where $E(\omega)$ is the so called energy spectrum. It represents the energy content of each frequency. The power term in this equation is for a unit amplitude incident wave. For simplicity, we choose a Pierson-Moskowitz spectrum which is an empirical relation usually used to represent fully developed waves in deep water [19]. It can be expressed as:

$$E(\omega) = \frac{5}{16}\frac{H_s^2}{\omega}\left(\frac{\omega_p}{\omega}\right)^4 exp\left\{-\frac{5}{4}\left(\frac{\omega_p}{\omega}\right)^4\right\}. \tag{3.26}$$

Here H_s is the significant wave height defined to be the average of the highest 1/3 of the wave heights while ω_p is the frequency at the peak value of the spectrum. The energy frequency for random waves is defined as $\omega_e = 2\pi/T_e$ such that:

$$T_e = \frac{\int \frac{2\pi}{\omega} E(\omega) d\omega}{\int E(\omega) d\omega} \tag{3.27}$$

is the energy period [36]. The procedure in this case is to tune the buoy radius (in the absence of the spar) to the energy frequency, optimize the PTO damping at that radius for the different geometries, fixing these values for different frequencies and then performing the integration over the whole spectral range using (3.25). This forms a basis of comparison to assess the effect of the spar.

We want to capture the real situation as much as possible. That is, to get a sense of the ranges of power we are talking about. That is why dimensional values will be considered. Furthermore, to be sure the results are valid, it is important to ensure that the buoy will neither leave the water surface nor hit the ocean bottom. Otherwise, the problem becomes highly nonlinear and the analysis done will be invalid. We assume that the buoy will not leave the water surface if the following condition is met:

$$H - U_{max} > \zeta_{max}\,, \tag{3.28}$$

where H is the buoy draft, U_{max} is the maximum buoy displacement and ζ_{max} is the highest incident wave amplitude. This guarantees the validity of the analysis even when the buoy is at maximum amplitude upward and the incoming wave of highest amplitude is at a trough. Here we assume that the highest wave height (twice the amplitude) is twice the significant wave height [37]. Furthermore, since the water depth is finite, we need to make sure that the buoy does not hit the sea floor by ensuring the following condition is satisfied:

$$H + U_{max} < h\,. \tag{3.29}$$

Here h is the water depth. The buoy maximum displacement can be approximated using

$$U_{max} = \sqrt{\int_0^\infty 2|\widehat{U}(\omega)|^2 \, E(\omega) d\omega} \,, \tag{3.30}$$

where $|\widehat{U}(\omega)|$ is buoy displacement amplitude due to unit-amplitude incident wave. The 2 factor follows from the definition of $E(\omega)$.

The results are presented in Figures 3-11 to 3-13. The conditions (3.28-29) are already accounted for in the figures. This work has been already been published in the World Renewable Energy Congress (WREC XI) in Abu Dhabi [38].

3.2.1 Results and Discussion

Computations are carried out for a significant wave height of 4 meters (typical of the North Atlantic region rich in the wave resource). For the Pierson–Moskowitz spectrum, this corresponds to a peak frequency of $\omega_p = 0.63(rad/sec)$, making use of the following relation [39]:

$$\omega_p = 0.4\sqrt{g/H_s} \,. \tag{3.31}$$

From (3.26-27), the energy frequency is $\omega_e = 0.73\ (rad/sec)$ for our case. Two water depths of 20 and 50 meters are considered. The energy flux is the power carried per meter of the incident wave front. It is given by:

$$J = \rho g \int_0^\infty E(\omega) c_g(\omega, h) d\omega \,, \tag{3.32}$$

where $c_g(\omega, h)$ is the group velocity in water of finite depth h. The corresponding energy fluxes are 77(kW/m) and 72(kW/m) for the chosen depths respectively when the sea water density ρ is taken to be $1025\ (kg/m^3)$.

The integral (3.25) is evaluated using the trapezoidal rule. Since this is an approximation, it is important to make sure to choose a large enough frequency interval so that the integrand almost vanishes on both sides.

In Figure 3-11, the power (top graphs) and power density (bottom graphs) curves are presented as a function of the draft to buoy radius ration H/a and for three different pole radius to buoy radius values b/a. The same results were plotted in Figure 3-13 with b/a on the x-axis and for different H/a values. The procedure to reach these power characteristics was described earlier in this section. The optimum radius for the case of spar absence ($b/a = 0$) and the optimum damping coefficients (characteristics of the power takeoff system) for the different geometries are presented in Figure 3-12. The optimal damping coefficient is plotted in the second row where an enlarged plot of the higher range of the figure ($H/a > 1.5$) is included. The maximum displacement from equation (3.30) is also shown in that figure.

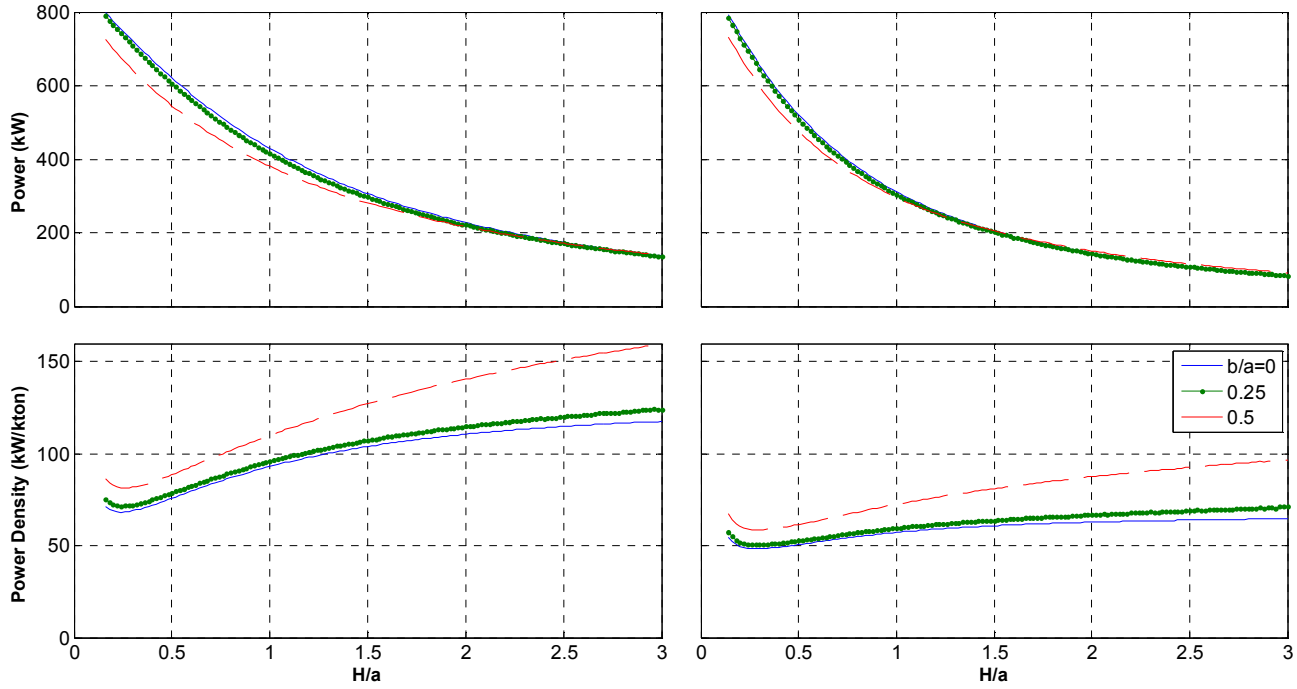

Figure 3-11: Power (row 1) and power density (row 2) plots for a floating buoy in real sea conditions as a function of H/a at two water depths of $h = 20\ m$ (left) and $h = 50\ m$ (right) for three different b/a values

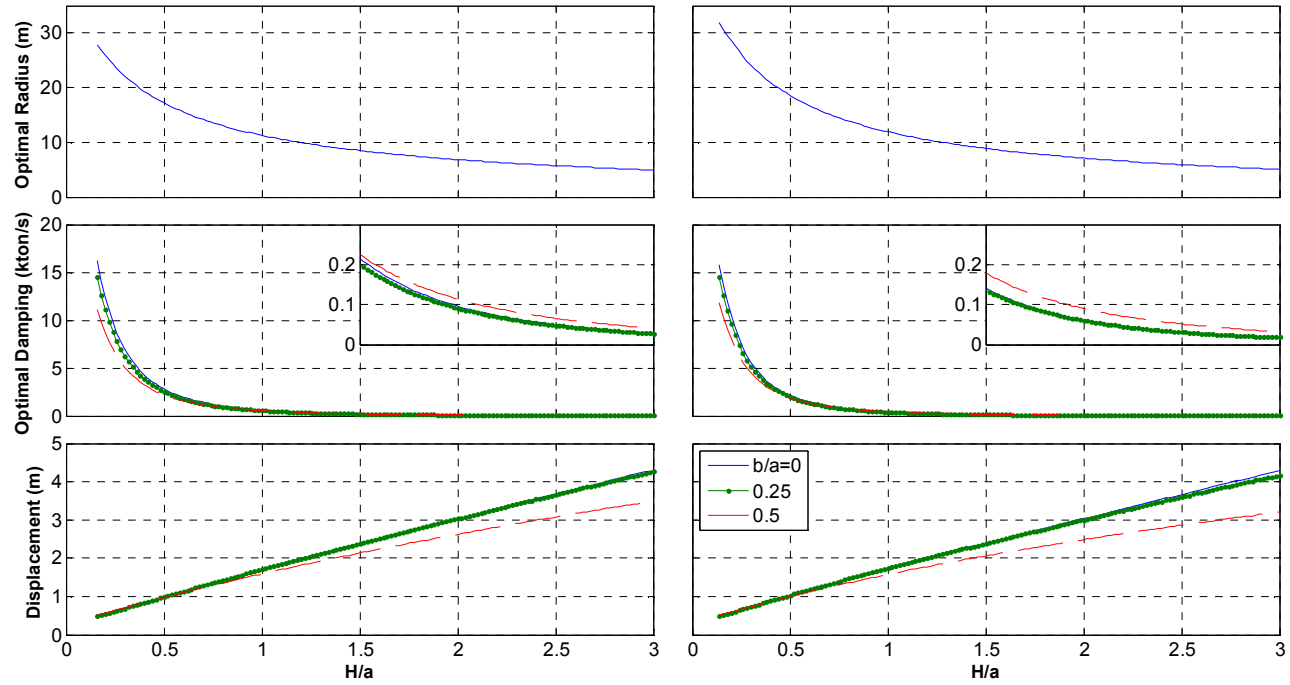

Figure 3-12: Optimum radius (row 1), PTO damping (row 2) and maximum displacement (row 3) plots for a floating buoy in real sea conditions as a function of H/a at two water depths of $h = 20\ m$ (left) and $h = 50\ m$ (right) for three different b/a values

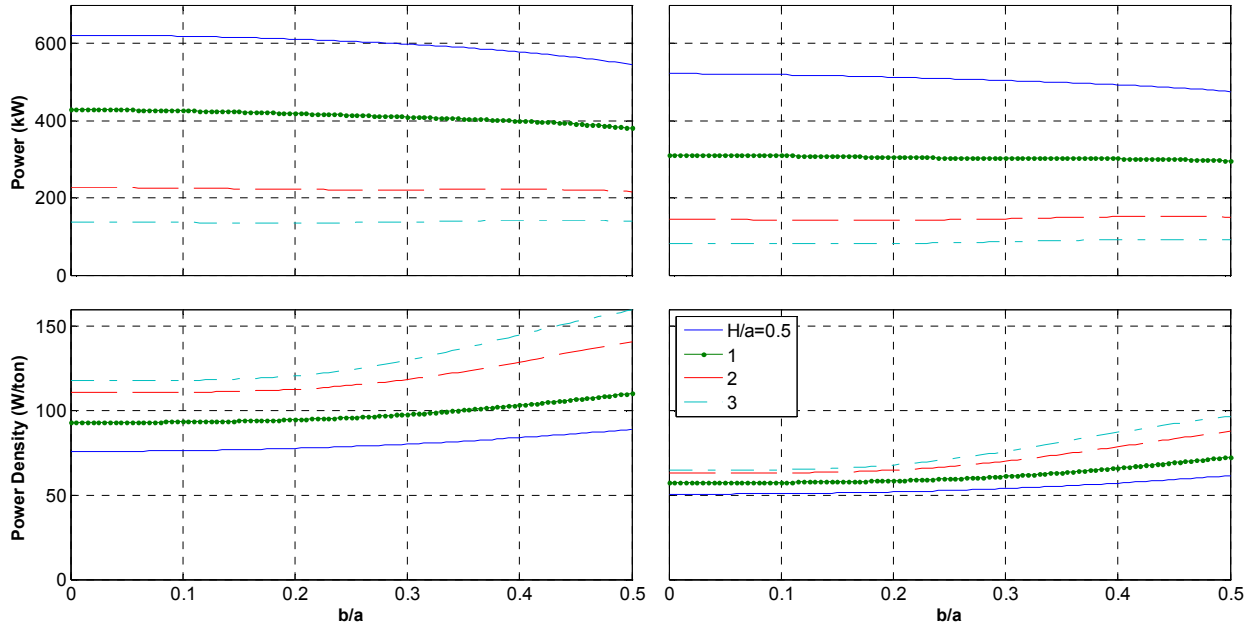

3-13: Power (row 1) and power density (row 2) plots for a floating buoy in real sea conditions as a function of b/a at two water depths of h=20 m (left) and h=50 m (right) for four different H/a values

As shown in Figures 3-11 and 3-13, the effect of the pole radius is to decrease the power for flat buoys (small H/a values) in general. The decrease in power diminishes, however, as the

buoy becomes more slender (large H/a). In fact, for very slender buoys, a power increase can be perceived. This is mostly pronounced in deeper water. This is quite an advantage when employing the pole. These figures also suggest that, with the proper choice of buoy geometry, the same amount of power can be achieved by employing the pole. The real advantage comes when we consider the power density. It is clear from Figure 3-13 that the power density increases only slightly as b/a increases from the lower end of the range. However, as b/a becomes bigger, the increase becomes dramatic and much higher power densities can be achieved by having the pole, a fact very evident in Figure 3-11. It is clear that the optimum radius and optimum damping values decrease fast and then slower as H/a increases.

Looking at the maximum displacements of the buoy from Figure 3-12, it is evident that the effect of the pole is to decrease the displacements. The decrease is even larger as the buoy becomes more slender. This may be partly due to the fact that the buoy is not exactly tuned to the energy period when the pole is present for reasons mentioned earlier.

3.3 Conclusion

This part of the thesis studied the power absorption characteristics of a truncated vertical cylinder supported by a concentric spar that is fixed to the ocean bottom. Potential flow, small amplitude oscillations of the buoy and the incident wave and a linear dashpot to model the PTO were assumed. The linear problem was treated in the frequency domain to solve for the hydrodynamic added mass and damping and the excitation force using the eigenfunction expansion method. The potentials of the region underneath the cylinder and outside were found by matching pressure and normal velocity at their interface. The power, power density and displacement amplitude were presented in dimensionless form for selected values of frequency and buoy radius. For a fixed frequency, the results show that the effect of the pole is to achieve the same power values as the case when the pole is absent but for wider buoys. An interesting result is that higher peak power density values can be achieved by employing the pole for certain geometries. The optimum geometrical parameters that achieve the highest power and power density values were also presented.

The work was then extended to random waves. A Pierson–Moskowitz spectrum, which describes irregular waves well enough, was assumed and use was made of the power from the previous results to compute the total power absorbed by the device from random waves. For each draft to buoy radius ratio, the radius of the buoy without the pole was tuned to the energy period to yield the highest power. The same radius is used for the case when the pole is present. The optimal PTO damping for each case is then fixed for the whole frequency range. A set of results for the power absorbed and the power density of the optimized buoy are then presented as a function of the buoy draft to buoy radius values and the pole radius to buoy radius values for two water depths. The optimum radii and damping coefficients and the maximum displacements were also presented.

Numerical results show how adding a pole to support the buoy affects the power absorption characteristics of the system in irregular waves. The effect of the added element is to decrease the power absorbed for flat buoys, something seen to diminish as the buoy becomes more regular in shape and eventually a slight increase in power is actually observed for slender buoys. This is more pronounced in deeper water. On the other hand, the effect of the pole on the power density is completely different. The power density was found to be higher when the pole is present, a fact that is subtle for small pole radii but becomes quite evident for large ones. The amplitudes of oscillation were also found to be lower when the pole is present, especially for slender buoys. The results presented thus far provide a valuable starting point for designing experiments to validate these results as well as to design similar wave energy converters.

Part 2 The Multi DOF Cylinder

Chapter 4 Hydrodynamics of the Pitch Mode

The second wave energy converter that will be discussed is again a floating buoy oscillating in water of constant depth. This time, the restriction on the buoy motion is relaxed as it is allowed to oscillate in a vertical plane. The orientation of that plane is unimportant since the body is axisymmetric about the z-axis. Studying the system when the incident wave is oriented along the x-direction will suffice. The buoy is moored using a tension cable.

This chapter mainly deals with the analysis of the hydrodynamic problem related to second configuration considered in this work. Since the pitch mode is the center of the discussions in this part of the thesis, the device here will be referred to as the pitching cylinder.

4.1 Problem Description

It is a well known fact (see Falnes [19]) that the theoretical maximum power that can be absorbed from an axisymmetric body oscillating in heave or pitch only is limited by the energy transport per unit frontage of the incident wave divided by the wave number. This maximum becomes three times higher when the modes: surge, heave and pitch are allowed. It might seem advantageous to employ all three modes simultaneously in a wave energy converter. This does not have to be the case as the power extracted is mostly less than the theoretical maximum unless some control strategy is considered [40]. In general, it is difficult to implement a controller [41] and in its absence, it is difficult to tell for a generic body whether allowing more degrees of freedom will help. So when is it advantageous to do that and when is it not?

It is the purpose of this work to show how much more power is actually extracted by employing the added modes to a vertical truncated circular cylindrical body in shallow water. The body considered is connected to the ocean bottom using a loose mooring cable which allows the body to oscillate about the ocean bottom (Figure 4-1). The coordinate system used is situated at the center of rotation at the bottom with the vertical z-axis pointing upwards and the positive x-axis is in the direction of wave propagation. Power is extracted from the heave and pitch

modes using two power takeoff mechanisms (PTOs). For simplicity and to keep our analysis within the frequency domain, the PTOs are modeled by linear translational and rotational dashpots for the heave and pitch modes placed along the cable and on the center of rotation respectively.

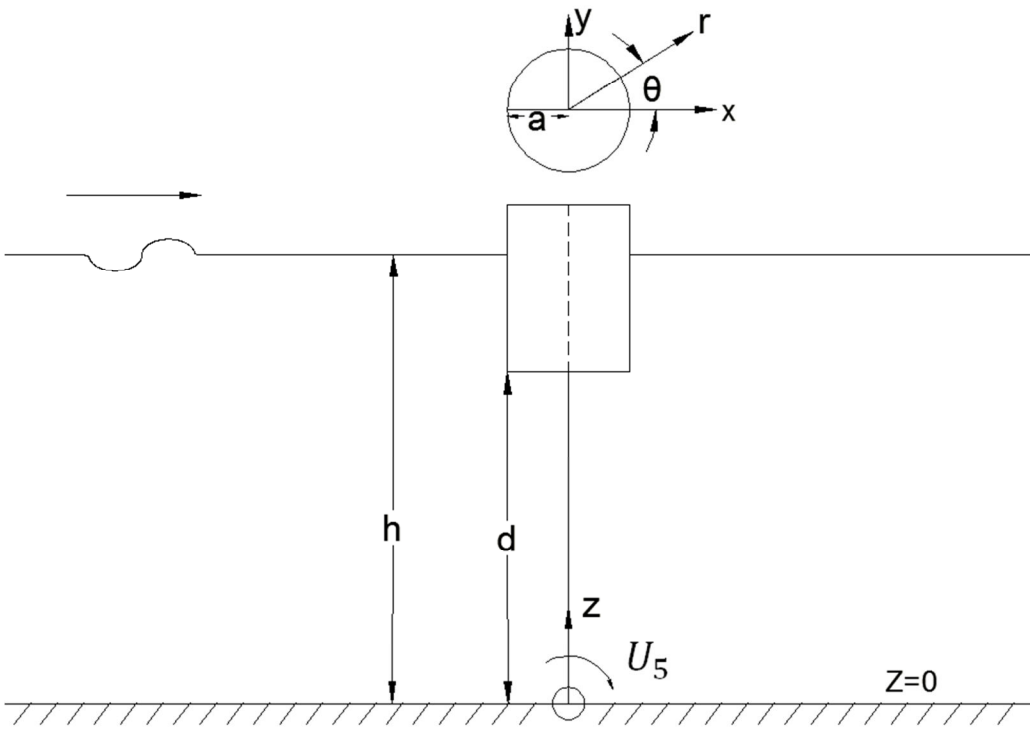

Figure 4-1: Schematic diagram of the Multi DOF System defining the different system parameters and the direction of wave propagation

We want to estimate the power that can be extracted by using such a device. To compute the power, the forces on the device and its reaction to the incoming waves must be known. The analysis for the hydrodynamics of the heave mode was presented in Chapter 2 and will not be repeated here. The surge mode was analyzed in [13]. Therefore, only the pitch problem will require a solution. Here the same assumptions used in part one are repeated. Namely, the fluid is considered to be incompressible and inviscid, irrotational and incompressible. Friction losses are also considered to be negligible. To make the problem linear, only small amplitude oscillations and incident waves are considered. The boundary conditions are therefore simple and to a first order approximation, only mean values of the buoy position and the free surface need to be considered. The linearized Bernoulli equation can thus be applied at the surface to lead to a simple free surface condition.

These assumptions enable us to model the flow as a potential flow, that is, the velocity field at any point can be conveniently represented by the gradient of a scalar potential function ϕ. It follows from the continuity equation that ϕ is governed by the Laplace equation. Cylindrical coordinates will be used because of the geometry of the problem.

The resulting potential will therefore include the combined effects of both radiation and diffraction. However, since the problem is linear, the total potential is just the summation of the individual potentials (the same notation of part one will be used):

$$\phi = \phi^I + \phi^s + \phi^r \,. \tag{4.1}$$

This fact makes the problem easier to handle as each potential can be solved for separately. We further assume that the velocity potential ϕ varies sinusoidally with time as $\phi = Re\{\hat{\phi}(r,z,\theta)e^{-i\omega t}\}$ and we non-dimensionalize length parameters and the potentials using depth and frequency as before.

For both the radiation and scattering problems, the potential amplitude function can be separated into two regions, the first for $r > a$ (the exterior region) and the other one below the cylinder for $r < a$ (the interior region). The two resulting potentials are denoted by $\hat{\phi}_e$ and $\hat{\phi}_i$ respectively. Separation of variables is used to solve for these two functions.

The incident wave is assumed to be unidirectional propagating in the positive x direction. The corresponding free surface displacement can again be represented by:

$$\zeta = \zeta_0 e^{im_0 x} = \zeta_0 \sum_{p=0}^{\infty} \epsilon_p i^p J_p(m_0 r) cos(p\theta) \,. \tag{4.2}$$

The boundary conditions needed include the linear free surface condition

$$\frac{\partial \hat{\phi}}{\partial z} - \frac{\omega^2 h}{g}\hat{\phi}\bigg|_{z=1} = 0 \,, \tag{4.3}$$

applied at the average surface position at $z = 1$ as the displacement is considered to be negligibly small. The no flux conditions at the bottom surface of the ocean apply:

$$\left.\frac{\partial \hat{\phi}}{\partial z}\right|_{z=0} = 0\,, \tag{4.4}$$

Slipping (nonzero velocities tangent to the body surfaces) is allowed since viscosity is considered negligible. In the normal direction, the velocity of the fluid must be the same as that of the buoy. This is zero for the diffraction problem. Finally, both problems must satisfy the radiation condition at infinity [5]:

$$\lim_{r\to\infty} \frac{1}{\sqrt{m_0 r}}\left(\frac{\partial \hat{\phi}}{\partial r} - i m_0 \hat{\phi}\right) = 0\,. \tag{4.5}$$

In what follows, we attempt to solve for the hydrodynamic coefficients (§4.2) and then for the excitation force (§4.3).

4.2 The Pitch Radiation Problem

The pitch radiation problem is very similar to the heave problem previously discussed. The only difference lies in the body boundary conditions. The condition at the buoy bottom just yields a new particular solution while the condition on the side will be part of the matching approximation at the interface of the internal and external regions.

4.2.1 Theory

Assume the velocity potential is of the form $\phi = Re\{u_p \hat{\phi}(r,z) e^{-i\omega t}\}\cos(\theta)$ where u_p is the pitch velocity amplitude. Besides the no flux condition at the bottom (4.4), $\hat{\phi}_i$ must satisfy:

$$\left.\frac{\partial \hat{\phi}_i}{\partial z}\right|_{z=d} = -r\,, \tag{4.6}$$

which means that the fluid velocity is equal to the buoy velocity at the buoy bottom and the matching condition:

$$\hat{\phi}_i\big|_{r=a} = \hat{\phi}_e\big|_{r=a} . \tag{4.7}$$

$\hat{\phi}_e$ must satisfy the free surface condition (4.3), the no flux condition (4.4) at the ocean bottom as well as:

$$\left.\frac{\partial \hat{\phi}_e}{\partial r}\right|_{r=a} = z \quad (d \le z \le 1) , \tag{4.8}$$

which again means that the fluid velocity equals the buoy velocity at its side, and another matching condition

$$\left.\frac{\partial \hat{\phi}_e}{\partial r}\right|_{r=a} = \left.\frac{\partial \hat{\phi}_i}{\partial r}\right|_{r=a} \quad (0 \le z \le d) . \tag{4.9}$$

Finally, it must satisfy the radiation condition. We start by solving for the internal potential function $\hat{\phi}_i$. $\hat{\phi}_i$ has to satisfy one inhomogeneous condition (4.6) and therefore it can be expressed as the sum of a homogeneous solution $\hat{\phi}_h$ and a particular solution $\hat{\phi}_p$ such that:

$$\hat{\phi}_i = \hat{\phi}_h + \hat{\phi}_p . \tag{4.10}$$

By definition, $\hat{\phi}_p$ satisfies (4.4) and (4.6) and $\hat{\phi}_h$ must satisfy:

$$\left.\frac{\partial \hat{\phi}_h}{\partial z}\right|_{z=0 \,\&\, d} = 0 , \tag{4.11}$$

$$\hat{\phi}_h\big|_{r=a} = \left(\hat{\phi}_e - \hat{\phi}_p\right)\big|_{r=a} . \tag{4.12}$$

A particular solution is given by:

$$\hat{\phi}_p = \frac{-1}{2d}\left(z^2 r - \frac{r^3}{4}\right). \tag{4.13}$$

Now the homogeneous solution can be solved using the method of separation of the variables as before. Assume the following form:

$$\hat{\phi}_h = \psi_n(r)\xi_n(z) . \tag{4.14}$$

This gives a set of eigenfunctions of the form:

$$\xi_n = \cos(\lambda_n z) \quad (n = 0,1,2 \dots) , \tag{4.15}$$

and eigenvalues λ_n given by:

$$\lambda_n = \frac{n\pi}{d} . \tag{4.16}$$

The function ψ_n must be finite at $r = 0$. This yields a solution of the form:

$$\psi_n(r) = \begin{cases} r & (n = 0) , \\ I_1(\lambda_n r) & (n > 0) . \end{cases} \tag{4.17}$$

The homogeneous solution can therefore be written in the convenient form:

$$\hat{\phi}_h = \sum_{n=0}^{\infty} \alpha_n \frac{\psi_n(r)}{\psi_n(a)} \cos(\lambda_n z) . \tag{4.18}$$

In this equation, α_n are the Fourier coefficients. To solve for these constants, apply (4.12):

$$\alpha_n = \frac{\epsilon_n}{d} \int_0^d \hat{\phi}_e\big|_{r=a} \cos(\lambda_n z)\, dz - {\alpha_n}^*, \tag{4.19}$$

such that ϵ_n is the Jacobi symbol and,

$${\alpha_n}^* = \frac{\epsilon_n}{d} \int_0^d \hat{\phi}_p\big|_{r=a} \cos(\lambda_n z)\, dz . \tag{4.20}$$

Now moving to solve for the external potential function, if we assume

$$\hat{\phi}_e = R_k(r) Z_k(z) , \tag{4.21}$$

then the functions $R_k(r)$will be given by:

$$R_k = \begin{cases} H_1(m_0 r) & (k = 0), \\ K_1(m_k r) & (k > 0), \end{cases} \tag{4.22}$$

where H_1 and $K_1$is the first kind Hankel and second kind modified Bessel functions respectively. The depth functions $Z_k(z)$ were introduced in (2.43). The solution for the potential of the external region is therefore written conveniently as:

$$\hat{\phi}_e = \sum_{k=0}^{\infty} A_k \frac{R_k(r)}{R_k'(a)} Z_k(z). \tag{4.23}$$

The last equation represents the sum of a propagating wave (the term with $k = 0$) and an infinite number of evanescent waves ($k \geq 1$). Conditions (4.8) and (4.9) must be satisfied. That is:

$$\left.\frac{\partial \hat{\phi}_e}{\partial r}\right|_{r=a} = \sum_{k=0}^{\infty} A_k Z_k(z) = \begin{cases} \left.\frac{\partial \hat{\phi}_i}{\partial r}\right|_{r=a} & (0 \leq z \leq d)\,, \\ z & (d \leq z \leq 1). \end{cases} \tag{4.24}$$

Making use of the orthogonal properties of the Z_k functions:

$$A_k = \int_0^d \left.\frac{\partial \hat{\phi}_h}{\partial r}\right|_{r=a} Z_k(z)dz + A_k^*\,. \tag{4.25}$$

Here A_k^* is given by:

$$A_k^* = \int_0^d \left.\frac{\partial \hat{\phi}_p}{\partial r}\right|_{r=a} Z_k(z)dz + Z_k^*\,, \tag{4.26}$$

$$Z_k^* = \int_d^1 z Z_k(z)dz\,. \tag{4.27}$$

Making use of (4.18), (4.25) becomes:

$$A_k = \sum_{n=0}^{\infty} \alpha_n \frac{\psi_n'|_{r=a}}{\psi_n(a)} C_{nk} + A_k^*\,. \tag{4.28}$$

The coupling coefficient C_{nk} was defined in (2.52). Now going back to equation (4.19), and inserting the results for the external potential (4.23):

$$\alpha_n = \frac{\epsilon_n}{d} \sum_{k=0}^{\infty} A_k \frac{R_k(a)}{R_k'(a)}\, C_{nk} - {\alpha_n}^*\,. \tag{4.29}$$

Finally, (4.28) is inserted into (4.29) to yield,

$$\alpha_n = \sum_{j=0}^{\infty} e_{nj}\alpha_j \; + s_n\,, \tag{4.30}$$

$$e_{nj} = \frac{\epsilon_n}{d} \sum_{k=0}^{\infty} \frac{\psi_j'|_{r=a}}{\psi_j(a)} \frac{R_k(a)}{R_k'(a)} C_{jk} C_{nk}\,, \tag{4.31}$$

$$s_n = \frac{\epsilon_n}{d} \sum_{k=0}^{\infty} A_k^* \frac{R_k(a)}{R_k'(a)}\, C_{nk} - {\alpha_n}^*\,. \tag{4.32}$$

This system can be truncated at any number of terms depending on the accuracy of the solutions required. The coefficients A_k can then be computed using (4.28).

4.2.2 Radiation Coefficients

Now the case under question involves oscillation in pitch. For unit velocity, if B_{55} is the pitch damping coefficient and M_{55} is the corresponding added moment of inertia then:

$$\frac{M_{55} + iB_{55}/\omega}{\rho h^5} = -\iint \hat{\phi}\frac{\partial \hat{\phi}}{\partial n}\cos(\theta)^2\, dS\,. \tag{4.33}$$

Here the integral is over S, the surface area of the cylinder and $i = \sqrt{-1}$. Considering the external and internal regions separately, the integral becomes:

$$\begin{aligned}\frac{M_{55} + iB_{55}/\omega}{\rho h^5} &\\ &= \int_0^{2\pi}\int_0^a r\left(\hat{\phi}_i\frac{\partial \hat{\phi}_i}{\partial z}\right)\Big|_{z=d}\cos(\theta)^2\, dr d\theta \\ &- a\int_0^{2\pi}\int_d^1 \left(\hat{\phi}_e\frac{\partial \hat{\phi}_e}{\partial r}\right)\Big|_{r=a}\cos(\theta)^2\, dz d\theta \\ &= -\pi\int_0^a r^2\hat{\phi}_i(r,d)dr - \pi a\int_d^1 z\hat{\phi}_e(a,z)dz\,.\end{aligned} \tag{4.34}$$

Use of conditions (4.6) and (4.8) was made. The first integral can be split according to (4.10). The resulting integral is:

$$\begin{aligned}\frac{M_{55} + iB_{55}/\omega}{\pi\rho h^5} &\\ &= -\int_0^a r^2\hat{\phi}_p(r,d)dr - \int_0^a r^2\hat{\phi}_i^h(r,d)dr \\ &- a\int_d^1 z\hat{\phi}_e(a,z)dz\ .\end{aligned} \tag{4.35}$$

Using (4.13) and (4.18):

$$\mu_{55} + i\lambda_{55} = \frac{M_{55} + iB_{55}/\omega}{\pi\rho a^3 h^2}$$

$$= \left(\frac{6ad^2 - a^3}{48d}\right) - \frac{1}{a^3}\sum_{n=0}^{\infty} \alpha_n (-1)^n \psi_n^* \qquad (4.36)$$

$$- \frac{1}{a^2}\sum_{k=0}^{\infty} A_k \frac{R_k(a)}{R_k'(a)} Z_k^* ,$$

$$\psi_n^* = \int_0^a r^2 \frac{\psi_n(r)}{\psi_n(a)} dr , \qquad (4.37)$$

and Z_k^* is defined in (4.27).

4.2.3 Results and Discussion

Using Matlab, the system (4.30-32) can be solved and then the radiation coefficients can be computed from (4.36) for specified values of a, d and m_0. Some results are presented for selected values of radii a and distance to sea floor d (Figures 3.2 to 3-5).

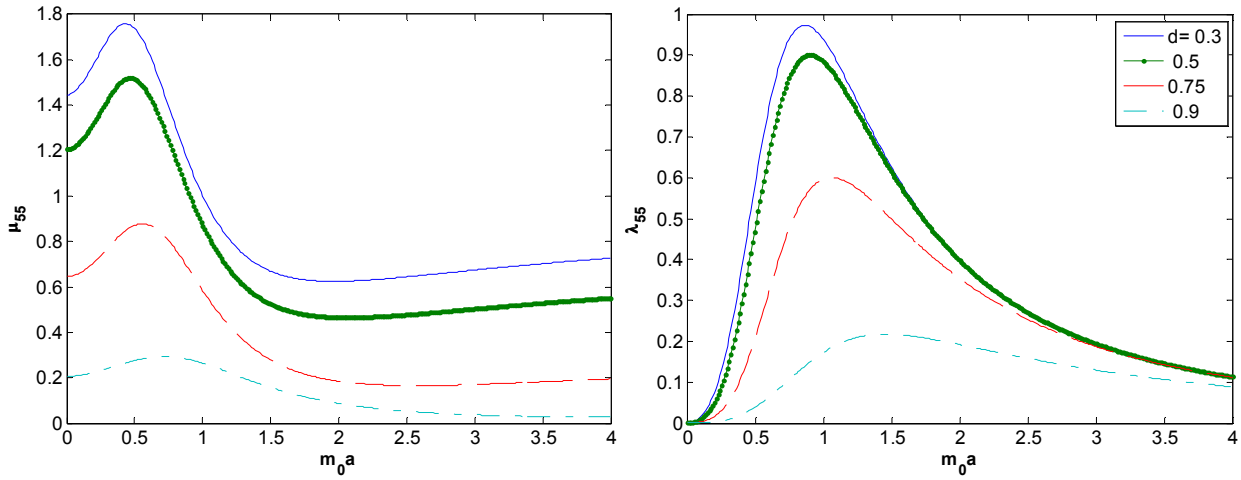

Figure 4-2: The radiation pitch added mass (left) and damping (right) coefficients for the pitching buoy system at $a/h = 0.2$ and for four floatation levels

The results show that the damping coefficient starts from 0 at low frequencies, increases and then drops to zero again at high frequencies. This is somewhat different from the results for the heave radiation where the damping has a nonzero fixed value at zero frequency. It was stated

earlier that the theoretical maximum power extraction is achieved when the PTO damping coefficient is equal to the radiation damping coefficient presented. These results indicate that this PTO optimal damping must be zero at high and low frequencies which in turn forces the power extracted to be zero at these points. This indicates the presence of an optimal frequency where the maximum power can be converted; a fact we have seen from the results of the previous section (Figures 3-4, 6).

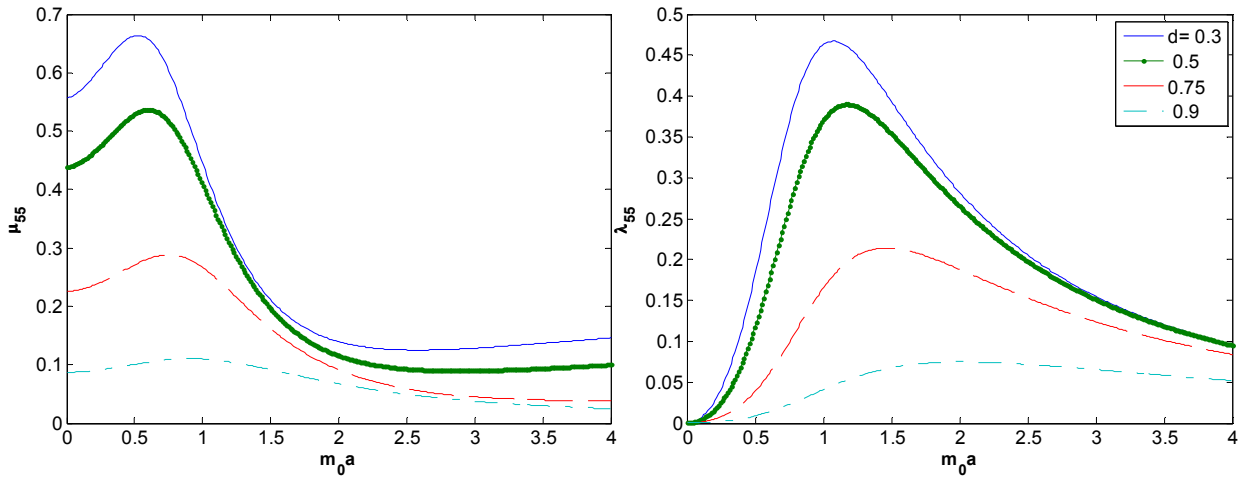

Figure 4-3: The radiation pitch added mass (left) and damping (right) coefficients for the pitching buoy system at $a/h = 0.5$ and for four floatation levels

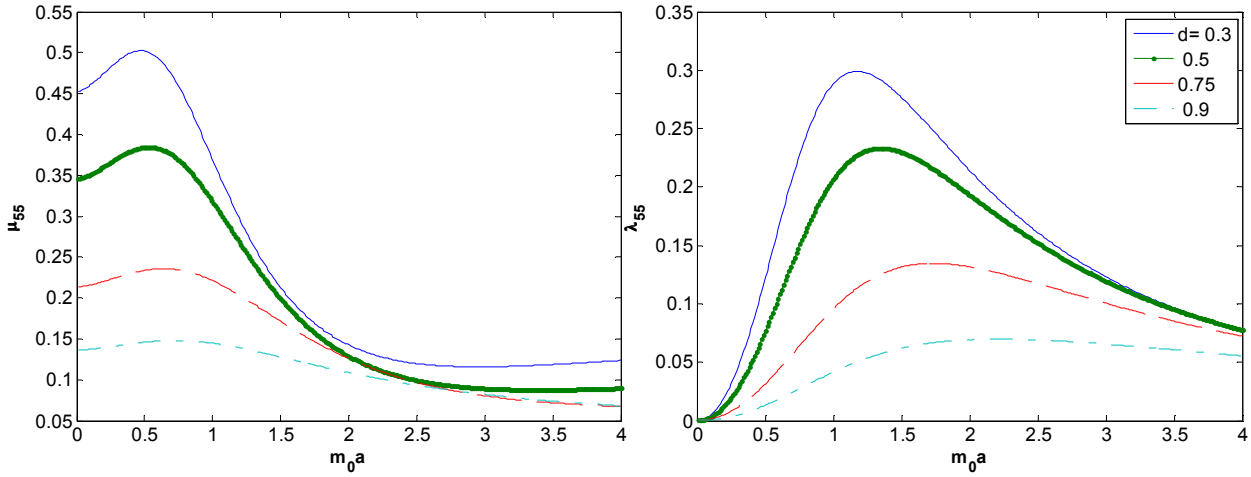

Figure 4-4: The radiation pitch added mass (left) and damping (right) coefficients for the pitching buoy system at $a/h = 1$ and for four floatation levels

The added mass starts from a finite point at low frequency (in contrast to the heave mode) and reaches a constant value at higher frequencies. The qualitative behavior is similar to the results in

[13] where the difference is the position of the center of rotation. The author of that paper also pointed out to the fact that the sway damping maximum occurs at $m_0 a \sim 1.2$ at all times. The results for pitch (or roll) are fairly similar in the cases presented here but are more complicated in general. The results show a decrease of the values of the coefficients with the increasing radius a and floatation level d but that is mainly due to the dimensionalization scheme considered.

4.3 The Pitch Diffraction Problem

As stated earlier, the diffraction problem deals with solving for the diffraction loads on a fixed body (at least within linear theory). For the case considered, we are interested in the torque on the buoy about the y-axis. We saw from the Haskind relation in part 1 how the vertical force is proportional to the square root of the radiation damping coefficient. We know that such a simple relation is possible for the asymmetric pitch problem. Therefore we expect the torque to adopt the same qualitative behavior as the pitch radiation damping coefficients in Figures (4-2, 4). In this section, the diffraction problem is solved and the mentioned torque is computed.

4.3.1 Theory

The solution for the velocity potential is the same as that of (§ 2.3). Here, it is presented in a slightly different more compact form. The Laplace equation is to be solved. Assume that ϕ varies sinusoidally with time, then it can be represented as $\phi = Re\left(\hat{\phi}(r,z,\theta)e^{-i\omega t}\right)$. The complex amplitude of the free surface elevation due to the incident wave was given in (4.2).

For the diffraction problem, since there are no inhomogeneous terms in the boundary conditions, no particular solution is needed. In this case, the internal potential $\hat{\phi}_i$ satisfies the no flux conditions (4.11) at the ocean and buoy bottom and the matching condition (4.7). The external potential, on the other hand is a summation of the diffracted and the incident wave potentials. It satisfies the free surface condition (4.3), the no flux condition (4.4), a matching

condition (4.9) as well as the radiation condition (4.5). Furthermore, the fluid must not penetrate the buoy side such that:

$$\left.\frac{\partial \hat{\phi}_e}{\partial r}\right|_{r=a} = 0 \quad (d \le z \le 1)\,. \tag{4.38}$$

Because this problem is directional in nature, symmetry considerations dictate the conditions:

$$\left.\frac{\partial \hat{\phi}_i}{\partial \theta}\right|_{\theta=0,\pi} = 0\,, \tag{4.39}$$

$$\left.\frac{\partial \hat{\phi}_e}{\partial \theta}\right|_{\theta=0,\pi} = 0\,. \tag{4.40}$$

The resulting form of the internal potential is a summation of the functions:

$$\hat{\phi}_{pn} = \psi_{pn}(r)\cos(\lambda_n z)\cos(p\theta), \tag{4.41}$$

$$\lambda_n = n\pi/d \text{ and } p = 0,1,2\ldots. \tag{4.42}$$

The modal functions ψ_{pn} are given by:

$$\psi_{pn} = \begin{cases} r^p & n = 0\,, \\ I_p(\lambda_n r) & n > 0\,, \end{cases} \tag{4.43}$$

where I_p is the modified Bessel functions of p^{th} order and of the first kind. The solutions presented were chosen to be finite at $r = 0$. The internal potential is now given (in a more suitable form) by:

$$\hat{\phi}_i = \zeta_0 \sum_{p=0}^{\infty}\sum_{n=0}^{\infty} \alpha_{pn}\varepsilon_{pn}\frac{\psi_{pn}(r)}{\psi_{pn}(a)}\cos(\lambda_n z)\cos(p\theta). \tag{4.44}$$

$$\varepsilon_{pn} = \frac{\epsilon_p \epsilon_n}{2\pi d}\,, \tag{4.45}$$

and ζ_0 is the incident wave amplitude. Condition (4.7) must be satisfied as well which leads to:

$$\alpha_{pn} = \frac{1}{\zeta_0}\int_0^d\int_0^{2\pi} \hat{\phi}_e\big|_{r=a}\cos(\lambda_n z)\cos(p\theta)\,d\theta dz\,. \tag{4.46}$$

The external potential is the sum of the potentials of the incident wave (4.2) and the diffracted wave written conveniently as:

$$\begin{aligned}\hat{\phi}_e = -\zeta_0 \sum_{k=0}^{\infty} \epsilon_k i^{k+1} \big(J_k(m_0 r) \\ - \frac{J_k'(m_0 a)}{H_k'(m_0 a)} H_k(m_0 r)\big) \cos(k\theta) \frac{Z_0(z)}{Z_0'(1)} \\ + \zeta_0 \sum_{j=0}^{\infty} \sum_{k=0}^{\infty} A_{kj} \frac{R_{kj}(r)}{R_{kj}'(a)} Z_j(z) \cos(k\theta).\end{aligned} \tag{4.47}$$

Here $Z_j(z)$ are given in (2.43). The functions $R_{kj}(r)$ that satisfy the radiation condition or are finite at an infinite distance from the body are given in (2.80).

Conditions (4.9) and (4.38) must be satisfied:

$$\begin{aligned}\left.\frac{\partial \hat{\phi}_e}{\partial r}\right|_{r=a} &= \zeta_0 \sum_{j=0}^{\infty} \sum_{k=0}^{\infty} A_{kj} Z_j(z) \cos(k\theta) \\ &= \begin{cases} 0 & (d \le z \le 1), \\ \dfrac{\partial \hat{\phi}_i(a,z,\theta)}{\partial r} & (0 \le z \le d). \end{cases}\end{aligned} \tag{4.48}$$

The unknown coefficients are then given by:

$$A_{kj} = \frac{\epsilon_k}{2\pi\zeta_0} \int_0^{2\pi} \int_0^{d} \left.\frac{\partial \hat{\phi}_i}{\partial r}\right|_{r=a} Z_j(z) \cos(k\theta)\, dz d\theta\,. \tag{4.49}$$

Now inserting the value of the internal potential function from (4.44) and integrating,

$$A_{kj} = \sum_{n=0}^{\infty} \varepsilon_{kn} \frac{\psi_{kn}'(a)}{\psi_{kn}(a)} C_{nj} \alpha_{kn}\,, \tag{4.50}$$

where the coupling coefficient C_{nj} was defined in (2.52). Inserting the value of the external potential (4.47) into (4.46) and simplifying then,

$$\alpha_{pn} - \alpha_{pn}^* = \frac{2\pi}{\epsilon_p} \sum_{j=0}^{\infty} A_{pj} \frac{R_{pj}(a)}{R_{pj}'(a)} C_{nj}\,, \tag{4.51}$$

$$\alpha_{pn}^{*} = \frac{4i^{p}}{aH_{p}'(m_0 a)Z_0'(1)} C_{n0} \,. \tag{4.52}$$

Here, use of the Wronskian relation is made:

$$J_k(m_0 a)H_k'(m_0 a) - J_k'(m_0 a)H_k(m_0 a) = \frac{2i}{\pi a} \,. \tag{4.53}$$

Finally inserting (4.50) into (4.51),

$$\alpha_{pn} = \sum_{l=0}^{\infty} e_{pnl}\alpha_{pl} + \alpha_{pn}^{*} \,, \tag{4.54}$$

$$e_{pnl} = \sum_{j=0}^{\infty} \frac{\epsilon_l}{d} \frac{R_{pj}(a)}{R_{pj}'(a)} \frac{\psi_{pl}'(a)}{\psi_{pl}(a)} C_{lj} C_{nj} \,. \tag{4.55}$$

This is a system of equations in the unknowns α_{pn} that needs to be solved.

4.3.2 Torques on the Cylinder

The torque on the buoy about the y axis is the real part of $\hat{T}e^{-i\omega t}$ where $\hat{T}$ is a complex amplitude which has contributions from a side torque $\hat{T}_s$ and a bottom torque $\hat{T}_b$ given by an integration of the fluid pressure on the body surface. Starting with the side torque:

$$\frac{\hat{T}_s}{\rho h^5 \omega^2} = -ia \int_0^{2\pi} \int_d^1 z\hat{\phi}_e\big|_{r=a} \cos(\theta)\, dz\, d\theta \,, \tag{4.56}$$

Inserting the expression for the external potential from (4.47) and using the relation (4.53):

$$\frac{\hat{T}_s}{\rho h^3 \omega^2 \zeta_0 a} = i \int_d^1 z \left[\left(\frac{-4i}{a H_1'(m_0 a)} \right) \frac{Z_0(z)}{Z_0'(1)} - \pi \sum_{j=0}^{\infty} A_{1j} \frac{R_{1j}(a)}{R_{1j}'(a)} Z_j(z) \right] dz \tag{4.57}$$

$$= \left(\frac{4}{a H_1'(m_0 a) Z_0'(1)} \right) Z_0^* - i\pi \sum_{j=0}^{\infty} A_{1j} \frac{R_{1j}(a)}{R_{1j}'(a)} Z_j^* .$$

Z_j^* was defined in (4.27). Finally, it is written as:

$$\frac{\hat{T}_s}{Ba} = \left(\frac{4v}{\pi a^3 H_1'(m_0 a) Z_0'(1)} \right) Z_0^* - \frac{iv}{a^2} \sum_{j=0}^{\infty} A_{1j} \frac{R_{1j}(a)}{R_{1j}'(a)} Z_j^* , \tag{4.58}$$

where B is the buoyancy force $B = \pi \rho a^2 g \zeta_0$. The bottom torque is

$$\frac{\hat{T}_b}{\rho h^5 \omega^2} = -i \int_0^{2\pi} \int_0^a r^2 \hat{\phi}_i(r, d, \theta) \cos(\theta) dr \, d\theta$$

$$= \frac{i\zeta_0}{d} \sum_{n=0}^{\infty} \alpha_{1n} \epsilon_n (-1)^{n+1} \psi_n^* , \tag{4.59}$$

where ψ_n^* was defined in (4.37). In terms of buoyancy:

$$\frac{\hat{T}_b}{Ba} = \frac{iv}{\pi a^3 d} \sum_{n=0}^{\infty} \alpha_{1n} \epsilon_n (-1)^{n+1} \psi_n^* . \tag{4.60}$$

Since only α_{1n} are required to solve for the vertical force, then the system to solve reduces from (4.54-55) to one system in α_{1n}.

4.3.3 Results and Discussion

The torque amplitude and phase results obtained are plotted in Figures (4-5, 6, and 7) for the three radius values of 0.2, 0.5 and 1. The results are qualitatively similar to those in [21] in terms of amplitude and phase. The amplitude rises from no torque at zero frequency to a maximum and then down to zero at a large enough frequency. This is in accordance with the results for the

pitch damping coefficients in Figures 4-2 to 4-4. The torque is seen to lag the wave by $\pi/2$ (or is in phase with the negative wave slope) at zero frequency. This follows from the fact that fluid particles move in circular trajectories and their horizontal motion is 90º out of phase with the vertical motion. The torque is expected to have the phase of the horizontal forces. Again the jump of 2π in the phase is just to keep the values within the range $[-\pi, \pi]$.

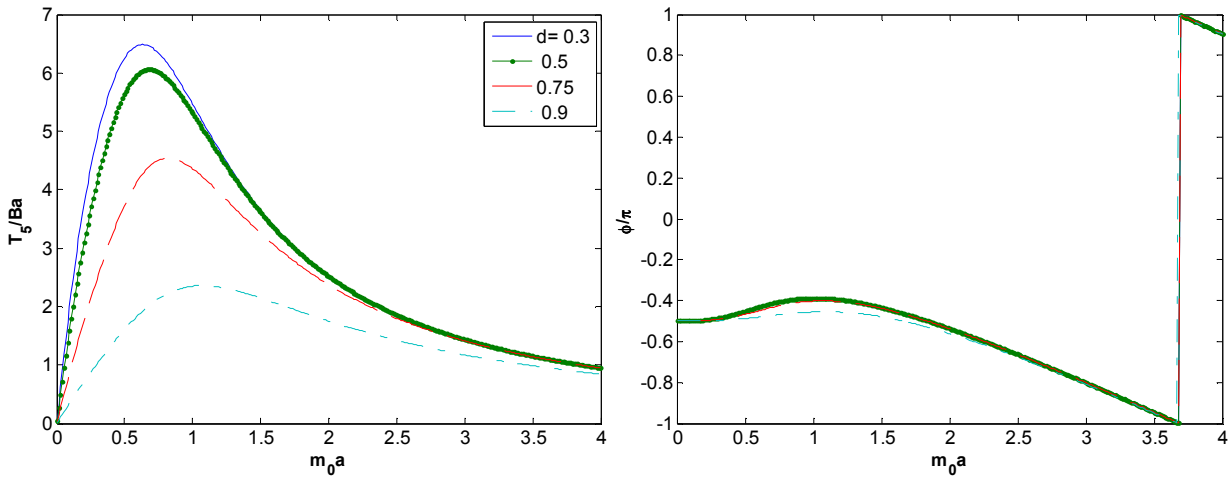

Figure 4-5: The excitation torque amplitude (left) and phase divided by π (right) for the pitching buoy system at $a/h = 0.2$ and for four floatation levels Excitation

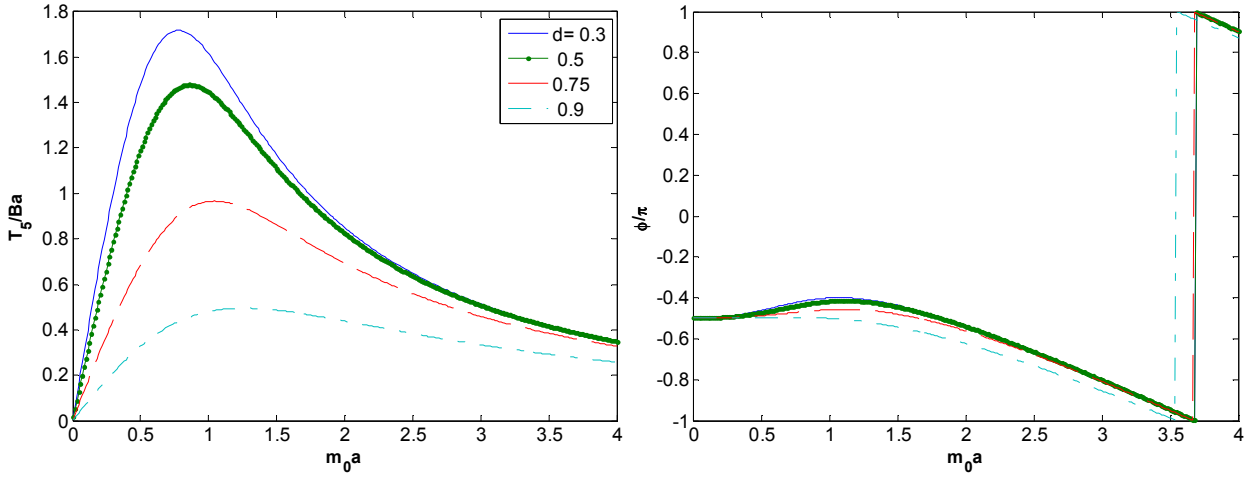

Figure 4-6: The excitation torque amplitude (left) and phase divided by π (right) for the pitching buoy system at $a/h = 0.5$ and for four floatation levels Excitation

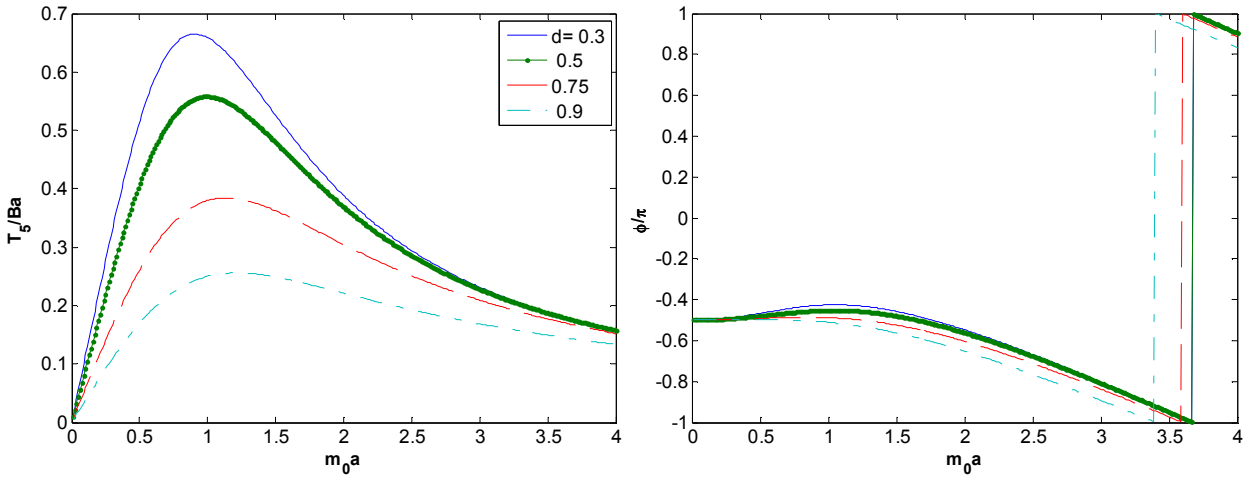

Figure 4-7: The excitation torque amplitude (left) and phase divided by π (right) for the pitching buoy system at $a/h = 1$ and for four floatation levels Excitation

4.3.4 The Haskind Relation

The results for the torque look reasonable, but further verification is required to make sure that no mistake was done. The Haskind relation can be used to compute the pitch excitation moment from a knowledge of the pitch potential derived in section 4.2. By comparing the results from this relation to those from the diffraction problem, verification of the results is possible. Furthermore, the Haskind relation provides a means that does not require solving the whole diffraction problem to obtain the wave loads, which saves lots of computational effort given that the radiation problem is already solved. The external pitch radiation potential for unit velocity is given by:

$$\hat{\phi}_5 \cos(\theta) = \frac{2A_0}{m_0} \frac{Z_0(z)\cos(\theta)}{\left(H_0^{(1)}(m_0 a) - H_2^{(1)}(m_0 a)\right)} H_1^{(1)}(m_0 r) - \sum_{k=1}^{\infty} \frac{2A_k}{m_k} \frac{K_1(m_k r) Z_k(z)\cos(\theta)}{\left(K_0(m_k a) + K_2(m_k a)\right)}. \tag{4.61}$$

In the limit of infinite distance from the body, the series above dies out exponentially and the far field form is:

$$\lim_{r\to\infty} \hat{\phi}_5 = A^* \cosh(m_0 z) \frac{e^{im_0 r}}{\sqrt{r}} + O\left(\frac{1}{r}\right), \tag{4.62}$$

$$A^* = \frac{2A_0/(m_0\sqrt{N_0})}{(H_0^{(1)}(m_0 a) - H_2^{(1)}(m_0 a))} \sqrt{\frac{2}{\pi m_0}} e^{-i3\pi/4}. \tag{4.63}$$

The potential gradient radial component in the far field becomes:

$$\lim_{r\to\infty} \frac{\partial \hat{\phi}_5}{\partial r} = A^* \cosh(m_0 z) \left(im_0 - \frac{1}{2r}\right) \frac{e^{im_0 r}}{\sqrt{r}}. \tag{4.64}$$

$\hat{\phi}^I$ is the incident wave velocity potential given by:

$$\hat{\phi}^I = -\frac{i\zeta_0}{m_0} \frac{\cosh(m_0 z)}{\sinh(m_0)} e^{im_0 r cos(\theta)}. \tag{4.65}$$

Its gradient component in the radial direction is also needed and is given by:

$$\frac{\partial \hat{\phi}^I}{\partial r} = \zeta_0 \frac{\cosh(m_0 z)}{\sinh(m_0)} \cos(\theta)\, e^{im_0 r cos(\theta)}. \tag{4.66}$$

Now, if $\hat{T}$ is the excitation torque then the Haskind relation states that:

$$\frac{\hat{T}}{\omega^2 h^5 \rho} = \frac{F_5^D}{\omega^2 h^5 \rho} = -i \iint_{A_\infty} \left(\hat{\phi}^I \frac{\partial \hat{\phi}_5}{\partial n} - \hat{\phi}_5 \frac{\partial \hat{\phi}^I}{\partial n}\right) \cos(\theta)\, dA. \tag{4.67}$$

Here the integration is over an imaginary cylindrical surface with infinite radius. F_5^D is the fifth component of the generalized force vector and corresponds to the pitch torque from the diffraction problem. The vertical force in Chapter 2 would have been called F_3^D corresponding to heave. For our case, the relation simplifies to (keeping in mind the limit):

$$\begin{aligned} \frac{\hat{T}}{\omega^2 h^5 \rho} &= -i \int_0^1 \int_0^{2\pi} \left(\hat{\phi}^I \frac{\partial \hat{\phi}_5}{\partial r} - \hat{\phi}_5 \frac{\partial \hat{\phi}^I}{\partial r}\right) r \cos(\theta)\, d\theta dz \\ &= \hat{T}_1 + \hat{T}_2, \end{aligned} \tag{4.68}$$

Using (4.64-65) and integrating over depth, the first part of the above integral becomes:

$$\hat{T}_1 = -i\int_0^1\int_0^{2\pi}\left(\hat{\phi}^I\frac{\partial\hat{\phi}_5}{\partial r}\right)r\cos(\theta)\,d\theta dz$$
$$= \frac{-\zeta_0 A^* N_0}{m_0\sinh(m_0)}\int_0^{2\pi}\sqrt{r}\left(im_0 - \frac{1}{2r}\right)\cos(\theta)\,e^{im_0 r(1+cos(\theta))}d\theta\,. \tag{4.69}$$

The second term in the parenthesis drops out in the limit. Using (4.63, 66), $\hat{T}_2$ becomes:

$$\hat{T}_2 = i\int_0^1\int_0^{2\pi}\left(\hat{\phi}_5\frac{\partial\hat{\phi}^I}{\partial r}\right)r\cos(\theta)\,d\theta dz$$
$$= \frac{i\zeta_0 A^* N_0}{\sinh(m_0)}\int_0^{2\pi}\sqrt{r}\cos(\theta)^2\left(e^{im_0 r(1+cos(\theta))}\right)d\theta\,. \tag{4.70}$$

Adding these and using the method of stationary phase [5]:

$$\frac{\hat{T}}{\omega^2 h^5\rho} = \frac{-i\zeta_0 A^* N_0}{\sinh(m_0)}\int_0^{2\pi}\sqrt{r}\cos(\theta)\,(1-\cos(\theta))e^{im_0 r(1+cos(\theta))}d\theta$$
$$= \frac{2i\zeta_0 A^* N_0}{\sinh(m_0)}\sqrt{\frac{2\pi}{m_0}}e^{\frac{i\pi}{4}}\,. \tag{4.71}$$

Finally inserting the value of A^* from (4.63),

$$\frac{\hat{T}}{Ba} = \frac{8vA_0\sqrt{N_0}}{\pi a^3 m_0^2(H_0^{(1)}(m_0 a) - H_2^{(1)}(m_0 a))\sinh(m_0)}\,. \tag{4.72}$$

The results from this relation and from the diffraction problem were found to match perfectly.

4.4 Surge-Pitch Coupling Coefficients

We now move to solve for the coupling hydrodynamic coefficients, namely $M_{51} = M_{15}$ and $B_{51} = B_{15}$ between the surge and the pitch modes only since heave is independent of the other motions. Here,

$$\mu_{51} + i\lambda_{51} = \frac{M_{51} + iB_{51}/\omega}{\pi\rho h a^3}$$

$$= -\frac{1}{a^3\pi}\int_d^1 \int_0^{2\pi} \hat{\phi}_5 \frac{\partial \hat{\phi}_1}{\partial r}\bigg|_{r=a} \cos(\theta)^2 \, a d\theta dz \tag{4.73}$$

$$= -\frac{1}{a^2}\int_d^1 \hat{\phi}_5(a,z)dz = -\frac{1}{a^2}\sum_{k=0}^{\infty} A_k \frac{R_k(a)}{R_k'(a)}\Gamma_k^*,$$

$$\Gamma_k^* = \int_d^1 Z_k(z)dz\,. \tag{4.74}$$

Here are some of the results that are qualitatively very similar to those of the pitch radiation problem.

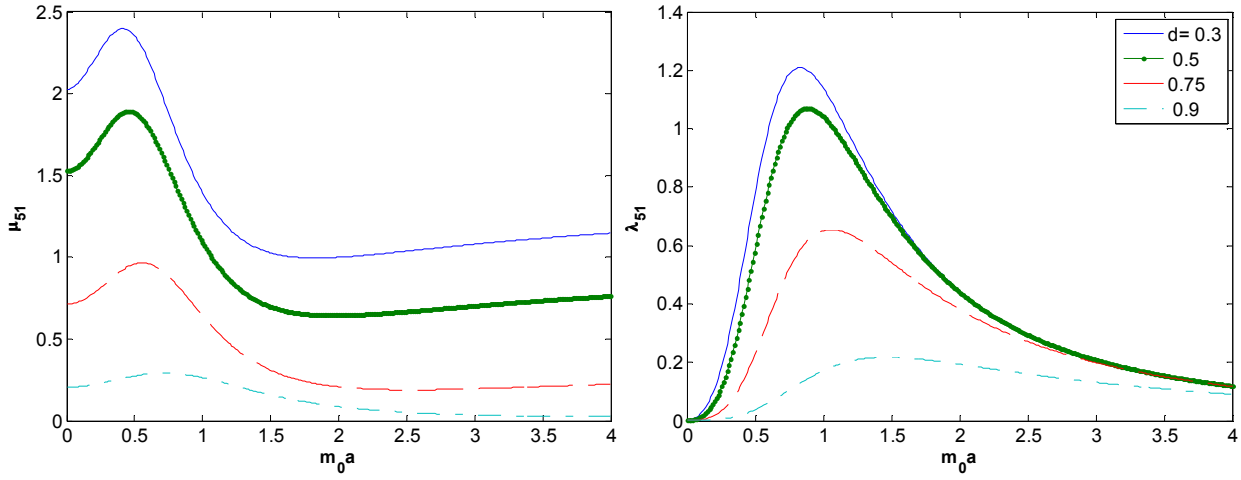

Figure 4-8: The pitch-surge coupling added mass (left) and damping coefficient (right) for the pitching buoy system at $a/h = 0.2$ and for four floatation levels Excitation

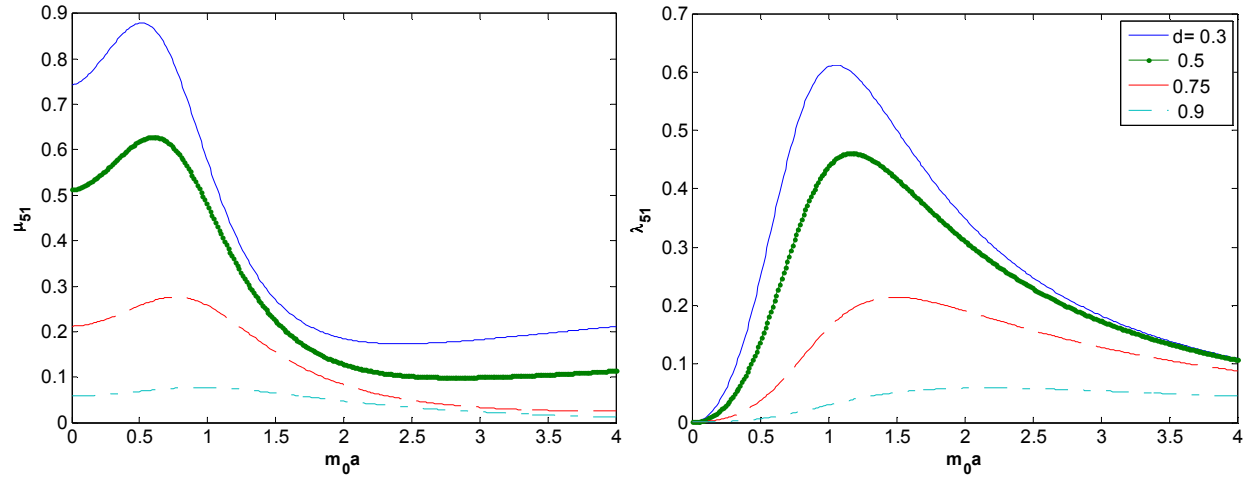

Figure 4-9: The pitch-surge coupling added mass (left) and damping coefficient (right) for the pitching buoy system at $a/h = 0.5$ and for four floatation levels Excitation

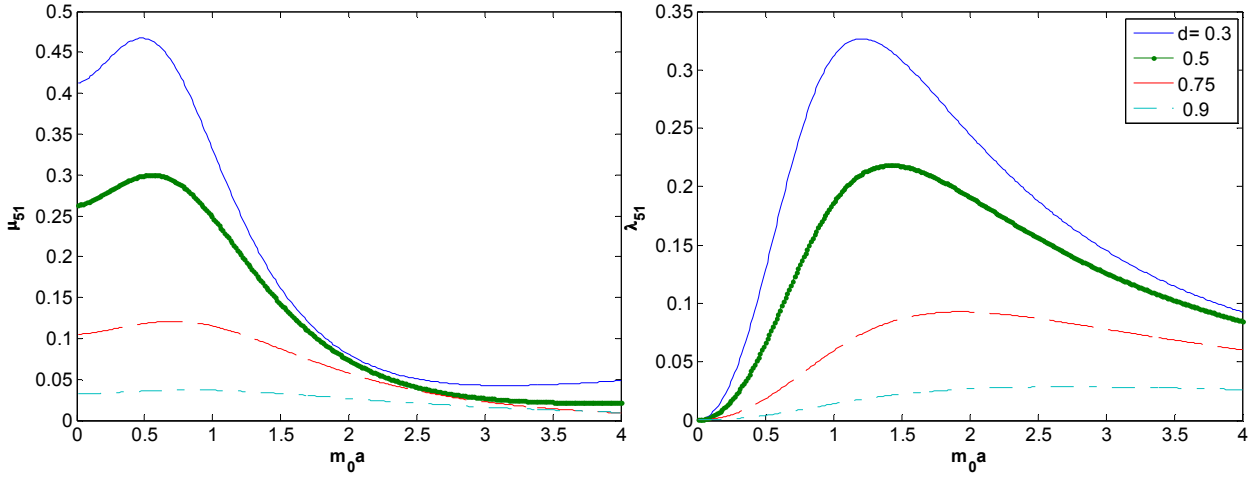

Figure 4-10: The pitch-surge coupling added mass (left) and damping coefficient (right) for the pitching buoy system at $a/h = 1$ and for four floatation levels Excitation

4.5 Appendices

Appendix 4.A

Evaluation of Different Expressions from Chapter 4

These are the expressions presented in Chapter 4 and not fully evaluated for brevity.

From (4.20),

$$\alpha_n{}^* = -\frac{\epsilon_n}{d}\int_0^d \frac{1}{2d}\left(z^2 a - \frac{a^3}{4}\right)\cos(\lambda_n z)\,dz$$

$$= \begin{cases} -\dfrac{ad}{6} + \dfrac{a^3}{8d} & (n=0), \\ -\dfrac{2a}{d}\dfrac{(-1)^n}{\lambda_n^2} & (n>0). \end{cases} \tag{4.A.1}$$

From (4.27),

$$Z_k^*$$

$$= \begin{cases} \dfrac{1}{m_0^2\sqrt{N_0}}(\cosh(m_0 d) - m_0 d\sinh(m_0 d) - \cosh(m_0) + m_0\sinh(m_0)) & (k=0), \\ \dfrac{1}{m_k^2\sqrt{N_k}}(\cos(m_k) + m_k\sin(m_k) - \cos(m_k d) - m_k d\sin(m_k d)) & (k>0). \end{cases} \tag{4.A.}$$

From (4.26),

$$A_k^* = \frac{-1}{2d}\int_0^d (z^2 - \frac{3}{4}a^2)Z_k(z)dz + Z_k^*\,. \tag{4.A.3}$$

For $k = 0$,

$$A_0^* = \frac{-1}{2d\sqrt{N_0}}\int_0^d (z^2 - \frac{3}{4}a^2)\cosh(m_0 z)dz + Z_0^*$$

$$= \frac{-1}{8d\sqrt{N_0}}\left(\frac{(4m_0^2 d^2 - 3a^2 m_0^2 + 8)\sinh(m_0 d) - 8m_0 d\cosh(m_0 d)}{m_0^3}\right) + Z_0^*$$

$$= \frac{16m_0 d\cosh(m_0 d) + 8m_0^2 d\sinh(m_0) - 8m_0 d\cosh(m_0) - (12m_0^2 d^2 - 3m_0^2 a^2 + 8)\sinh(m_0 d)}{8m_0^3 d\sqrt{N_0}},$$

And for $k > 0$,

$$A_k^* = \frac{-1}{2d\sqrt{N_k}} \int_0^d (z^2 - \frac{3}{4}a^2)\cos(m_k z)dz + Z_k^*$$

$$= \frac{-1}{8d\sqrt{N_k}} \left(\frac{(4m_k^2 d^2 - 3a^2 m_k^2 - 8)\sin(m_k d) + 8m_k d\cos(m_k d)}{m_k^3} \right) + Z_k^*$$

$$= \frac{-16m_k d\cos(m_k d) + 8m_k^2 d\sin(m_k) + 8m_k d\cos(m_k) - (12m_k^2 d^2 - 3m_k^2 a^2 - 8)\sin(m_k d)}{8m_k^3 d\sqrt{N_k}}.$$

From (4.37),

$$\psi_n^* = \begin{cases} \int_0^a \frac{r^3}{a} dr = \frac{a^3}{4} & (n = 0), \\ \int_0^a r^2 \frac{I_1(\lambda_n r)}{I_1(\lambda_n a)} dr = \frac{a^2 I_2(\lambda_n a)}{\lambda_n I_1(\lambda_n a)} & (n > 0). \end{cases} \tag{4.A.4}$$

From (4.52),

$$\alpha_{1n}^* = \frac{8\sqrt{N_0}i}{am_0^2\left(H_0^1(m_0 a) - H_2^1(m_0 a)\right)\sinh(m_0)} C_{n0}\,. \tag{4.A.5}$$

Finally from (4.74),

$$\Gamma_k^* = \begin{cases} \frac{\sinh(m_0) - \sinh(m_0 d)}{m_0\sqrt{N_0}} & (k = 0), \\ \frac{\sin(m_k) - \sin(m_k d)}{m_k\sqrt{N_k}} & (k > 0). \end{cases} \tag{4.A.6}$$

Chapter 5 Power Output from Regular and Irregular Waves

The previous chapter studied the hydrodynamics of a cylinder pitching in the vertical plane about an axis perpendicular to that plane and passing through the origin. The chapter also studied the torque caused by an incident wave about that same axis when the body is held stationary. The parameters of the pitch problem are therefore available. Those of the heave problem were discussed in part one of this work while those of the surge problem can be found in the literature ([13][21]). The required elements to solve for the power are now in hand. This chapter deals with the power output of the buoy that is oscillating in surge, heave and pitch. It is very important to consider in advance how beneficial it may be to employ these added modes. As stated earlier, a statistical distribution is the closest theoretical approximation of real conditions. It is therefore desirable to know the power output of a WEC in such a simulated sea state. So how does our system perform in irregular waves? The chapter starts by presenting the dynamic equations of motion and the equation of the power output from regular waves. It also presents the power output of the device in irregular waves described by a Pierson-Moskowitz spectrum. The chapter ends with a comparison of this configuration with the case when motion is restricted to heave. In fact, the theme of the chapter is more about the power contribution from the pitch mode and how viable that is.

5.1 Power Output from a Single Wave

As stated earlier, evaluating the power from regular waves has a theoretical as well as experimental significance. For linear problems, the first step in computing the power from irregular waves must start with the power output from regular waves. The body under consideration is symmetric about the vertical axis and an analysis of its motion in a plane will suffice to compute the power. The problem dynamic force balance can simply be stated by (taken from [5]):

$$(\mathbf{M} + \mathbf{M^a})\frac{d^2U}{dt^2} + \mathbf{B^a}\frac{dU}{dt} + \mathbf{C}U = F^D + F\,. \tag{5.1}$$

Here,

$$U = [U_1, U_3, U_5]^T. \tag{5.2}$$

U_i is the displacement in the i^{th} direction (surge, heave and pitch). The mass matrix $\mathbf{M}$ is:

$$\mathbf{M} = \begin{bmatrix} M & 0 & Mz_m \\ 0 & M & -Mx_m \\ Mz_m & -Mx_m & I_{xx} + I_{zz} \end{bmatrix}, \tag{5.3}$$

where M is the buoy mass, x_m and z_m are the coordinates of the center of mass and $I_{xx} + I_{zz}$ is the mass moment of inertia about the y-axis (axis of rotation). The double subscript notation denotes the second moment with the subscript value to be the moment arm. The hydrodynamic added mass and damping matrices are given by:

$$\mathbf{M^a} = \begin{bmatrix} M_{11} & 0 & M_{15} \\ 0 & M_{33} & 0 \\ M_{51} & 0 & M_{55} \end{bmatrix}, \tag{5.4}$$

$$\mathbf{B^a} = \begin{bmatrix} B_{11} & 0 & B_{15} \\ 0 & B_{33} & 0 \\ B_{51} & 0 & B_{55} \end{bmatrix}. \tag{5.5}$$

The stiffness matrix is:

$$\mathbf{C} = \begin{bmatrix} 0 & 0 & 0 \\ 0 & \rho g A & -\rho g I_x^A \\ 0 & -\rho g I_x^A & \rho g (I_{xx}^A + I_z^V) - Mgz_m \end{bmatrix}. \tag{5.6}$$

Here A is the buoy cross section piercing the water surface, while V is the submerged volume of the body. The excitation force vector F^D is:

$$F^D = [F_1^D, F_3^D, F_5^D]. \tag{5.7}$$

F is the external force vector which includes forces from the power takeoff mechanisms and mooring line. Let H be the buoy height (not draft) then,

$$M = \rho\pi a^2 H = \rho A H\,, \tag{5.8}$$

$$\begin{cases} x_m = 0\,, \\ z_m = d + \dfrac{H}{2}\,. \end{cases} \tag{5.9}$$

If V_t is the total volume of the buoy (not just the submerged part):

$$\begin{aligned} I_{xx} + I_{zz} &= \int (x^2 + z^2)dm = \rho \iiint_{V_t} (x^2 + z^2)dV_t \\ &= \rho \int_d^{d+H} \int_0^a \int_0^{2\pi} (r^2\, cos(\theta)^2 + z^2) r d\theta dr dz \\ &= M\left(\frac{H^2}{3} + Hd + d^2 + \frac{a^2}{4}\right), \end{aligned} \tag{5.10}$$

$$I_x^A = \int x dA = \int_0^a \int_0^{2\pi} r^2\, cos(\theta)\, d\theta dr = 0\,, \tag{5.11}$$

$$I_{xx}^A = \int x^2 dA = \int_0^a \int_0^{2\pi} (r\, cos(\theta))^2 r d\theta dr = \frac{\pi a^4}{4}\,, \tag{5.12}$$

$$I_z^V = \int z dV = \int_d^1 \int_0^a \int_0^{2\pi} z r d\theta dr dz = \frac{\pi a^2}{2}(1 - d^2). \tag{5.13}$$

Now, all the parameters that needed to solve for the displacement are ready. The matrix equation (5.1), in the frequency domain, becomes:

$$\{-\omega^2(\mathbf{M} + \mathbf{M^a}) + \mathbf{C} - i\omega\mathbf{B^a}\}\hat{U} = \hat{F}^D + \hat{F}\,. \tag{5.14}$$

We consider the forces from two power takeoff mechanisms, one acting on the heave oscillation and the other on the pitch oscillation. These are modeled as linear dashpots. The mooring cable also exerts some tension on the buoy and can be modeled by a spring for simplicity. The external force vector can therefore be written in terms of the displacement vector $\hat{U}$ as:

$$\hat{F} = -\begin{bmatrix} 0 & 0 & 0 \\ 0 & k_3 - i\omega c_3 & 0 \\ 0 & 0 & -i\omega c_5 \end{bmatrix}\hat{U} = -\boldsymbol{\mathcal{F}}\hat{U}, \tag{5.15}$$

Simply written:

$$\mathbf{K}\widehat{U} = \{-\omega^2(\mathbf{M} + \mathbf{M^a}) + \mathbf{C} - i\omega\mathbf{B^a} + \boldsymbol{\mathcal{F}}\}\widehat{U} = \widehat{F}^D \,. \tag{5.16}$$

Here, the matrix **K** is given by:

$$\mathbf{K} = -\omega^2\begin{bmatrix} M + M_{11} & 0 & Mz_m + M_{15} \\ 0 & M + M_{33} - \dfrac{\rho g A - k_3}{\omega^2} & 0 \\ Mz_m + M_{51} & 0 & I_{xx} + I_{zz} + M_{55} - \dfrac{\rho g(I_{xx}^A + I_z^V) - Mgz_m}{\omega^2} \end{bmatrix} - i\omega\begin{bmatrix} B_{11} & 0 & B_{15} \\ 0 & B_{33} + c_3 & 0 \\ B_{51} & 0 & B_{55} + c_5 \end{bmatrix}. \tag{5.17}$$

Define the following dimensionless parameters:

$$\varsigma_m = \frac{z_m}{h}\,, \qquad f_1, f_3, f_5 = \frac{F_1^D, F_3^D, F_5^D/h}{\omega^2\rho\pi a^3\zeta_0}\,,$$

$$\lambda_{11}, \lambda_{33}, \lambda_3, \lambda_5, \lambda_{51}, \lambda_{55} = \frac{B_{11}, B_{33}, c_3, c_5, B_{51}/h, B_{55}/h^2}{\omega\rho\pi a^3}\,,$$

$$\mu, \mu_{11}, \mu_{33}, \mu_{51}, \mu_{55} = \frac{M, M_{11}, M_{33}, M_{51}/h, M_{55}/h^2}{\rho\pi a^3},$$

$$\eta_0^A, \eta_3 = \frac{(\rho g A), k_3}{\omega^2\rho\pi a^3}\,, \qquad \eta_{xx} + \eta_{zz} = \frac{I_{xx} + I_{zz}}{\rho\pi a^3 h^2}\,, \quad \eta_{xx}^A + \eta_z^V = \frac{I_{xx}^A + I_z^V}{\pi a^3\omega^2 h^2/g}\,,$$

where ζ_0 is the amplitude of the incident wave. The equations of motion can be finally summarized:

$$\kappa\varsigma = f, \tag{5.18}$$

$$\kappa = -\begin{bmatrix} \mu + \mu_{11} & 0 & \mu\varrho_m + \mu_{15} \\ 0 & \mu + \mu_{33} - \eta_0^A - \eta_3 & 0 \\ \mu\xi_m + \mu_{51} & 0 & \eta_{xx} + \eta_{zz} + \mu_{55} - \eta_{xx}^A - \eta_z^V + \mu\varrho_m/v \end{bmatrix} - i\begin{bmatrix} \lambda_{11} & 0 & \lambda_{15} \\ 0 & \lambda_{33} + \lambda_3 & 0 \\ \lambda_{51} & 0 & \lambda_{55} + \lambda_5 \end{bmatrix}, \tag{5.19}$$

$$\varsigma = [\varsigma_1\ \varsigma_3\ \varsigma_5]^T = \left[\frac{U_1}{\zeta_0}, \frac{U_3}{\zeta_0}, \frac{U_5}{\zeta_0/h}\right]^T , \tag{5.20}$$

$$f = [f_1\ f_3\ f_5]^T . \tag{5.21}$$

The useful power extracted from the mechanisms is:

$$P = \frac{1}{2} c_3 \omega^2 |U_3|^2 + \frac{1}{2} c_5 \omega^2 |U_5|^2 , \tag{5.22}$$

If we use the shallow water velocity

$$V_s = \sqrt{hg} , \tag{5.23}$$

The power expression becomes

$$\frac{P}{\frac{\pi}{2}\rho V_s^3 \zeta_0^2} = v^{3/2} \bar{a}^3 (\lambda_3 |\varsigma_3|^2 + \lambda_5 |\varsigma_5|^2) . \tag{5.24}$$

The right hand side is related to the frequency and the radius through the power only. For power per unit mass, I suggest,

$$\frac{P}{MV_s^3 \zeta_0^2/(2h^3)} = \frac{\bar{a} v^{3/2}}{(1-\bar{d})} (\lambda_3 |\varsigma_3|^2 + \lambda_5 |\varsigma_5|^2) . \tag{5.25}$$

If we write $\kappa = [\kappa_{ij}]$ such that $(i,j) = (1,3,5)$ then the displacements are given by:

$$\varsigma_1 = \frac{f_5\kappa_{15} - f_1\kappa_{55}}{\kappa_{15}\kappa_{51} - \kappa_{11}\kappa_{55}} , \qquad \varsigma_3 = \frac{f_3}{\kappa_{33}} , \qquad \varsigma_5 = \frac{f_5\kappa_{11} - f_1\kappa_{51}}{\kappa_{15}\kappa_{51} - \kappa_{11}\kappa_{55}} . \tag{5.26}$$

The heave displacement amplitude is simply:

$$|\varsigma_3|^2 = \left|\frac{f_3}{\kappa_{33}}\right|^2 = \frac{|f_3|^2}{(\mu + \mu_{33} - \eta_0^A - \eta_3)^2 + (\lambda_{33} + \lambda_3)^2} , \tag{5.27}$$

and using the fact that $\lambda_{51} = \lambda_{15}$ and $\mu_{51} = \mu_{15}$, the pitch displacement amplitude can be written as:

$$|\varsigma_5| = \left|\frac{f_5\kappa_{11} - f_1\kappa_{51}}{\kappa_{15}\kappa_{51} - \kappa_{11}\kappa_{55}}\right| = \frac{\alpha}{\sqrt{(\beta + \lambda_{11}\lambda_5)^2 + \left(\gamma + \lambda_5(\mu + \mu_{11})\right)^2}} , \tag{5.28}$$

$$\alpha = |f_5(\mu + \mu_{11} - i\lambda_{11}) - f_1(\mu\varrho_m + \mu_{51} - i\lambda_{51})|\,, \tag{5.29}$$

$$\begin{aligned}\beta = (\mu\varrho_m + \mu_{15})^2 - \lambda_{15}^2 - (\mu + \mu_{11})(\eta_{xx} + \eta_{zz} + \mu_{55} - \eta_{xx}^A - \eta_z^V + \mu\varrho_m/v) \\ + \lambda_{11}\lambda_{55}\,,\end{aligned} \tag{5.30}$$

$$\begin{aligned}\gamma = -2\lambda_{51}(\mu\varrho_m + \mu_{15}) + \lambda_{55}(\mu + \mu_{11}) \\ + \lambda_{11}(\eta_{xx} + \eta_{zz} + \mu_{55} - \eta_{xx}^A - \eta_z^V + \mu\varrho_m/v)\,.\end{aligned} \tag{5.31}$$

$\alpha, \beta,$ and γ are real and do not depend on λ_5.

We need to optimize for $\eta_3, \lambda_3, \lambda_5$ for each wave number m_0. Now, η_3 and λ_3 appear in the first term of the power equation only. Their optimum values are easily obtained to be:

$$\eta_3^{opt} = \mu + \mu_{33} - \eta_0^A\,, \tag{5.32}$$

$$\lambda_3^{opt} = \sqrt{(\mu + \mu_{33} - \eta_0^A - \eta_3)^2 + \lambda_{33}^2}\,. \tag{5.33}$$

Similarly, λ_5 appears in the second term only. Setting the gradient of that to zero and manipulating the resulting equation reduces nicely to:

$$\lambda_5^{opt} = \sqrt{\frac{\beta^2 + \gamma^2}{\lambda_{11}^2 + (\mu + \mu_{11})^2}}\,. \tag{5.34}$$

Equations (5.24, 25) can be used to compute the power and power density of the device in question. To maximize the power output, the optimal values of the design parameters (5.32-34) should be used.

5.2 Power Output from a Wave Spectrum

Because of the symmetry of the body, the power output from a regular wave is independent of the incident wave direction of propagation. For that reason, we assume that a non-directional Pierson-Moskowitz (PM) spectrum can describe the real sea state. That is given in [19]:

$$E_\omega(\omega) = \frac{5}{16}\frac{H_s^2}{\omega}\frac{v_p^2}{v^2}\exp\left(-\frac{5}{4}\frac{v_p^2}{v^2}\right). \tag{5.35}$$

Here H_s is the significant wave height of the sea state, $v = \omega^2 h/g$ is the dimensionless frequency squared, and v_p is its value at the peak of the spectrum. The total power produced from this random sea is given by:

$$P_t = \int_0^\infty 2E_\omega(\omega)P\,(\omega)d\omega$$
$$= \frac{5\pi}{32} H_s^2 \rho V_s^3 \int_0^\infty a^3 \left(\frac{v_p^2}{v^{3/2}} \exp\left(-\frac{5}{4}\frac{v_p^2}{v^2}\right)\right)(\lambda_3|\varsigma_3|^2 \quad (5.36)$$
$$+ \lambda_5|\varsigma_5|^2)\,dv\,,$$

where $P(\omega)$ is the power transfer function, i.e. the power in (5.22) for a unit wave amplitude. For the (PM) spectrum, the significant wave height is related to the peak frequency by (see [39]):

$$H_s = \frac{0.1615g}{\omega_p^2}, \quad (5.37)$$

and (5.36) can then be written in dimensionless form as:

$$\frac{P_t}{h^2\rho V_s^3} = 0.0128 \int_0^\infty \frac{a^3}{v^{3/2}}(\lambda_3|\varsigma_3|^2 + \lambda_5|\varsigma_5|^2) \exp\left(-\frac{5}{4}\frac{v_p^2}{v^2}\right) dv\,. \quad (5.38)$$

The power density can be presented in the form:

$$\frac{hP_t}{MV_s^3} = \frac{0.0128}{\pi(1-d)} \int_0^\infty \frac{a}{v^{3/2}}(\lambda_3|\varsigma_3|^2 + \lambda_5|\varsigma_5|^2) \exp\left(-\frac{5}{4}\frac{v_p^2}{v^2}\right) dv\,. \quad (5.39)$$

5.3 Results and Discussion

For the case of regular waves, the power and power density (power per unit mass) were computed in dimensionless form for the case when there is no tension in the spring ($\eta_3 = 0$) because the optimal radii that correspond to the η_3^{opt} values were found too big (and probably uneconomical) to be realistic or representative of real implementations. The case of having a slack mooring is also quite common in real applications and usually costs less to use. The buoy height H does not affect the power from heave but is a significant parameter that determines the mass distribution and therefore affects the pitch power.

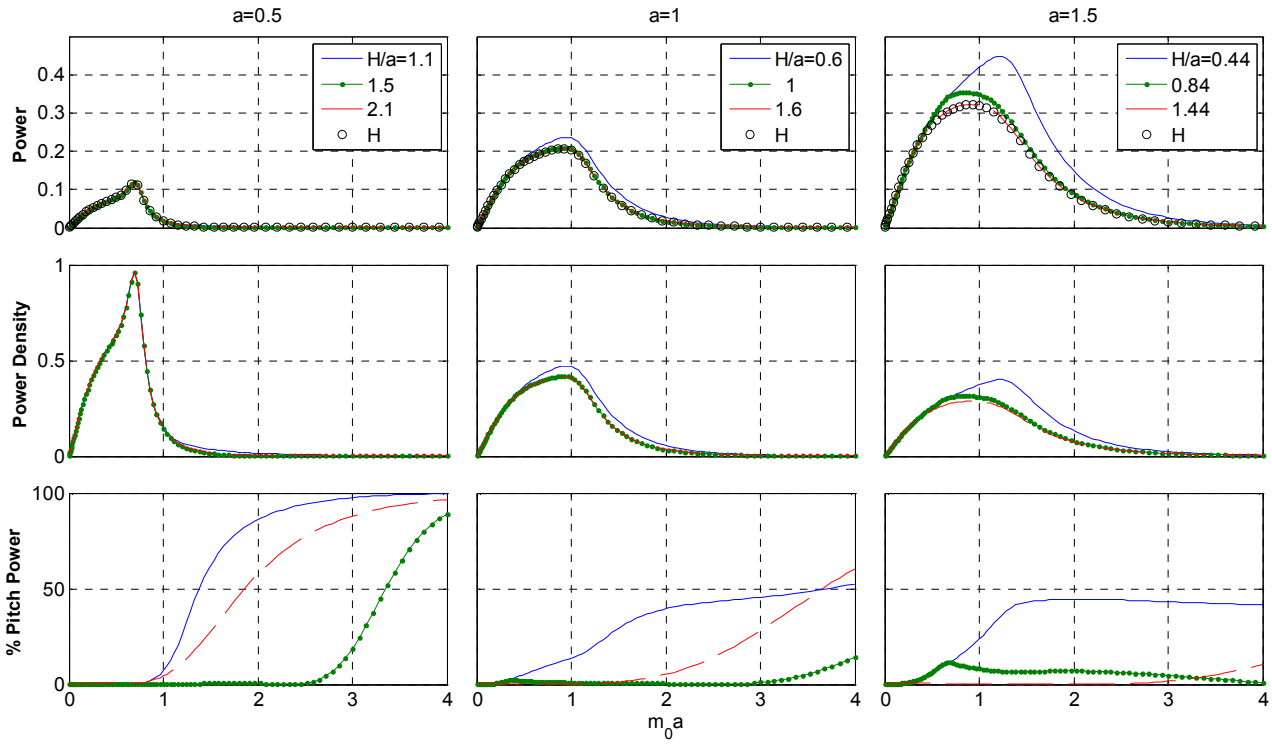

Figure 5-1: Power (row 1), power density (row 2) and % pitch contribution to power (row 3) plots in regular waves for a fixed d=0.5 as a function of wavenumber for three buoy radii a/h and three H/a values (The fourth curve, denoted by H, represents the power output of the heave mode only)

The first row of Figure (5-1) displays the useful power output of the buoy (5.24) against the frequency (represented by $m_0 a$) of the incident monochromatic wave. The different curves in each subfigure represent the chosen buoy height to radius ratios $/a$; i.e. the aspect ratio of the buoy. The power output from the heave mode only is also included for comparison. The three columns represent different radii of the device. The second row shows the power density curves from (5.25) and the third row displays the percentage of the total power that results from including the pitch degree of freedom. For brevity, only the cases for one floatation level ($d = 0.5$) are presented.

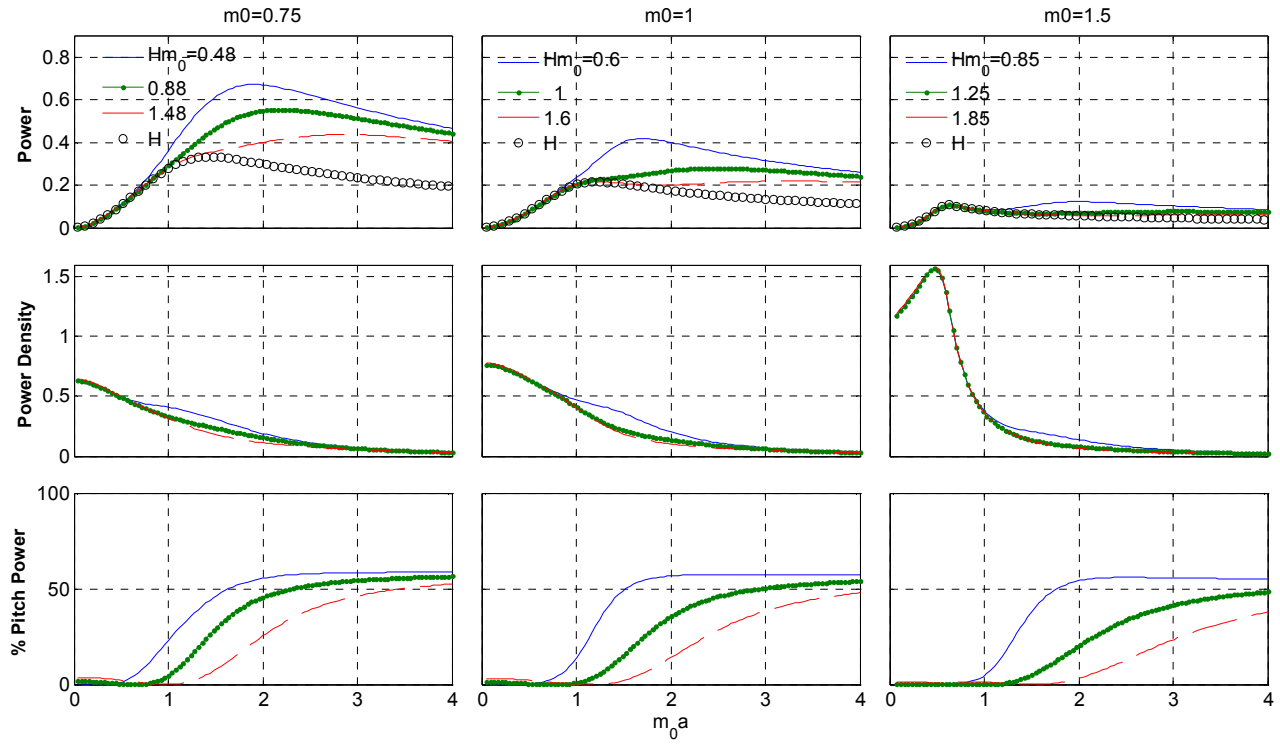

Figure 5-2: Power (row 1), power density (row 2) and % pitch contribution to power (row 3) plots in regular waves for a fixed d=0.5 as a function of a/h for three wavenumbers m_0h and three H/a values (The fourth curve, denoted by H, represents the power output of the heave mode only)

Within the operating range of each buoy, the added power from the pitch mode is not as significant as that from the heave mode in general. However, a significant gain can be achieved with larger radius and flatter buoys (when the radius is fixed). Most notable from the power curves is the presence of an optimal frequency for power absorption, the increase of output with buoy radius, and a widening of the spectrum as the buoy becomes flatter. The change of the shape of the buoy has the effect of shifting the peak power frequency, especially for the larger buoys. The power density curves have the same shape and characteristics as the power curves with the exception that the power density levels decrease with an increasing radius. This is because the increase of power associated with the increase in radius is overshadowed by the increasing mass which changes as a^2. The third row of the figure shows that most of the contribution from the pitch mode appears at the higher frequencies. This is mainly because the power from the heave mode decreases markedly at higher frequencies. This indicates that our multiple DOF arrangement might be more suitable in areas with high frequency waves. In fact, the change in the percentage of pitch power is so abrupt that it might not be economical to employ this system in a low wave frequency area.

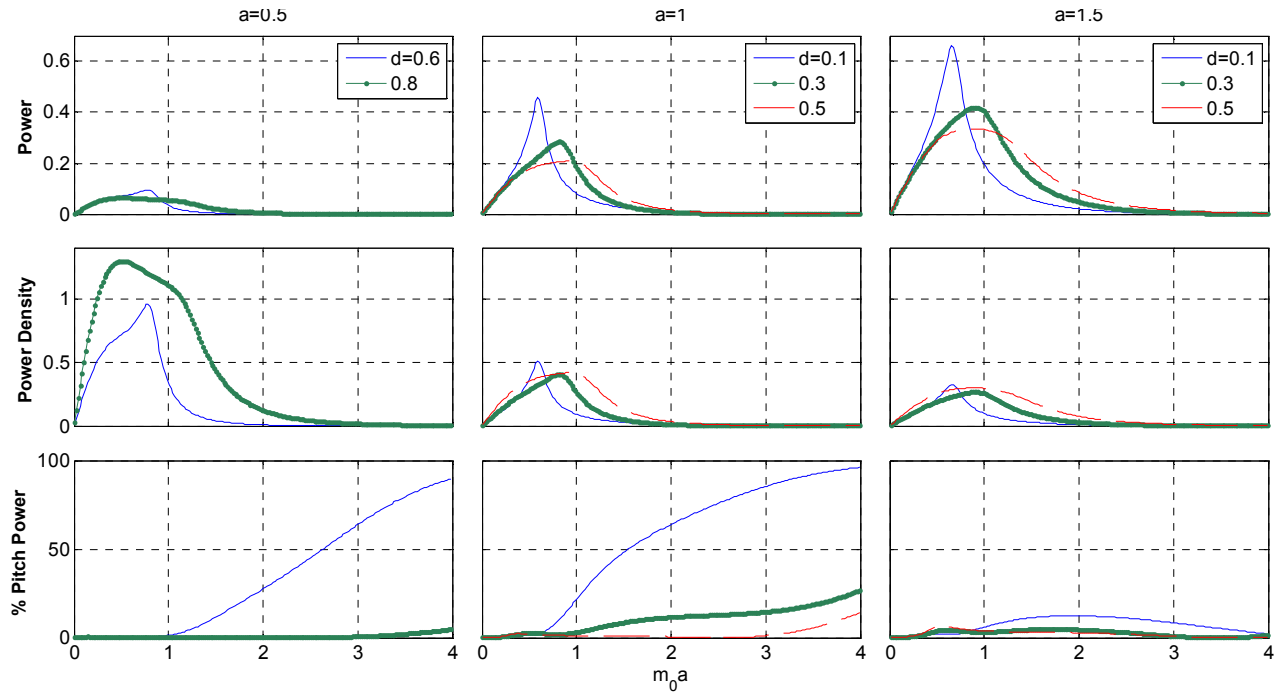

Figure 5-3: Power (row 1), power density (row 2) and % pitch contribution to power (row 3) plots in regular waves for a fixed $H/a = 1$ as a function of wavenumber for three buoy radii a/h and three d/h values

Figure (5-2) displays the same information as in (5-1), varying the radius on the x-axis instead, and for three fixed wave numbers. The power curves confirm our previous statement that the power increases with the increasing buoy radius. However, this is not entirely true at high frequencies. An optimal radius for power extraction exists. The effect of the pitch mode is clearly manifested at larger radii with a significant power increase for the shorter buoys. Worthy to mention is the presence of two peaks for the power curves at high frequencies. The power density is seen to decrease as the buoy radius increases confirming our previous statement.

The last figure (5-3) is meant to show the effect of varying the floatation level d (i.e. the weight) of a buoy of the same size over a wide frequency range. The figure shows that the parameter d is very significant in determining the power output. The deeper the buoy is installed, the lower and more left shifted is the peak power and the wider is the bandwidth. The interesting presence of two power peaks can be seen for smaller and lighter buoys. Here, account is taken of the fact that these buoys must remain floating at all times. In terms of power density, it is clear that the light buoys are dominant in general. The effect of the submergence on the pitch power is very significant especially at higher frequencies.

With regards to irregular waves, the procedure that we followed is:

1. For specified v_p , H/a , and d values, the optimum buoy radius and PTO characteristics that maximize power output are found (assuming no tension in the mooring cable).
2. The power spectrum is computed for those parameters.
3. The integral in Equation (5.38) is evaluated using the trapezoidal rule and this would represent the dimensionless power from irregular waves.

We considered two peak frequencies ($v_p = 0.75, 1$) that are within the useful range of natural wave characteristics. Furthermore, the frequency range is chosen to be wide enough to make the integrand in (5.38) converge.

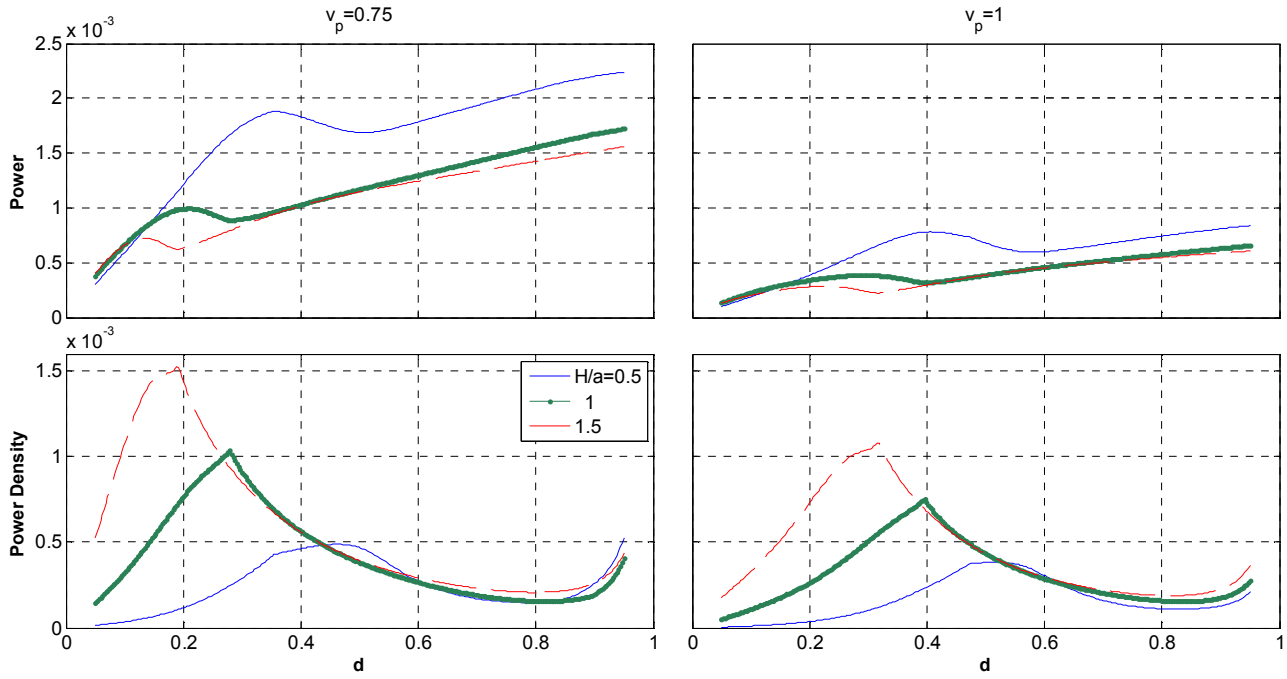

Figure 5-4: Power and power density plots for irregular waves as a function of floatation d for two peak frequencies v_p and three values of H/a

Figure (5-4) is a plot of the power and power density curves for the two peak frequencies considered as a function of the floatation level d. Each subfigure displays the results for three chosen height-to-radius ratios of 0.5, 1 and 1.5. The plots show the superiority of flat and light buoys as compared to the others in terms of power output. The maxima and minima observed in mid-range of d in the figure are mainly due to the changing optimal radius values in these ranges which severely alters the integrand in (5.38). The power density results are more interesting

showing the presence of an optimal floatation level where that density is maximized. This is again mainly due to the small optimal radius at that point.

Figure (5-5) complements Figure (5-4) by showing the corresponding optimal parameters of buoy radius and PTO damping values. The optimal radius is limited in the search to an upper value of 3 which shows in Figure 5-5 at high d values.

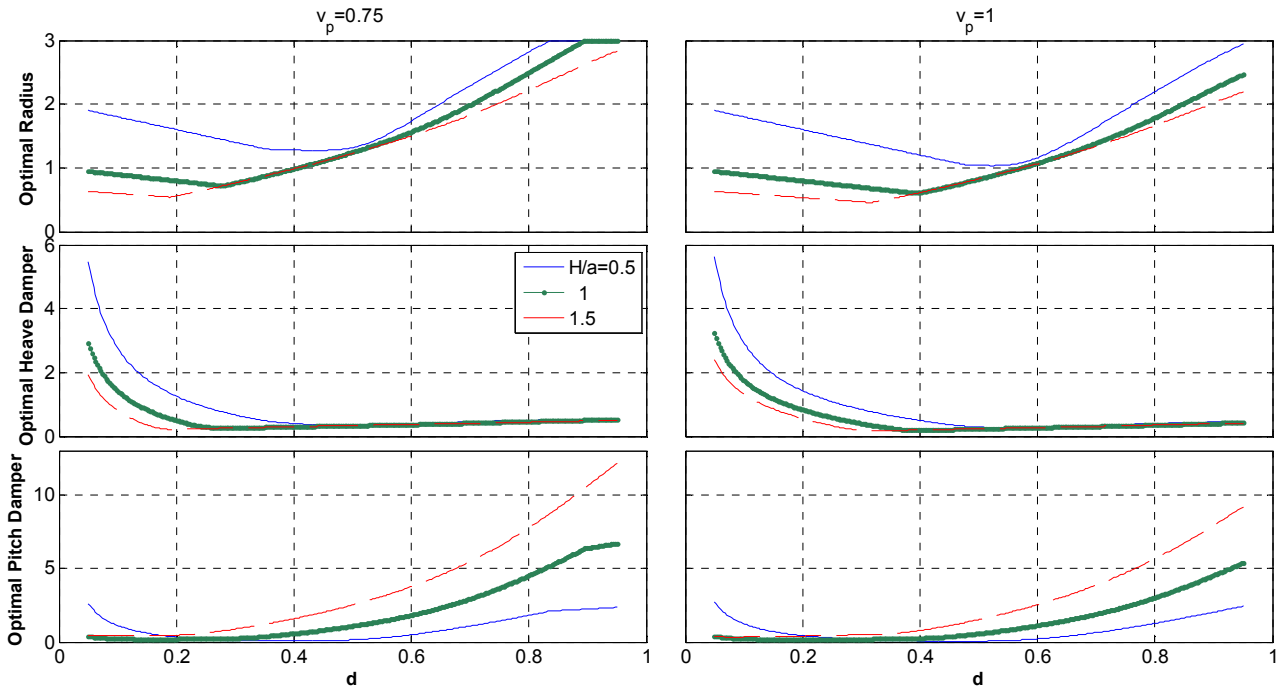

Figure 5-5: Optimal buoy radius (row 1) and PTO heave (row 2) and pitch (row 3) dampers for maximum power extraction from irregular waves as a function of the floatation d for two peak frequencies v_p and three values of H/a

5.4 Conclusion

In this chapter and the previous one, the case of a cylinder oscillating in surge, heave and pitch was considered and analyzed. The hydrodynamic forces on the cylinder were computed and used to determine the power output of the cylinder from two power takeoff mechanisms in regular and irregular waves. The analysis stressed the effect of the pitch mode on the amount of power extracted.

The results in regular waves indicate that the contribution from the pitch mode is highest at high frequencies and high radii. This is mainly because the heave power drops sharply at these specifications. For a given submergence level, shorter buoys were found to produce the most power and an optimal radius for power extraction exists. The effect of increasing the submergence of the buoy (increasing its density) is to shift the now higher peak power to lower frequencies and to limit the bandwidth. This can have major implications in random seas. The results for irregular waves indicate that flatter and lighter bodies perform the best in terms of power production. The power density results indicate a contrary behavior peaking for slender buoys that are more submerged mainly because of the low optimal radii required for these bodies.

Comparing the power results with those of a cylinder restricted to heave, we can tell that employing the added pitch mode can be useful in areas with a concentration of high frequency waves. This is usually associated with a high peak frequency of the spectrum which means that this system is most suitable in areas of generally poor wave resource having low significant wave heights as indicated by the relation (5.37).

Part 3 The Archimedes Wave Swing with an Internal Oscillator

Chapter 6 Dynamics and Power Output of the AWS

The third wave energy converter that will be discussed here is the so called Archimedes Wave Swing (referred to by AWS further on). The AWS is a type of submerged wave and tidal energy converter. In this text, we focus on the wave conversion functionality only. The principle of operation of the AWS is quite simple. The device consists of two main parts. The fixed base is called the silo and the moving part is called the floater [10]. In a real situation, the silo would be moored to sea floor and therefore can move in pitch. For simplicity however, we consider the silo to be fixed to the sea bottom and that the floater can only move in heave. The chamber separating the silo and the floater is usually filled with air.

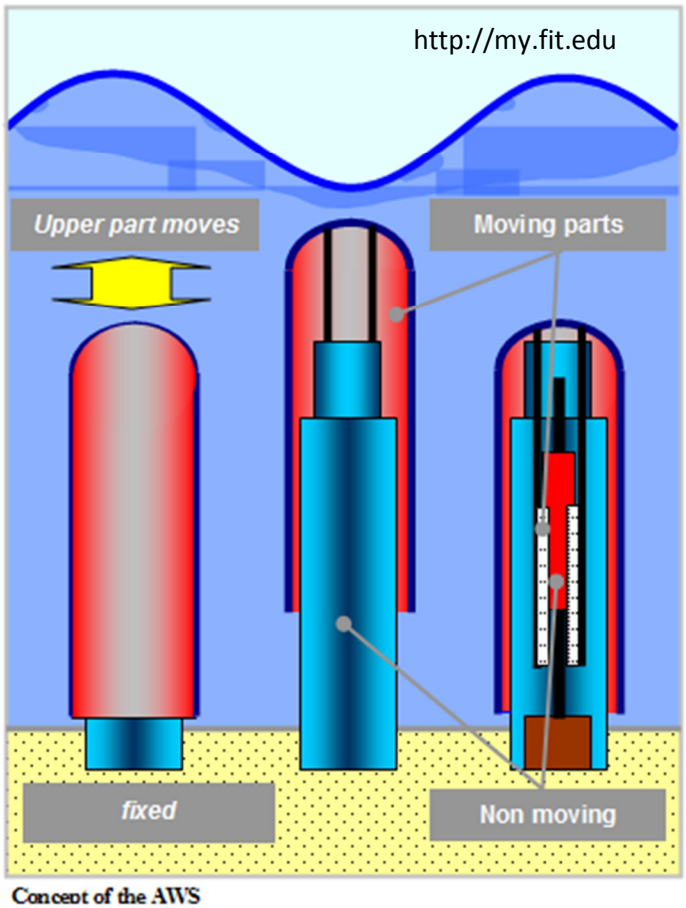

Figure 6-1: Schematic showing the AWS principle of operation showing the internal parts and the different phases of the device under a wave trough and crest

When a wave crest passes above the device, the increasing pressure of the water above pushes the floater downward compressing the air trapped inside. As the wave crest changes to a trough, the decreasing pressure above becomes insufficient to sustain the pressure of the air inside. The gas expands pulling the floater upwards. The cycle then is repeated in a similar manner. This oscillatory motion of the floater is then transmitted to the arm of a linear electric generator to produce electricity. It is interesting to note that the AWS was the first device to employ such a generator.

The AWS is not a new concept and its modeling is not something new. The contribution of this thesis to the device is to assess the effect of an added internal mass spring system inside the air chamber. The rationale behind it follows from earthquake engineering. Buildings in areas where seismic action is common are usually designed to withstand the earthquakes. One such design involves adding a mass spring system inside the building. When the earthquake hits, the vibration is mostly absorbed by the internal system and the building only oscillates with minimum amplitude. Using that idea for the AWS, we can design the device so that the floater becomes almost stationary in the water like the building in our analogy (decreasing the probability of wear and the need for maintenance) and the energy will be transmitted to the internal mass which lies safely away from the salty water.

We want to estimate the power that can be extracted by using such a device. To compute the power, the forces on the device and its reaction to the incoming waves must be known. We make the same assumptions that we did for the floating buoy in order to simplify the problem. Namely, the fluid is considered to be incompressible inviscid, and irrotational. Friction losses are also considered to be negligible. To make the problem linear, only small amplitude oscillations and incident waves are considered. The boundary conditions are therefore simple and to a first order approximation, only mean values of the buoy position and the free surface need to be considered. The linearized Bernoulli equation can thus be applied at the surface to lead to a simple free surface condition.

These assumptions enable us to model the flow as a potential flow, that is, the velocity field at any point can be conveniently represented by the gradient of a scalar potential function ϕ. It follows from the continuity equation that ϕ is governed by the Laplace equation. Cylindrical coordinates will be used because of the geometry of the problem.

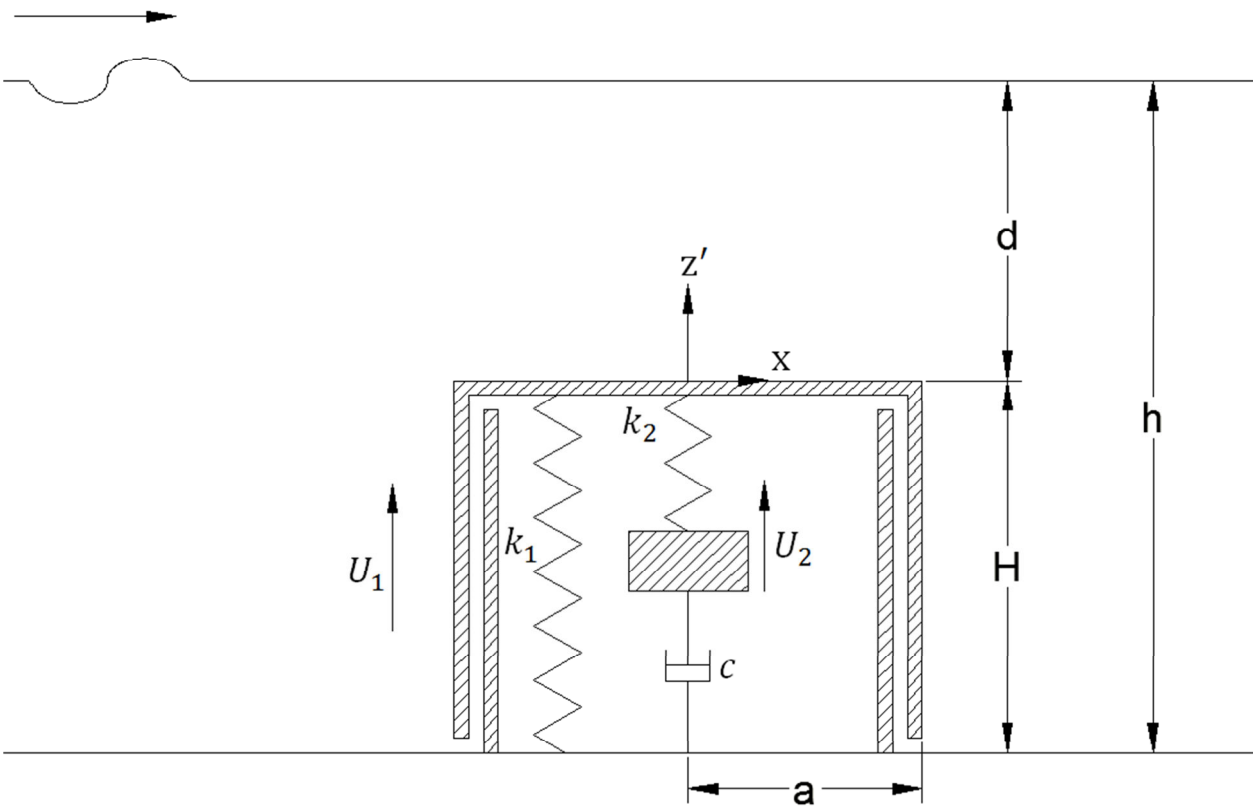

Figure 6-2: Schematic diagram of the AWS with a internal mass-spring system showing the definitions of the different dimensions and parameters used in the text

The radiation and diffraction problems were discussed in detail previously and again we need to solve these problems to attain the power absorbed by our new device. The radiation potential is ϕ_r and the diffraction potential is ϕ_d as defined previously. Both are governed by Laplace's equation. The first is used to get the forces on the AWS resulting from the radiated waves while the second is used to get the forces resulting from the incoming wave. In a real situation, the incident wave is scattered by the presence of the buoy and waves are also radiated because of its oscillatory motion. The resulting potential will therefore include the combined effects of both radiation and diffraction. However, since the problem is linear, the total potential is just the summation of the individual potentials as in (5.1). This fact makes the problem easier to handle as each potential can be solved for separately. We further assume that the velocity potential ϕ can be represented by $\phi = Re\{\hat{\phi}(r,z,\theta)e^{-i\omega t}\}$, and we non-dimensionalize as in the previous chapters. For length parameters, here, r, z and a have the same definitions as for the floating

buoy case. In this case, H is the draft of the cylinder and $d = h - H$ is the length of the fluid region above the cylinder.

Again, for both the radiation and scattering problems, the potential amplitude function can be separated into two regions, the first for $r > a$ (the exterior region) and the other one above the cylinder for $r < a$ (the interior region). The two resulting potentials are denoted by $\hat{\phi}_e$ and $\hat{\phi}_i$ respectively. Separation of variables is used to solve for these two functions in the same manner as was done for the floating buoy.

The incident wave is assumed to be unidirectional propagating in the positive x direction and the free surface displacement is given in (5.2). The Laplace equation applies with the last term dropped for the axi-symmetric radiation problem. The boundary conditions needed again include the linearized free surface condition, the no flux conditions on the bottom of the ocean and on the side of the body and the inhomogeneous condition in the normal direction at the top of the body. Finally, the potential must satisfy the radiation condition at infinity:

In what follows, we attempt to solve for the radiation coefficients (§ 6.1) and then for the excitation force (§ 6.2) and finally we group the results to compute the power produced by the buoy (§ 6.3).

6.1 The Radiation Problem

The radiation problem has already been treated in detail for the floating buoy. The aim of solving this problem is to obtain the forces that act on the body as energy, in the form of waves, radiates away. The result is the complex amplitude of the force which is best viewed as the summation of a damping coefficient (the real part) and an added mass (the imaginary part). The same idea follows for the AWS which is modeled as a submerged circular cylinder. The analysis follows in the same manner as before and the assumptions are basically the same.

6.1.1 Theory

As for previous analysis, it is convenient to write the potential as the sum of a homogeneous potential $\hat{\phi}_h$ and a particular one $\hat{\phi}_p$. Both of these functions satisfy the axi-symmetric Laplace equation and the relevant boundary conditions. Note that the free surface condition must be satisfied by the internal potential function as well as the external one in this case. For these potentials and for the time being, let's use a new coordinate system (denoted by a prime) whose origin is on the center of the upper surface of the cylinder and is related to the global system by:

$$\begin{cases} z' = z - H\,, \\ r' = r\,. \end{cases} \tag{6.1}$$

This will facilitate the analysis later on. In the new system, Laplace's equation is invariant:

$$\frac{\partial^2 \hat{\phi}}{\partial r^2} + \frac{1}{r}\frac{\partial \hat{\phi}}{\partial r} + \frac{\partial^2 \hat{\phi}}{\partial z'^2} = 0\,, \tag{6.2}$$

and the boundary conditions become (remember (2.12)):

$$\left.\frac{\partial \hat{\phi}_p}{\partial z'}\right|_{z'=0} = \hat{u}\,, \tag{6.3}$$

$$\left.\left(\frac{\partial \hat{\phi}_p}{\partial z'} - \frac{\omega^2 h}{g}\hat{\phi}_p\right)\right|_{z'=d} = 0\,, \tag{6.4}$$

for the particular solution and:

$$\left.\frac{\partial \hat{\phi}_h}{\partial z'}\right|_{z'=0} = 0\,, \tag{6.5}$$

$$\left.\left(\frac{\partial \hat{\phi}_h}{\partial z'} - \frac{\omega^2 h}{g}\hat{\phi}_h\right)\right|_{z'=d} = 0\,, \tag{6.6}$$

$$\hat{\phi}_h\big|_{r=a} = \left(\hat{\phi}_e - \hat{\phi}_p\right)\big|_{r=a}\,, \tag{6.7}$$

for the homogeneous solution. By inserting a function of the form $\hat{\phi}_p = Az' + B$ into the governing equation and applying (6.3-4), a particular solution is given by:

$$\hat{\phi}_p = \hat{u}\left(z' + \frac{1}{v} - d\right), \tag{6.8}$$

$$v = \frac{\omega^2 h}{g}\,. \tag{6.9}$$

Now the homogeneous solution can be solved using the method of separation of the variables. It can be written in the form:

$$\hat{\phi}_h = \sum_{n=0}^{\infty} \alpha_n \frac{\psi_n(r)}{\psi_n(a)} \xi_n(z'), \tag{6.10}$$

where the components are given by:

$$\xi_n(z') = \begin{cases} \dfrac{\cosh(\lambda_0 z')}{\sqrt{M_0}} & M_0 = \dfrac{d}{2} + \dfrac{\sinh(2\lambda_0 d)}{4\lambda_0} \quad (n = 0)\,, \\ \dfrac{\cos(\lambda_n z')}{\sqrt{M_n}} & M_n = \dfrac{d}{2} + \dfrac{\sin(2\lambda_n d)}{4\lambda_n} \quad (n > 0)\,, \end{cases} \tag{6.11}$$

such that λ_0 and $i\lambda_n$ are solutions of the dispersion relation:

$$\lambda \tanh(\lambda d) = v\,, \tag{6.12}$$

and $\psi_n(r)$ are defined as:

$$\psi_n(r) = \begin{cases} J_0(\lambda_0 r)\,, \\ I_0(\lambda_n r)\,. \end{cases} \tag{6.13}$$

In this equation, J_0 and I_0 are zeroth order Bessel and Modified Bessel functions of the first kind. Finally, α_n are constants. Matching the potentials at the common boundary to both regions:

$$\hat{\phi}_h\big|_{r=a} = \sum_{n=0}^{\infty} \alpha_n \xi_n(z') \;=\; \left(\hat{\phi}_e - \hat{\phi}_p\right)\big|_{r=a}\,. \tag{6.14}$$

which leads to:

$$\alpha_n = \int_H^1 \hat{\phi}_e\big|_{r=a}\, \xi_n(z-H)dz - {\alpha_n}^*\,, \tag{6.15}$$

$${\alpha_n}^* = \int_H^1 \hat{\phi}_p\big|_{r=a}\, \xi_n(z-H)dz\,. \tag{6.16}$$

The external potential can be written in the form:

$$\hat{\phi}_e = \sum_{k=0}^{\infty} A_k \frac{R_k(r)}{R_k'(a)} Z_k(z)\,, \tag{6.17}$$

where $R_k(r)$ are defined in (2.45), $Z_k(z)$ in (2.43) and the eigenvalues m_0 and im_k needed in these functions are solutions of (2.41). The last equation represents the sum of a propagating wave (the first term $k = 0$) and an infinite number of evanescent waves ($k \geq 1$) that die out at an infinite distance. Matching potential gradients (normal velocities) at the common boundary and using the no flux condition at the body side:

$$\left.\frac{\partial \hat{\phi}_e}{\partial r}\right|_{r=a} = \sum_{k=0}^{\infty} A_k Z_k(z) = \begin{cases} 0 & (0 \leq z \leq H)\,, \\ \dfrac{\partial \hat{\phi}_i(a,z)}{\partial r} & (H \leq z \leq 1)\,. \end{cases} \tag{6.18}$$

This yields:

$$A_k = \int_H^1 \left.\frac{\partial \hat{\phi}_h}{\partial r}\right|_{r=a} Z_k(z)dz + A_k^*\,, \tag{6.19}$$

$$A_k^* = \int_H^1 \left.\frac{\partial \hat{\phi}_p}{\partial r}\right|_{r=a} Z_k(z)dz = 0\,, \tag{6.20}$$

since the particular solution is independent of the radial coordinate. Inserting (6.10) into (6.19):

$$A_k = \sum_{n=0}^{\infty} \alpha_n \frac{\psi_n'|_{r=a}}{\psi_n(a)} C_{nk}\,, \tag{6.21}$$

where the coupling coefficient C_{nk} is defined as:

$$C_{nk} = \int_H^1 \xi_n(z-H) Z_k(z)dz\,. \tag{6.22}$$

Inserting (6.17) into (6.15):

$$\alpha_n = \sum_{k=0}^{\infty} A_k \frac{R_k(a)}{R_k'(a)}\, C_{nk} - {\alpha_n}^*\,. \tag{6.23}$$

Finally, (6.21) is inserted into (6.23) to yield,

$$\alpha_n = \sum_{j=0}^{\infty} e_{nj}\alpha_j\, - {\alpha_n}^*\,, \tag{6.24}$$

$$e_{nj} = \sum_{k=0}^{\infty} \frac{\psi_j'\big|_{r=a}}{\psi_j(a)} \frac{R_k(a)}{R_k'(a)} C_{jk} C_{nk} \,, \tag{6.25}$$

This system can be truncated at any number of terms depending on the accuracy of the solutions required.

6.1.2 Radiation Coefficients

Now the case under question involves only the heaving action and the radiation coefficients can be obtained in a manner similar to that of (§ 2.2.2). For unit velocity:

$$\frac{M_{33} + iB_{33}/\omega}{\rho h^3} = -\iint \hat{\phi} \frac{\partial \hat{\phi}}{\partial n} dS \,. \tag{6.26}$$

Here the integration is over S the surface area of the cylinder. Considering the external and internal regions separately and making use of the body boundary conditions, the integral becomes:

$$\frac{M_{33} + iB_{33}/\omega}{\pi \rho h^3} = -2\int_0^a r\hat{\phi}_h(r,d)dr - 2\int_0^a r\hat{\phi}_p(r,d)dr \,. \tag{6.27}$$

Using (6.8) and (6.10) results in (returning to the over bar notation)

$$\lambda_{33} + i\mu_{33} = \frac{M_{33} + iB_{33}/\omega}{\pi \rho a^3} = -\frac{2}{\bar{a}^3} \sum_{n=0}^{\infty} \alpha_n \frac{\psi_n^*}{\sqrt{M_n}} - \frac{1}{\bar{a}}\left(\frac{1}{v} - \bar{d}\right), \tag{6.28}$$

$$\psi_n^* = \int_0^{\bar{a}} \bar{r} \frac{\psi_n(\bar{r})}{\psi_n(\bar{a})} d\bar{r} \,. \tag{6.29}$$

6.1.3 Results and Discussion

These are the results for the damping coefficient and added mass for some chosen cases.

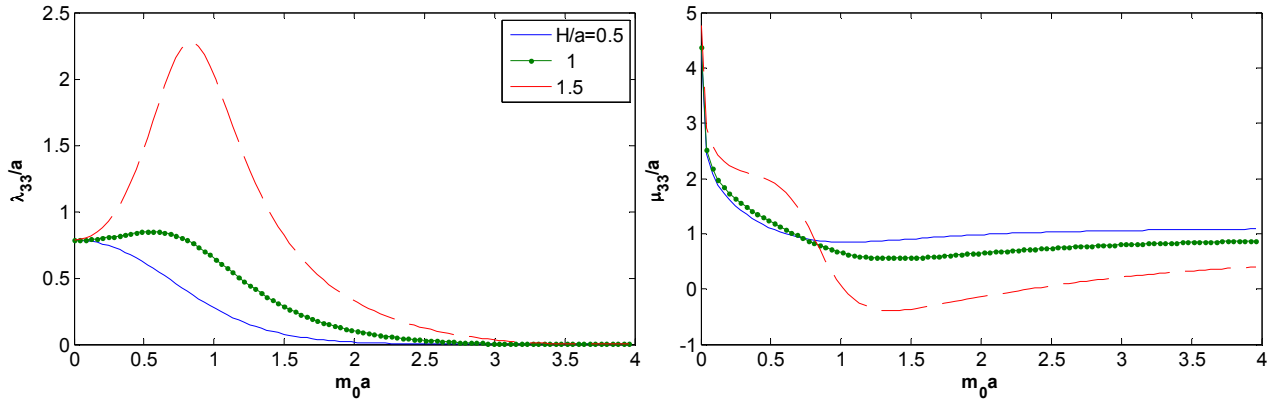

Figure 6-3: Radiation damping (left) and added mass (right) coefficients for the AWS as a function of wavenumber for $a = 0.5$ and three H/a values

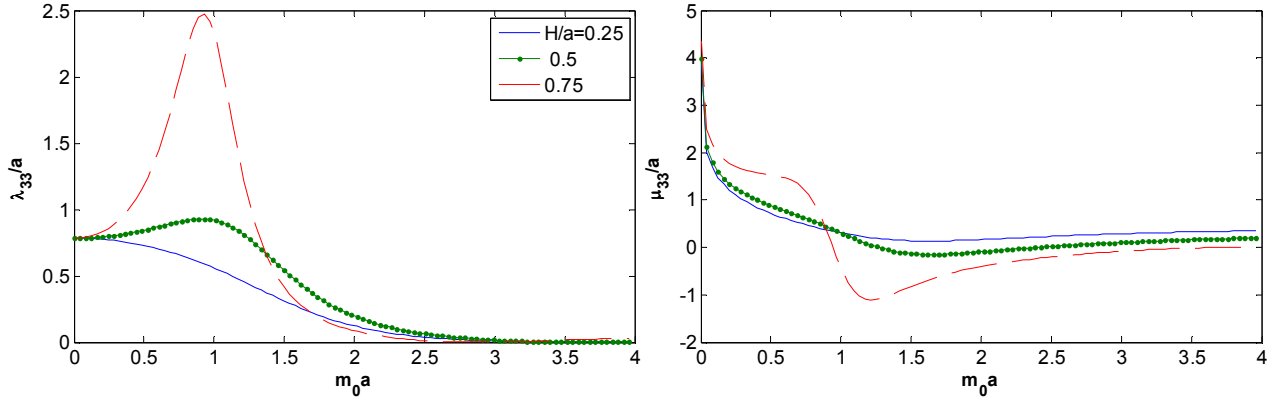

Figure 6-4: Radiation damping (left) and added mass (right) coefficients for the AWS as a function of wavenumber for $a = 1$ and three H/a values

The results show a similar behavior to those of the floating buoy. Higher forces are observed for slender buoys. Particularly interesting besides the minimum of the added mass, which we already encountered in the floating buoy case, is the presence of a local maximum or an inflection point. This is quite clear for slender bodies at which the added mass can also be slightly negative for a certain frequency range but this is typical of submerged bodies close to the surface [42].

6.2 The Diffraction Problem

One more time, the diffraction problem for the submerged body must be solved to obtain the power output. Will we obtain similar results to the buoy case as well? There must be some difference caused by submergence. The procedure is the same.

6.2.1 Theory

Using the same auxiliary coordinate system introduced in the previous section and nondimensionalizing in the same manner, the same conditions used for the radiation problem are still applicable with the body velocity set to zero and with the addition of conditions that maintain symmetry such as those in (5.62, 63, 65 and 66). The incident wave is still given by (5.2). The Laplace equation still applies in the form:

$$\frac{\partial^2\hat{\phi}}{\partial r^2}+\frac{1}{r}\frac{\partial\hat{\phi}}{\partial r}+\frac{\partial^2\hat{\phi}}{\partial z'^2}+\frac{1}{r^2}\frac{\partial^2\hat{\phi}}{\partial\theta^2}=0\,. \tag{6.30}$$

The internal potential is found to be of the form:

$$\hat{\phi}_i=\zeta_0\sum_{p=0}^{\infty}\sum_{n=0}^{\infty}\alpha_{pn}\frac{\epsilon_p}{2\pi}\frac{\psi_{pn}(r)}{\psi_{pn}(a)}\xi_n(z')\cos(p\theta)\,, \tag{6.31}$$

where $\xi_n(z')$ was defined in (6.11) and the radial modal function is defined as:

$$\psi_{pn}=\begin{cases}J_p(\lambda_0 r),\\ I_p(\lambda_n r),\end{cases} \tag{6.32}$$

where λ_n are the eigenvalues satisfying (6.12). Applying the potential matching condition (6.7) yields:

$$\alpha_{pn}=\frac{1}{\zeta_0}\int_0^d\int_0^{2\pi}\hat{\phi}_e\big|_{r=a}\,\xi_n(z')\cos(p\theta)\,d\theta dz'. \tag{6.33}$$

The external potential is the sum of the potentials of the incident wave and the scattered wave. It is given in the form:

$$\hat{\phi}_e = -\zeta_0 \sum_{k=0}^{\infty} \epsilon_k i^{k+1} \Bigg(J_k(m_0 r) - H_k(m_0 r) \frac{J_k'(m_0 a)}{H_k'(m_0 a)} \Bigg) \frac{Z_0(z)}{Z_0'(1)} \cos(k\theta) + \zeta_0 \sum_{j=0}^{\infty} \sum_{k=0}^{\infty} A_{kj} \frac{\epsilon_k}{2\pi} \frac{R_{kj}(r)}{R_{kj}'(a)} Z_j(z) \cos(k\theta), \tag{6.34}$$

where the depth dependent modal functions were given in (2.43) and the radial ones are defined in (2.80). Matching the normal velocities at the interface of both regions then:

$$A_{kj} = \frac{1}{\zeta_0} \int_0^{2\pi} \int_H^1 \left. \frac{\partial \hat{\phi}_i}{\partial r} \right|_{r=a} Z_j(z) \cos(k\theta)\, dz d\theta\,. \tag{6.35}$$

Now inserting the value of the internal potential function,

$$A_{kj} = \sum_{n=0}^{\infty} \frac{\psi_{kn}'(a)}{\psi_{kn}(a)} C_{nj} \alpha_{kn}\,, \tag{6.36}$$

where the coupling coefficient C_{nj} was defined in (6.22). Inserting the value of the external potential into (6.33) and simplifying yields:

$$\alpha_{pn} = \sum_{j=0}^{\infty} A_{pj} \frac{R_{pj}(a)}{R_{pj}'(a)} C_{nj} + \alpha_{pn}^*\,, \tag{6.37}$$

$$\alpha_{pn}^* = -\int_0^d \int_0^{2\pi} \sum_{k=0}^{\infty} \epsilon_k i^{k+1} \Bigg(J_k(m_0 a) - H_k(m_0 a) \frac{J_k'(m_0 a)}{H_k'(m_0 a)} \Bigg) \frac{Z_0(z)}{Z_0'(1)} \cos(k\theta)\, \xi_n(z') \cos(p\theta)\, d\theta dz'. \tag{6.38}$$

Finally inserting (6.36) into (6.37),

$$\alpha_{pn} = \sum_{l=0}^{\infty} e_{pnl} \alpha_{pl} + \alpha_{pn}^*\,, \tag{6.39}$$

$$e_{pnl} = \sum_{j=0}^{\infty} \frac{R_{pj}(a)}{R_{pj}'(a)} \frac{\psi_{pl}'(a)}{\psi_{pl}(a)} C_{lj} C_{nj}\,. \tag{6.40}$$

These are systems of equations in the unknowns α_{pn} that need to be solved.

6.2.2 Forces on the Cylinder

The force in the vertical direction on the buoy is given by the real part of $\hat{F}^D e^{-i\omega t}$ and

$$\frac{\hat{F}^D}{\rho h^4 \omega^2} = -i \int_0^{2\pi} \int_0^a r \hat{\phi}_i(r, d, \theta) dr\, d\theta = -i\zeta_0 \sum_{n=0}^{\infty} \alpha_{0n} \frac{\psi_n^*}{\sqrt{M_n}}, \tag{6.41}$$

where ψ_n^* was defined in (6.29). Although the buoyant force is independent of wave amplitude for a submerged device, the form presented in Section (2.3) is still used and the force is written as:

$$\frac{\left|\hat{F}^D\right|}{B} = \frac{v}{\pi a^2} \left| \sum_{n=0}^{\infty} \alpha_{0n} \frac{\psi_n^*}{\sqrt{M_n}} \right|. \tag{6.42}$$

Since only α_{0n} are required to get the vertical force, then the system to solve reduces to:

$$\alpha_{0n} = \sum_{l=0}^{\infty} e_{0nl} \alpha_{0l} + \alpha_{0n}^*, \tag{6.43}$$

$$e_{0nl} = \sum_{j=0}^{\infty} \frac{R_{0j}(a)}{R'_{0j}(a)} \frac{\psi'_{0l}(a)}{\psi_{0l}(a)} C_{lj} C_{nj}. \tag{6.44}$$

6.2.3 Results and Discussion

These are the results for the vertical force amplitude and phase (divided by π) for some chosen cases.

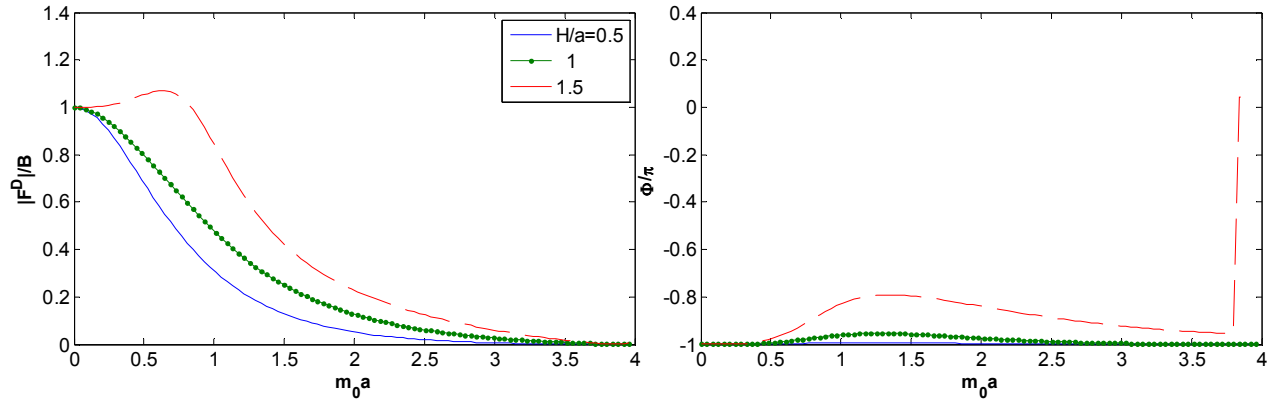

Figure 6-5: Diffraction force amplitude (left) and phase divided by π (right) for the AWS as a function of wavenumber for $a = 0.5$ and three H/a values

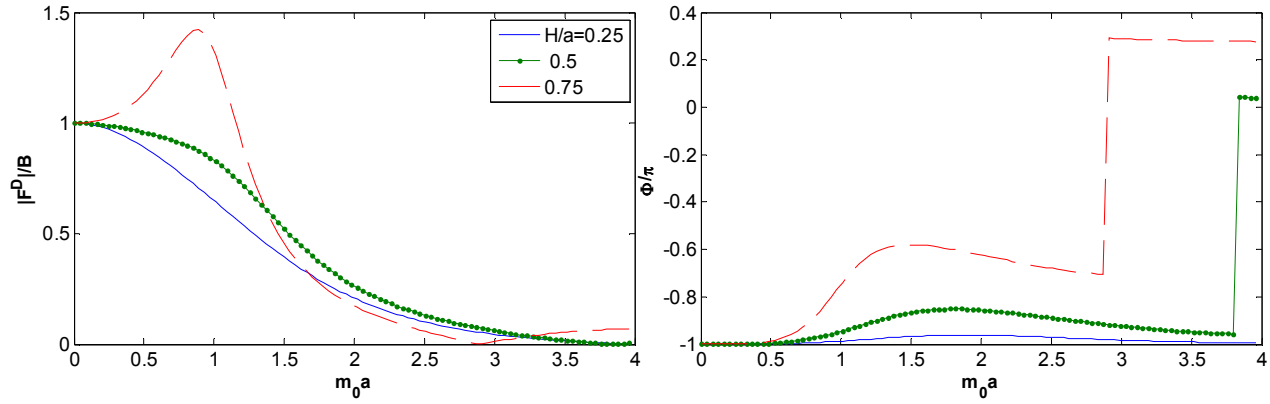

Figure 6-6: Diffraction force amplitude (left) and phase divided by π (right) for the AWS as a function of wavenumber for $a = 1$ and three H/a values

The results in this case again are similar to those for the floating buoy with the exception of nodes appearing at certain frequencies where the force reverses its sign. This explains the sudden jump in the phase by π at the corresponding wavenumbers. These results were found to match those in [22] with the difference that the phase is the negative of the one presented in that paper. The reason for that is still unclear but the results here are reproduced by the Haskind relation in the next section and identical results to these were obtained. Nonetheless, the phase sign will be irrelevant as we will see in the upcoming sections as the power merely depends on the force amplitude. An interesting observation is the high force amplitudes that slender bodies can achieve at certain frequencies (forming an amplitude peak that goes above one buoyancy term B) as compared to the floating body where such a behavior was not observed.

Off course the Haskind relation can still be used and a form such as that given in (2.98) can be used. Alternatively, a derivation similar to that in section 4.3.4 can be done as well to obtain information about the phase as well.

6.3 Power Output from a Single Wave

The aim of this section is to study how effective it is to employ the internal oscillator we talked about. To do that, the first subsection (6.3.1) studies the AWS without an internal oscillator and presents the power output from that system which is then used as a control system for comparison with the oscillator complemented system in subsection (6.3.2).

6.3.1 The AWS with no Internal Oscillator

When the internal oscillator is absent and at steady state, the power output of the device (assuming a linear dashpot as a model for the PTO) is given by:

$$P = \frac{1}{2}\frac{c\left|\hat{F}_e\right|^2}{(c+B_{33})^2+(\omega M+\omega M_{33}-k_1/\omega)^2}, \tag{6.45}$$

where $k_1$is a springiness constant used to approximate the effect of the internal gas and the rest of the variables are defined as before. The same dimensionless definitions will be retained with the additional $k_1 = \omega^2\rho\pi a^3\eta_1$ to represent the spring constant. The relevant outputs then become:

$$\frac{P}{\frac{\pi}{2}\rho V_s^3\zeta_0^2} = \bar{a}^3\nu^{3/2}\frac{\lambda_c|f|^2}{(\lambda_c+\lambda_{33})^2+(\mu+\mu_{33}-\eta_1)^2}, \tag{6.46}$$

$$\frac{P}{MV_s^3\zeta_0^2/(2h^3)} = \frac{\nu^{3/2}}{\mu}\frac{\lambda_c|f\ |^2}{(\lambda_c+\lambda_{33})^2+(\mu+\mu_{33}-\eta_1)^2}, \tag{6.47}$$

$$|\varsigma_1| = \frac{|\widehat{U}_1|}{\zeta_0} = \frac{|f|}{\sqrt{(\lambda_c + \lambda_{33})^2 + (\mu + \mu_{33} - \eta_1)^2}}, \tag{6.48}$$

where f is the dimensionless excitation force (defined just after (5.17)).

The optimal value of the PTO damper that maximizes (6.46) is easily found to be:

$$\lambda_c^{opt} = \sqrt{\lambda_{33}^2 + (\mu + \mu_{33} - \eta_1)^2} \tag{6.49}$$

The gas springiness can be adjusted as well by changing the equilibrium gas pressure. Ideally, this results in an optimal value:

$$\eta_1^{opt} = \mu + \mu_{33}\,. \tag{6.50}$$

This expression may be difficult to achieve in practice because of physical limitations. Furthermore, the design may involve no gas or a gas-spring combination to act as a restoring force. If the optimal spring value is too low, it may be impossible to implement such a spring because the initial compression under the action of the floater weight may cause the spring to collapse. It is therefore desirable to find the minimum spring value that is possible. At equilibrium and in the absence of any waves, a force balance on the floater includes the weight, buoyancy and gas spring forces:

$$-Mg + \pi a^2 \rho g H - k_1 \Delta_1 = 0\,, \tag{6.51}$$

where Δ_1 is the initial displacement of the floater taken to be positive when the spring is expanded. If we let χ be the specific gravity of the body (at least on average), the expression (6.51) can be equivalently written as:

$$\eta_1 \delta_1 = \frac{1}{v\bar{a}}(1 - \chi), \tag{6.52}$$

where $\delta_1 = \Delta_1/H$. This shows that the spring is expanded initially if the body is less dense than the water. It follows from the definition of χ that $= \chi H/a$. We would like to limit this initial displacement to a maximum fraction l_1 of the body height so that:

$$\left|\frac{\Delta_1}{H}\right| \leq l_1 \tag{6.53}$$

The acceptable value of the spring constant is then bounded by the relation:

$$\eta_1 \geq \frac{1}{v\bar{a}} \frac{|1-\chi|}{l_1}. \tag{6.54}$$

If the optimal spring value (6.50) fails to meet this criterion, then it must be rejected and the problem becomes a constraint optimization problem. Generally speaking, the optimal value of η_1 is whatever makes $(\mu + \mu_{33} - \eta_1)^2$ a minimum so that if the value given by (6.50) fails, the optimal value would result by satisfying an equality constraint in (6.54) instead. The result of this analysis is shown in Figure (6-7) for a chosen constraint of $l_1 = 0.1$ or an initial displacement of 10% of the body height. Also shown in the figure is the theoretical maximum power that can be achieved for this heaving body and is given by:

$$\frac{P_{max}}{\frac{\pi}{2}\rho V_s^3 \zeta_0^2} = \frac{1}{2\pi}\left(\frac{m_0^2 - v m_0 + v}{\sqrt{v} m_0^2}\right). \tag{6.55}$$

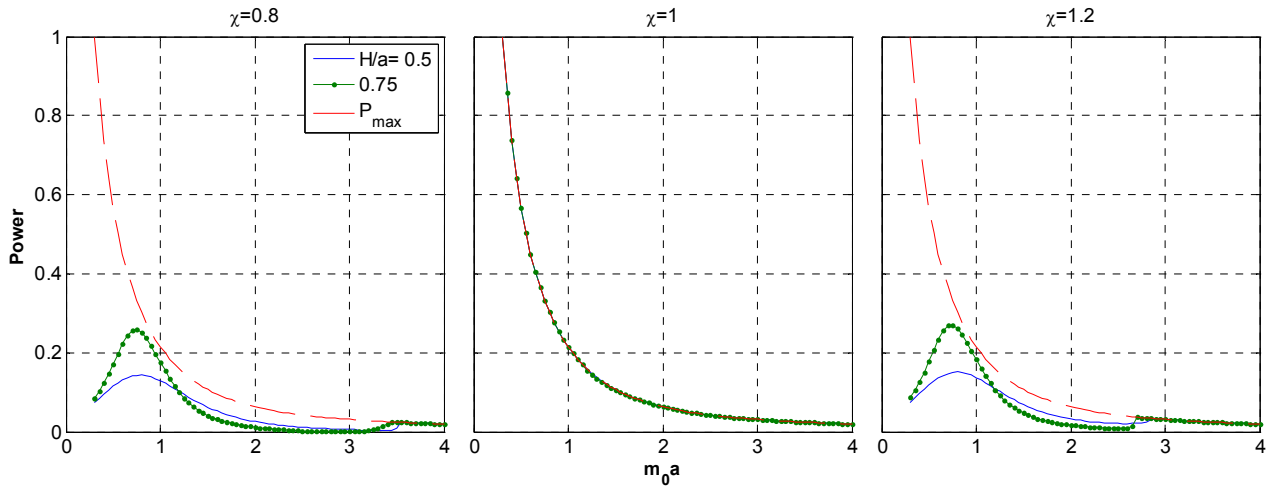

Figure 6-7: Plots of the power output of the AWS without an internal oscillator at $a = 1$ and $l_1 = 0.1$ as a function of wavenumber and for two values of H/a with the theoretical maximum power output also shown

The effect of the conditions is clearly marked as the power deviates from its theoretical maximum (particularly at low frequencies). Although for the case when $\chi = 1$, the right side of (6.54) becomes null, this condition may still be violated if the optimal springiness is negative which is the case when the added mass is sufficiently negative in magnitude. This causes the slightly suboptimal performance for the body with $H/a = 0.75$ to appear in the second plot of Figure (6-7). What follows is the case of the same body but with an internal oscillator. This figure will be used to compare with the results of the new case to be discussed.

6.3.2 The AWS with an Internal Oscillator

Now let's consider the case when a second mass is free to move in the system. An internal mass spring system is supplemented to the system in an effort to make the general performance better. The idea is that an added degree of freedom should provide more flexibility in the system design. It is possible to fix the internal system to oscillate at an angle to the vertical axis. This provides more space for the oscillation allowing softer springs to be used. However, it has the disadvantage of transmitting only part of the force from the wave to internal mass (sort of a cosine loss) where the power will be extracted. Furthermore, this system is difficult to implement and shall not be pursued any further. The mass will thus be constrained to vertical oscillation. This problem involves the use of two springs: one that models the gas and the other links the mass of the floater to the internal oscillator. With two degrees of freedom present, the dynamic balance of forces on the system now reads:

$$\begin{cases} \left(k_1 + k_2 - \omega^2\left(M_f + M_{33}\right) - i\omega B_{33}\right)\widehat{U}_1 - k_2\widehat{U}_2 = \widehat{F}^D, \\ -k_2\widehat{U}_1 + (k_2 - \omega^2 M_i - i\omega c)\widehat{U}_2 = 0\,. \end{cases} \tag{6.56}$$

Here, M_f and M_i are the masses of the floater and internal oscillator while $\widehat{U}_1$ and $\widehat{U}_2$ are their displacements respectively. k_2 is the constant of the spring holding the oscillator in place. Notice that the PTO is hooked to the internal mass. If we use the mass distribution ratio:

$$\chi_M = \frac{M_i}{M} = \frac{M_i}{M_f + M_i}, \tag{6.57}$$

then (6.56) can be written in dimensionless form:

$$\begin{cases} (\alpha - i\lambda_{33})\varsigma_1 - \eta_2\varsigma_2 = f\,, \\ -\eta_2\varsigma_1 + (\eta_2 - \chi_M\mu - i\lambda_c)\varsigma_2 = 0\,, \end{cases} \tag{6.58}$$

where we define:

$$\alpha = \eta_1 + \eta_2 - (1 - \chi_M)\mu - \mu_{33}. \tag{6.59}$$

This system of equations can be easily solved with the result:

$$\begin{cases} \varsigma_1 = \dfrac{(\eta_2 - \chi_M\mu - i\lambda_c)}{(\eta_2 - \chi_M\mu - i\lambda_c)(\alpha - i\lambda_{33}) - \eta_2^2}\, f, \\ \varsigma_2 = \dfrac{\eta_2}{(\eta_2 - \chi_M\mu - i\lambda_c)(\alpha - i\lambda_{33}) - \eta_2^2} f\,. \end{cases} \tag{6.60}$$

Now the system at hand has many undetermined coefficients and we would like to set some constraints over these parameters. The point of adding the internal oscillator was to limit the motion of the floater ς_1. It is therefore required to find the value of η_2 that maximizes:

$$\left|\frac{\varsigma_2}{\varsigma_1}\right| = \frac{\eta_2}{\sqrt{(\eta_2 - \chi_M\mu)^2 + \lambda_c^2}}. \tag{6.61}$$

This is found to be:

$$\eta_2 = \frac{(\chi_M\mu)^2 + \lambda_c^2}{\chi_M\mu}. \tag{6.62}$$

With the choice of the mass distribution and the specific gravity of the body, the coupling spring constant is specified. The equations for the displacement amplitudes are:

$$\begin{cases} |\varsigma_1|^2 = \dfrac{(\eta_2 - \chi_M\mu)^2 + \lambda_c^2}{(\alpha(\eta_2 - \chi_M\mu) - \lambda_c\lambda_{33} - \eta_2^2)^2 + (\lambda_{33}(\eta_2 - \chi_M\mu) + \lambda_c\alpha)^2}\, |f|^2, \\ |\varsigma_2|^2 = \dfrac{\eta_2^2}{(\alpha(\eta_2 - \chi_M\mu) - \lambda_c\lambda_{33} - \eta_2^2)^2 + (\lambda_{33}(\eta_2 - \chi_M\mu) + \lambda_c\alpha)^2} |f|^2\,. \end{cases} \tag{6.63}$$

The power is extracted from the motion of the internal mass now and is given by:

$$\frac{P}{\frac{\pi}{2}\rho V_s^3 \zeta_0^2} = \frac{\bar{a}^3 v^{3/2} \lambda_c \eta_2^2 |f|^2}{(\alpha(\eta_2 - \chi_M\mu) - \lambda_c\lambda_{33} - \eta_2^2)^2 + (\lambda_{33}(\eta_2 - \chi_M\mu) + \lambda_c\alpha)^2}, \tag{6.64}$$

while the power density is:

$$\frac{P}{MV_s^3\zeta_0^2/(2h^3)} = \frac{v^{3/2}\lambda_c\eta_2^2|f|^2/\mu}{(\alpha(\eta_2 - \chi_M\mu) - \lambda_c\lambda_{33} - \eta_2^2)^2 + (\lambda_{33}(\eta_2 - \chi_M\mu) + \lambda_c\alpha)^2}, \tag{6.65}$$

The optimal value for η_1 that maximizes (6.64) is seen to be:

$$\eta_1^{opt} = (1 - \chi_M)\mu + \mu_{33} - \eta_2 + \frac{\eta_2^2(\eta_2 - \chi_M\mu)}{(\eta_2 - \chi_M\mu)^2 + \lambda_c^2}. \tag{6.66}$$

The optimal damping value turns out to be:

$$\lambda_c^{opt} = \frac{\sqrt{(\alpha(\eta_2 - \chi_M\mu) - \eta_2^2)^2 + \lambda_{33}^2(\eta_2 - \chi_M\mu)^2}}{\sqrt{\alpha^2 + \lambda_{33}^2}}. \tag{6.67}$$

Equations (6.62, 66 & 67) need to be solved simultaneously. It turns out that they are not so coupled and they admit 3 different closed form solutions. Check Appendix 6.B for a solution of these equations.

Again we have to make sure the initial displacement of the springs is small enough. Starting with the dynamic balance at equilibrium:

$$\begin{cases} -M_f g + \pi a^2 \rho g H - k_1\Delta_1 - k_2(\Delta_1 - \Delta_2) = 0\,, \\ -M_i g + k_2(\Delta_1 - \Delta_2) = 0\,. \end{cases} \tag{6.68}$$

In dimensionless form:

$$\begin{cases} \eta_1\delta_1 + \eta_2(\delta_1 - \delta_2) = \dfrac{1 - (1 - \chi_M)\chi}{v\bar{a}}\,, \\ \eta_2(\delta_1 - \delta_2) = \dfrac{\chi_M\chi}{v\bar{a}}\,. \end{cases} \tag{6.69}$$

Solving for the displacements:

$$\begin{cases} \delta_1 = \dfrac{1 - \chi}{\eta_1 v\bar{a}}\,, \\ \delta_2 = \dfrac{1 - \chi}{\eta_1 v\bar{a}} - \dfrac{\chi_M\chi}{\eta_2 v\bar{a}}\,, \end{cases} \tag{6.70}$$

We would like to limit the absolute values of these displacements to l_1 and l_2. The first relation simply leads to:

$$\eta_1 \geq \frac{|1 - \chi|}{l_1 v\bar{a}}. \tag{6.71}$$

The second can be written as:

$$\left|\frac{\chi_M\chi}{\eta_2 v\bar{a}}\right| = |\delta_2 - \delta_1| \leq |\delta_1| + |\delta_2| \leq l_1 + l_2\,, \tag{6.72}$$

$$\eta_2 \geq \frac{\chi_M|\chi|}{(l_1 + l_2)v\bar{a}}. \tag{6.73}$$

If η_1 and η_2 fail to meet either of the constraints (6.71, 73), the failing constraints will be treated as equalities to ensure optimal performance that meets all conditions. These constraints will be referred to as conditions 1 and 2 respectively. Four cases arise depending on whether

each of the constraints is satisfied or not. For the case when both conditions are satisfied, we can proceed to compute the power directly. For all other cases, we must set one or both conditions to equality.

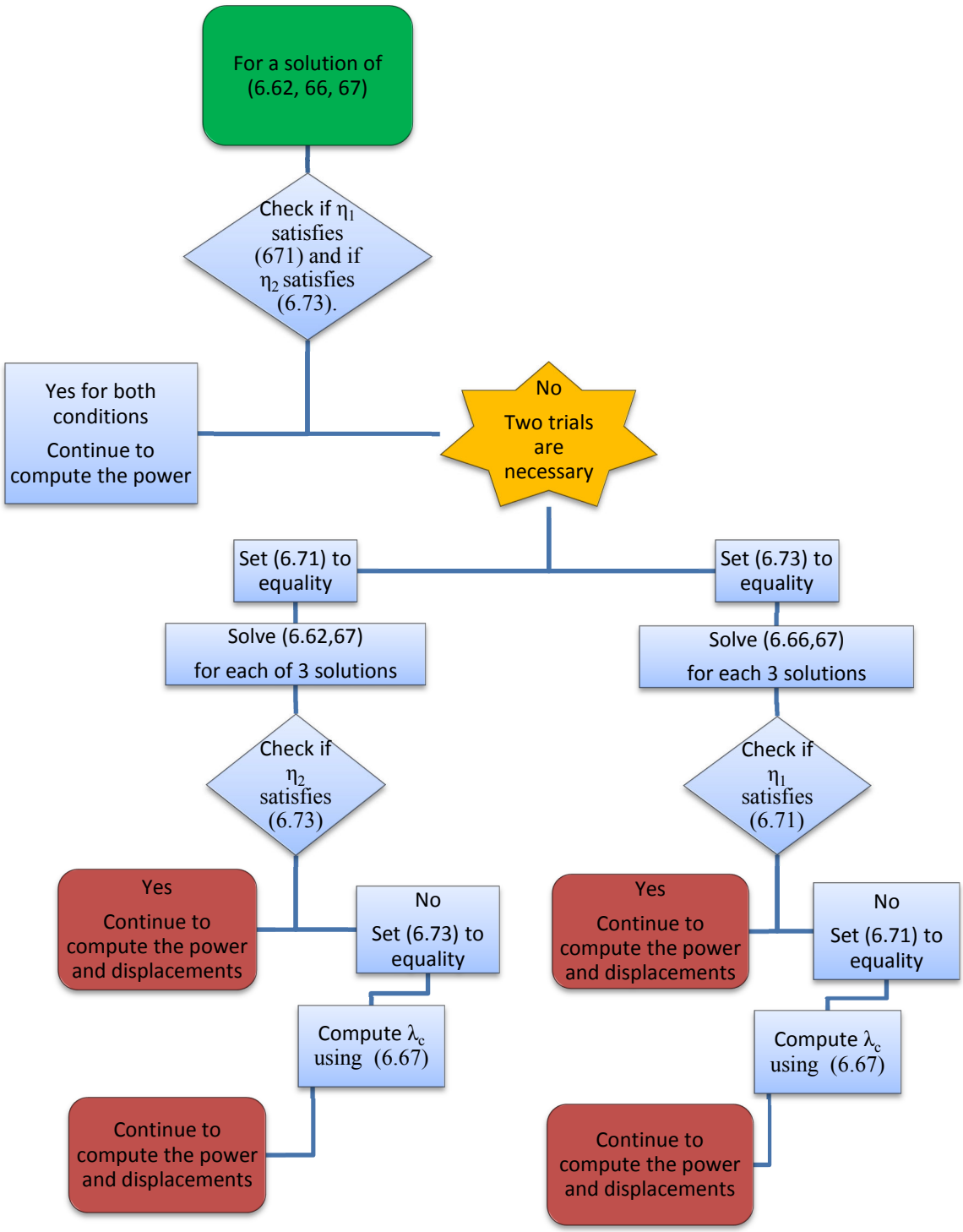

Figure 6-8: Flowchart for the algorithm which decides on the AWS characteristic spring constants

Up to three solutions may arise for equations (6.62, 66 & 67) depending on the presence of complex solutions. For each real solution, we should proceed as in Figure 6-8.

We would like to use the result which yields the higher displacement ratio. Depending on that, the output of the two trials at the orange star in Figure 6-8 should be compared and whichever is higher must be chosen. Now we can compare the outputs for the three solutions (i.e. 3 processes like the one in the figure) and make a choice of the parameters accordingly. It turns out that achieving a high displacement ratio ($\gg 1$) is not possible in practice for all the possible solutions. The ratio does not vary significantly from unity. This is clearly shown in figure 6-9. The legend in the top row can be used for the power and power density plots.

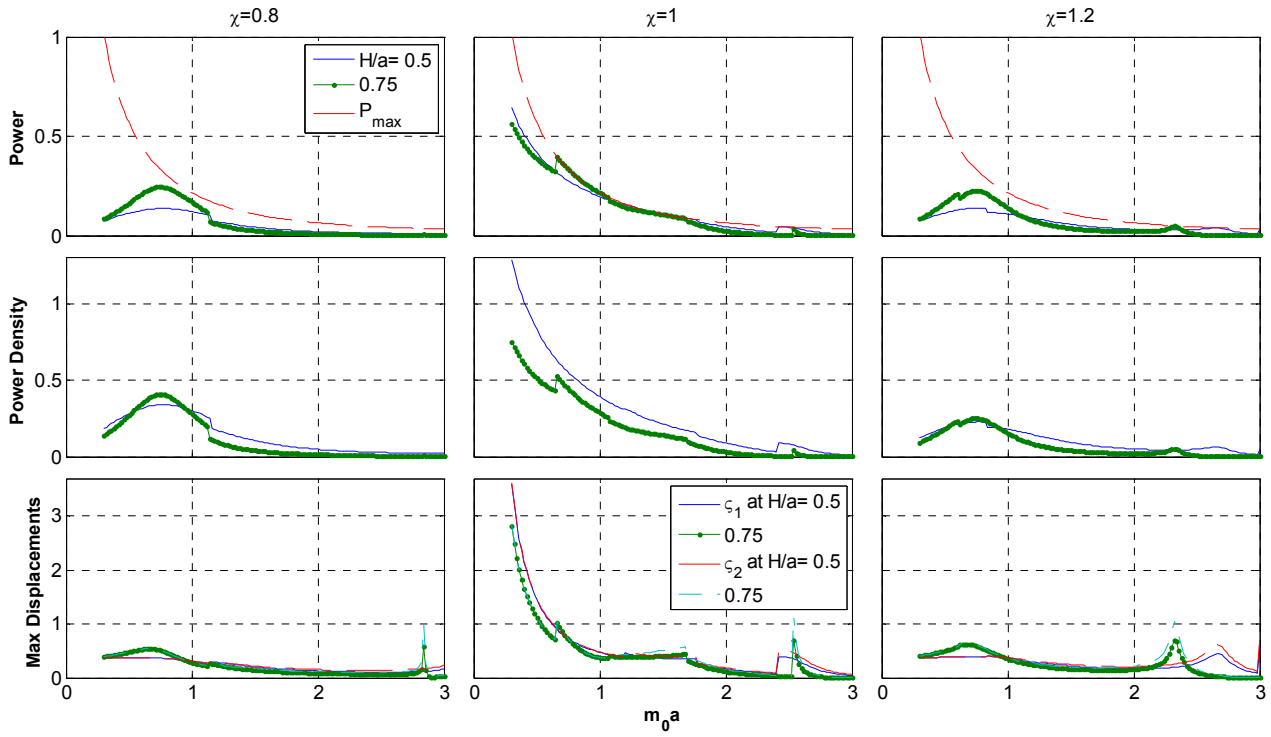

Figure 6-9: Plots for power (row 1), power density (row 2), and displacements (row 3) of the floater and internal mass of the AWS at $a = 1$, $\chi_m = 0.5$ and $l_1 = l_2 = 0.1$ as a function of wavenumber and for three χ and two H/a values with the theoretical maximum power output also shown

This figure clearly shows the effect of the applied conditions on the decline of the power as compared to the theoretical limit (also shown in the power plot). This decline is also partly due to the fact that we are not using the optimal value for η_2 as set by equation (6.62). This effect is most pronounced at the higher edge of the bandwidth and the low frequency effect is entirely due to the conditions (mainly (6.71) which can also be seen in Figure (6-7)). This fact is quite evident

for the case when $\chi = 1$ when the conditions do not apply unless the optimal spring values are negative. The mass distribution ration χ_m was found to have a limited effect on the performance, basically making the condition (6.73) more difficult to satisfy. The reduction in power due to this condition can be seen in the jump of the power curves in Figure (6-9). The power output for the body with an internal oscillator is obviously less (though not much) than that by oscillator free counterpart.

6.4 Conclusion

In this chapter, the case of the Archimedes Wave Swing (AWS), which is a submerged wave energy converter, was studied. The contribution included the effect of an added internal oscillator that was supposed to modify the dynamics of the system so as to reduce the motion of the external cover and extract energy from the internal system instead. The hydrodynamic forces were computed using the methods of the previous chapters and were reported in the form of plots. The most interesting observation about the excitation forces is the presence of nodes where the force complex amplitude diminishes to zero and reverses polarity. This will causes a sudden jump in the phase angle by a value of π.

The power output of a model device that is not coupled to an internal system was then presented to use as a basis for comparison. The results clearly indicate the effect of the condition, which was set on the internal spring, on the power output. The condition limits the power output at low frequencies and pulls it below its maximum limit.

The main results of the chapter concerned the performance of the AWS with an internal mass-spring system. The intention was to design the system so as to limit the external movement of the device and to, as much as possible, restrain this motion to the internal oscillator. Although the system was optimized to perform according to plan, the results indicate great difficulty in achieving this goal. The power output is slightly less than that for the case with no internal mass. The distribution of mass between the external floater and the internal system is seen to have little impact on the general performance having some advantage when more mass is located in the floater ($\chi_m \ll 1$).

Probably one of the key observations of this work is the convenience of designing the body so as to have a density close to that of the fluid density ($\chi = 1$). The buoyancy force in this case balances the mass of the system and the initial forces on the springs are negligible. This relieves the system from much of the constraints set on the spring characteristics and optimal values can be used in practice. This appreciably changes the power outcome, especially at low frequencies.

6.5 Appendices

Appendix 6.A

Evaluation of Different Expressions from Chapter 6

These are the expressions presented in Chapter 4 and not fully evaluated for brevity.

From (6.16),

$$\alpha_n{}^* = \begin{cases} \hat{u}\int_0^d \left(z' + \frac{1}{v} - d\right)\frac{\cosh(\lambda_0 z')}{\sqrt{M_0}}\,dz' = \frac{\hat{u}}{\lambda_0^2\sqrt{M_0}} & (n=0), \\ \hat{u}\int_0^d \left(z' + \frac{1}{v} - d\right)\frac{\cos(\lambda_n z')}{\sqrt{M_n}}\,dz' = \frac{-\hat{u}}{\sqrt{M_n}\lambda_n^2} & (n>0), \end{cases} \tag{6.A.1}$$

where the dispersion relation (6.12) was used.

From (6.22),

$$\begin{cases} C_{00} = \int_H^1 \frac{\cosh(\lambda_0(z-H))\cosh(m_0 z)}{\sqrt{M_0 N_0}}\,dz = \frac{-1}{\sqrt{M_0 N_0}}\frac{m_0\sinh(m_0 H)}{m_0^2 - \lambda_0^2}\ , \\ C_{0k} = \int_H^1 \frac{\cosh(\lambda_0(z-H))\cos(m_k z)}{\sqrt{M_0 N_k}}\,dz = \frac{-1}{\sqrt{M_0 N_k}}\frac{m_k\sin(m_k H)}{m_k^2 + \lambda_0^2}\ , \\ C_{n0} = \int_H^1 \frac{\cos(\lambda_n(z-H))\cosh(m_0 z)}{\sqrt{M_n N_0}}\,dz = \frac{-1}{\sqrt{M_n N_0}}\frac{m_0\sinh(m_0 H)}{m_0^2 + \lambda_n^2}\ , \\ C_{nk} = \int_H^1 \frac{\cos(\lambda_n(z-H))\cos(m_k z)}{\sqrt{M_n N_k}}\,dz = \frac{-1}{\sqrt{M_n N_k}}\frac{m_k\sin(m_k H)}{m_k^2 - \lambda_n^2}\ , \end{cases} \tag{6.A.1}$$

where the dispersion relations (6.12) and (2.41) were used.

From (6.29),

$$\psi_n^* = \begin{cases} \dfrac{1}{J_0(\lambda_0 a)} \displaystyle\int_0^a r J_0(\lambda_0 r) dr = \dfrac{a}{\lambda_0} \dfrac{J_1(\lambda_0 a)}{J_0(\lambda_0 a)} & (n = 0)\,, \\ \dfrac{1}{I_0(\lambda_n a)} \displaystyle\int_0^a r I_0(\lambda_n r) dr = \dfrac{a}{\lambda_n} \dfrac{I_1(\lambda_n a)}{I_0(\lambda_n a)} & (n > 0)\,. \end{cases} \tag{6.A.2}$$

The Wronskian relation was given in (4.53):

$$J_k(m_0 a) H_k'(m_0 a) - J_k'(m_0 a) H_k(m_0 a) = \frac{2i}{\pi a}\,.$$

If we use that in (6.38),

$$\begin{aligned} \alpha_{pn}^* &= \sum_{k=0}^{\infty} \int_0^d \int_0^{2\pi} \frac{2\epsilon_k i^k}{\pi a H_k'(m_0 a)} \frac{Z_0(z)}{Z_0'(1)} \cos(k\theta)\, \xi_n(z') \cos(p\theta)\, d\theta dz' \\ &= \frac{4 i^p C_{n0}}{a H_p'(m_0 a) Z_0'(1)}. \end{aligned} \tag{6.A.3}$$

$$\alpha_{0n}^* = \frac{-4\sqrt{N_0} C_{n0}}{a m_0^2 H_1(m_0 a) \sinh(m_0)}\,. \tag{6.A.4}$$

Appendix 6.B

Solution of equations (6.62, 66 & 67)

The equations mentioned can be simplified in the following manner:

Case 1: All 3 equations

$$\eta_2 = \frac{(\chi_M \mu)^2 + \lambda_c^2}{\chi_M \mu}\,, \tag{6.B.1}$$

$$\eta_1 = (1-\chi_M)\mu + \mu_{33} - \eta_2 + \frac{\eta_2^2(\eta_2 - \chi_M\mu)}{(\eta_2 - \chi_M\mu)^2 + \lambda_c^2}, \tag{6.B.2}$$

$$\lambda_c = \frac{\sqrt{(\alpha(\eta_2 - \chi_M\mu) - \eta_2^2)^2 + \lambda_{33}^2(\eta_2 - \chi_M\mu)^2}}{\sqrt{\alpha^2 + \lambda_{33}^2}}, \tag{6.B.3}$$

with α given in (6.59) by:

$$\alpha = \eta_1 + \eta_2 - (1-\chi_M)\mu - \mu_{33}\,. \tag{6.B.4}$$

These equations can be rewritten in the form:

$$A\eta_2 = A^2 + \lambda_c^2\,, \tag{6.B.5}$$

$$\begin{aligned}\eta_1(\eta_2 - A)^2 + \eta_1\lambda_c^2 + \eta_2(\eta_2 - A)^2 + \eta_2\lambda_c^2 \\ = B(\eta_2 - A)^2 + B\lambda_c^2 + \eta_2^2(\eta_2 - A)\,,\end{aligned} \tag{6.B.6}$$

$$\lambda_c^2(\alpha^2 + \lambda_{33}^2) = (\alpha(\eta_2 - A) - \eta_2^2)^2 + \lambda_{33}^2(\eta_2 - A)^2, \tag{6.B.7}$$

where we define the known constants:

$$\begin{cases} A = \chi_M\mu\,, \\ B = (1-\chi_M)\mu + \mu_{33}\,. \end{cases} \tag{6.B.8}$$

If we expand (6.B.6) and substitute (6.B.5) in where possible, the equation can be factored in the form:

$$(\eta_1 - B)(\eta_2^2 - A\eta_2) = 0\,, \tag{6.B.9}$$

which has 3 solutions. The solution $\eta_2 = 0$ is obviously rejected and the solution $\eta_2 = A$ leads to $\lambda_c = 0$ from (6.B.5) and is rejected as well. We can therefore conclude that:

$$\eta_1 = B. \tag{6.B.10}$$

That substituted into (6.B.4) and the result substituted into (6.B.7) and using (6.B.5) leads to:

$$\eta_2{}^3 - (2A + \lambda_{33}^2/A)\eta_2{}^2 + 3\eta_2\lambda_{33}^2 - 2A\lambda_{33}^2 = 0\,. \tag{6.B.11}$$

This is a third order polynomial whose solution is easily found. Three solutions arise, and for each of those, (6.B.5) gives a corresponding solution for λ_c (only the positive answer is taken) so that these solutions can be written as:

$$S_1 = \begin{cases} \eta_1 = (1-\chi_M)\mu + \mu_{33}\,, \\ \eta_2 = 2\chi_M\mu\,, \\ \lambda_c = \chi_M\mu\,. \end{cases} \tag{6.B.12}$$

$$S_2 = \begin{cases} \eta_1 = (1-\chi_M)\mu + \mu_{33}\,, \\ \eta_2 = \dfrac{\lambda_{33}^2 - \lambda_{33}\sqrt{\lambda_{33}^2 - (2\chi_M\mu)^2}}{2\chi_M\mu}\,, \\ \lambda_c = \sqrt{\dfrac{\lambda_{33}^2}{2} - \dfrac{\lambda_{33}}{2}\sqrt{\lambda_{33}^2 - (2\chi_M\mu)^2} - (\chi_M\mu)^2}\,. \end{cases} \tag{6.B.13}$$

$$S_3 = \begin{cases} \eta_1 = (1-\chi_M)\mu + \mu_{33}\,, \\ \eta_2 = \dfrac{\lambda_{33}^2 + \lambda_{33}\sqrt{\lambda_{33}^2 - (2\chi_M\mu)^2}}{2\chi_M\mu}\,, \\ \lambda_c = \sqrt{\dfrac{\lambda_{33}^2}{2} + \dfrac{\lambda_{33}}{2}\sqrt{\lambda_{33}^2 - (2\chi_M\mu)^2} - (\chi_M\mu)^2}\,. \end{cases} \tag{6.B.14}$$

Case 2: Equations (6.66, 67)

From (6.B.6, 7),

$$\lambda_c^2 = -(\eta_2 - A)^2 + \frac{\eta_2^2(\eta_2 - A)}{\alpha}, \tag{6.B.15}$$

$$\lambda_c^2(\alpha^2 + \lambda_{33}^2) = (\alpha(\eta_2 - A) - \eta_2^2)^2 + \lambda_{33}^2(\eta_2 - A)^2, \tag{6.B.16}$$

Substituting (6.B.15) into (6.B.16) and simplifying leads to:

$$C_1\eta_1^3 + D_1\eta_1^2 + E_1\eta_1 + F_1 = 0\,, \tag{6.B.17}$$

$$C_1 = -2A^2 + 4\eta_2 A - 2\eta_2^2\,, \tag{6.B.18}$$

$$D_1 = (6A^2 - 12\eta_2 A + 6\eta_2^2)B - 6\eta_2 A^2 + 9\eta_2^2 A - 3\eta_2^3\,, \tag{6.B.19}$$

$$\begin{aligned} E_1 = {} & (-2A^2 + 4\eta_2 A - 2\eta_2^2)\lambda_{33} + (-6A^2 + 12\eta_2 A - 6\eta_2^2)B^2 \\ & + (12\eta_2 A^2 - 18\eta_2^2 A + 6\eta_2^3)B - 6\eta_2^2 A^2 + 6\eta_2^3 A \\ & - \eta_2^4\,, \end{aligned} \tag{6.B.20}$$

$$\begin{aligned} F_1 = {} & \left((2A^2 - 4\eta_2 A + 2\eta_2^2)B - 2\eta_2 A^2 + 3\eta_2^2 A - \eta_2^3\right)\lambda_{33}^2 \\ & + (2A^2 - 4\eta_2 A + 2\eta_2^2)B^3 \\ & + (-6\eta_2 A^2 + 9\eta_2^2 A - 3\eta_2^3)B^2 \\ & + (6\eta_2^2 A^2 - 6\eta_2^3 A + \eta_2^4)B - 2\eta_2^3 A^2 + \eta_2^4 A\,. \end{aligned} \tag{6.B.21}$$

The polynomial has three solutions (complex solutions are to be rejected) and three values for λ_c follow from (6.B.15).

Case 3: Equations (6.62, 67)

$$A\eta_2 = A^2 + \lambda_c^2\,, \tag{6.B.22}$$

$$\lambda_c^2(\alpha^2 + \lambda_{33}^2) = (\alpha(\eta_2 - A) - \eta_2^2)^2 + \lambda_{33}^2(\eta_2 - A)^2, \tag{6.B.23}$$

If we simply insert (6.B.22) and (6.B.4) into (6.B.23) and simplify then we obtain:

$$A\eta_2^3 + C_2\eta_2^2 + D_2\eta_2 + E_2 = 0\,, \tag{6.B.24}$$

$$\begin{cases} C_2 = -\lambda_{33}^2 - B^2 + 2\eta_1 B - 4AB - 2A^2 + 4\eta_1 A - \eta_1^2\,, \\ D_2 = 3A\lambda_{33}^2 + 3AB^2 + 4A^2 B - 6\eta_1 AB - 4\eta_1 A^2 + 3\eta_1^2 A\,, \\ E_2 = -2A^2\lambda_{33}^2 - 2A^2 B^2 + 4\eta_1 A^2 B - 2\eta_1^2 A^2\,, \end{cases} \tag{6.B.25}$$

which is a third order polynomial that has three distinct solutions and can be solved easily. Three values for λ_c follow from (6.B.22).

Part 4 Numerical Aspects and Conclusion

Chapter 7 Some Numerical Aspects

It is somewhat straightforward to code the solutions for the problems presented. However, some numerical problems may arise either because of machine limitations (especially in computing limiting values) and because of the nature of the problem itself. It is the purpose of this chapter to clarify the procedures needed to achieve a reliable program. Here, we deal with various numerical aspects such as convergence, precision and limits. The pitch and coupled surge-pitch radiation problems are considered here for demonstration. The qualitative behavior of the results applies equally well in the other problems.

7.1 Error and Convergence

To deal with convergence, let us first define an appropriate error value. Instead of analyzing each parameter by itself, let us use the absolute value of these parameters (the absolute value of the impedance). From (4.36, 73), this is given by the infinite series:

$$\begin{aligned}\Lambda^{55} &= |\mu_{55} + i\lambda_{55}| \\ &= \left|\left(\frac{6ad^2 - a^3}{48d}\right) - \frac{1}{a^3}\sum_{n=0}^{\infty}\alpha_n(-1)^n\psi_n^* \right. \\ &\left. - \frac{1}{a^2}\sum_{k=0}^{\infty}A_k\frac{R_k(a)}{R_k'(a)}Z_k^*\right| .\end{aligned} \tag{7.1}$$

$$\Lambda^{51} = |\mu_{51} + i\lambda_{51}| = \left|-\frac{1}{a^2}\sum_{k=0}^{\infty}A_k\frac{R_k(a)}{R_k'(a)}\Gamma_k^*\right|. \tag{7.2}$$

In practice, both series will be truncated after a big enough number of terms N. Therefore we define:

$$\Lambda_N^{55} = \left|\left(\frac{6ad^2 - a^3}{48d}\right) - \frac{1}{a^3}\sum_{n=0}^{N}\alpha_n(-1)^n\psi_n^* - \frac{1}{a^2}\sum_{k=0}^{N}A_k\frac{R_k(a)}{R_k'(a)}Z_k^*\right|, \tag{7.3}$$

$$\Lambda_N^{51} = \left| -\frac{1}{a^2} \sum_{k=0}^{N} A_k \frac{R_k(a)}{R_k'(a)} \Gamma_k^* \right|. \tag{7.4}$$

Now if we consider that Λ_{100}^{5j} is a good approximation to Λ^{5j} $(j = 1,5)$, then we can use it to define the % error values:

$$E_N^{5j} = \frac{\left|\Lambda_{100}^{5j} - \Lambda_N^{5j}\right|}{\Lambda_{100}^{5j}} \times 100, \tag{7.5}$$

These error values were found to decay approximately as a function of $1/N^2$ (this was found to be a better fit than an exponential decay) if the oscillations were neglected. They can be fitted into rational functions of the form $\frac{a_{5j}}{b_{5j}N^2+c_{5j}N+d_{5j}}$. The following figures show some examples of the variation of Λ_N^{5j} as a function of N and how it converges to Λ_{100}^{5j} (first row) and the variation of the error E_N^{5j} and its curve fit as a function of N on a log plot to better present the small error values (second row).

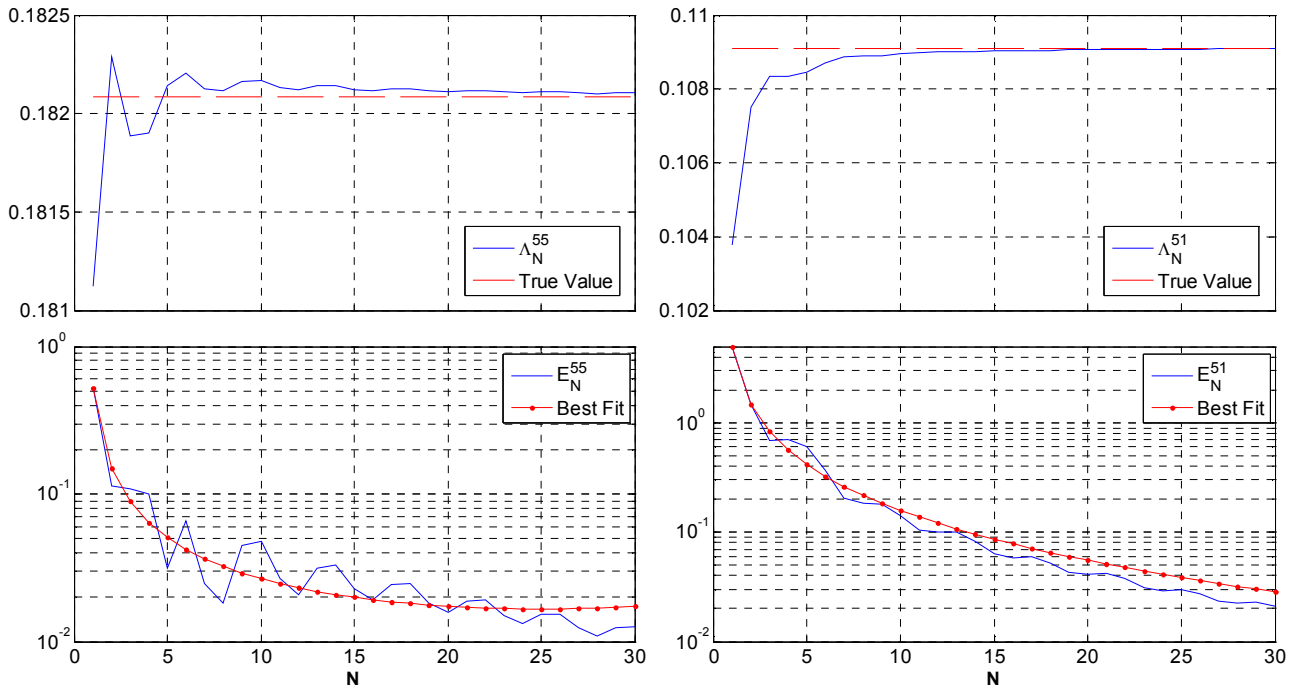

Figure 7-1: Solution convergence (row 1) and error decay (row 2, log plot) as a function of the number of harmonics used for the pitch (left) and coupled pitch-surge (right) problems at $m_0 = 2$, $a = 1$ and $d = 0.75$

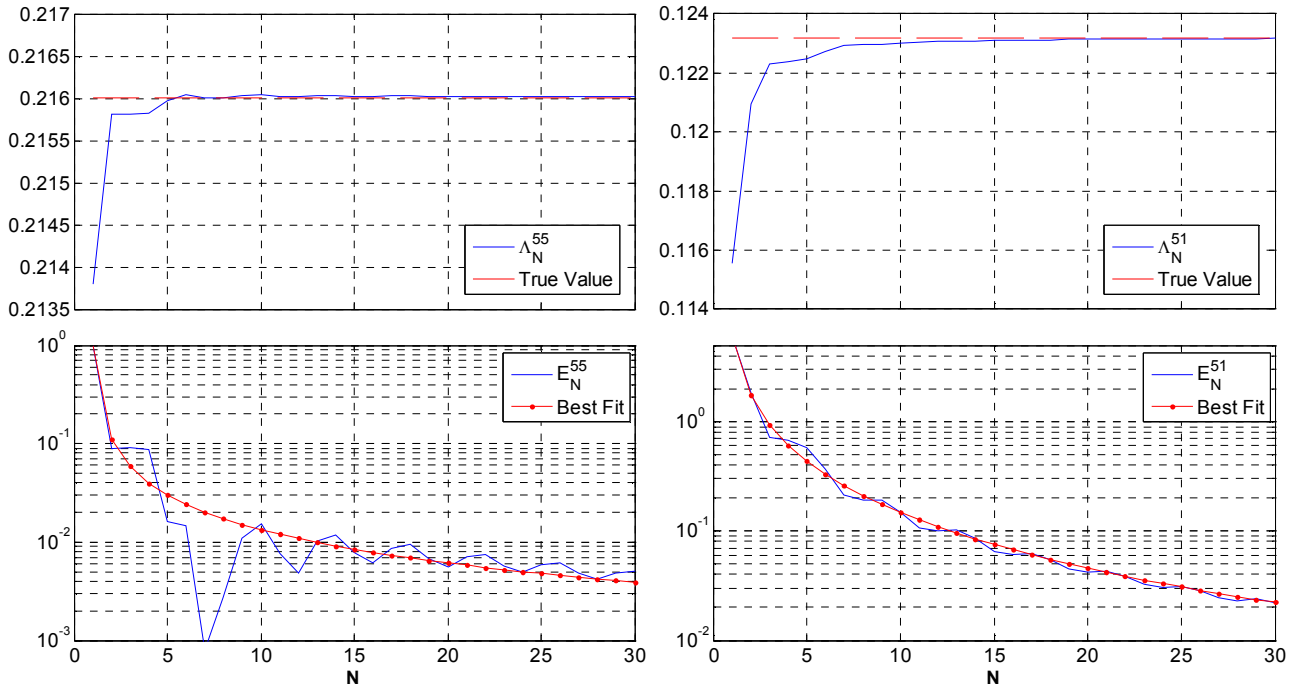

Figure 7-2: Solution convergence (row 1) and error decay (row 2, log plot) as a function of the number of harmonics used for the pitch (left) and coupled pitch-surge (right) problems at $m_0 = 1.5$, $a = 1$ and $d = 0.75$

In the limit of high N values, the error will then tend to $a_{5j}/(b_{5j}\,N^2)$. The parameter that determines the speed of convergence of the series is $\lambda_{5j} = a_{5j}/b_{5j}$. We estimate the value of λ_{5j} from the curve fits and plot it against the radius a and for some values of d and m_0 in Figures 7-3, 7-4 and 7-5.

7.2 Richardson Extrapolation

The series at hand obviously converge very fast. Nonetheless, if extensive computations of many cases are needed such as in the case of computing the power from irregular waves, it is worthwhile to look into convergence acceleration methods. These require a smaller number of harmonic terms to achieve a certain precision and therefore require far less computational effort.

A technique called the Richardson Extrapolation is handy in this case and is simple to implement. The first Richardson Extrapolate of Λ_N^{5j} is the series defined as:

$$\Omega_N^{5j} = \Lambda_N^{5j} + \frac{\Lambda_N^{5j} - \Lambda_{N/2}^{5j}}{3}, \tag{7.6}$$

where only even values for N are considered. Using this as an approximation to the series Λ^{5j} requires less harmonics to reach a certain precision. We show that by some examples, but first we define the % error values:

$$\Sigma_N^{5j} = \frac{\left|\Lambda_{100}^{5j} - \Omega_N^{5j}\right|}{\Lambda_{100}^{5j}} \times 100, \tag{7.7}$$

The error from the regular summation E_N^{5j} decays exponentially as we showed before. Therefore it is only reasonable to expect a modest improvement using the Richrdson approximants. A plot of these errors as a function of the number of harmonics used shows that clearly:

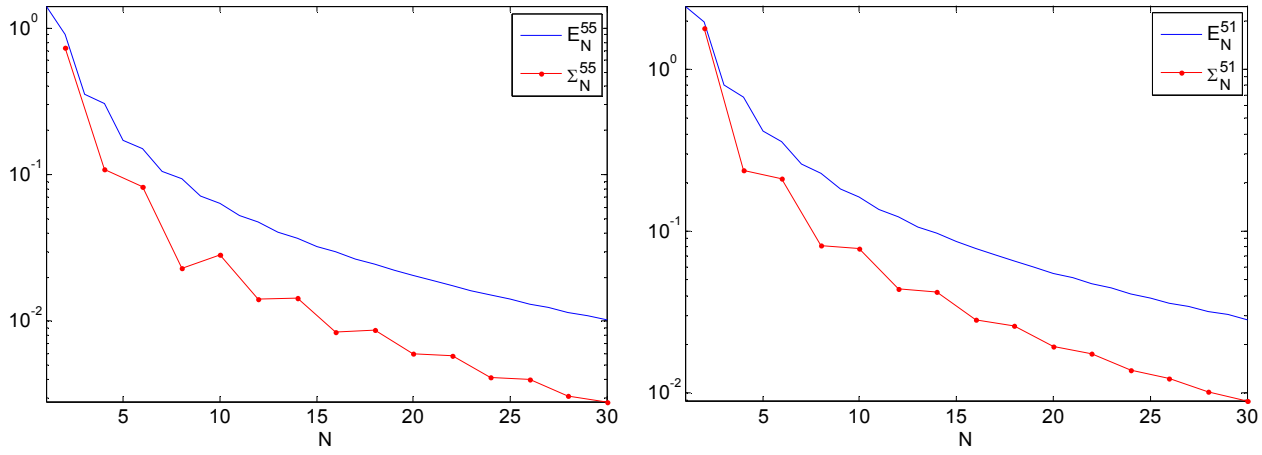

Figure 7-3: Richardson error enhancement compared to regular summation at $m_0 = 1$, $a = 0.5$ and $d = 0.5$ for the pitch (left) and coupled pitch-surge (right) problems

Although the decrease in error is very modest when using this method, the computational effort required to reach a certain precision is far less than simple summation. This method will therefore be adopted in the computations. It is worthy to point out though that in some cases, the error Σ_N^{5j} may be alternating in magnitude with E_N^{5j} as N increases (Figure 7-5).

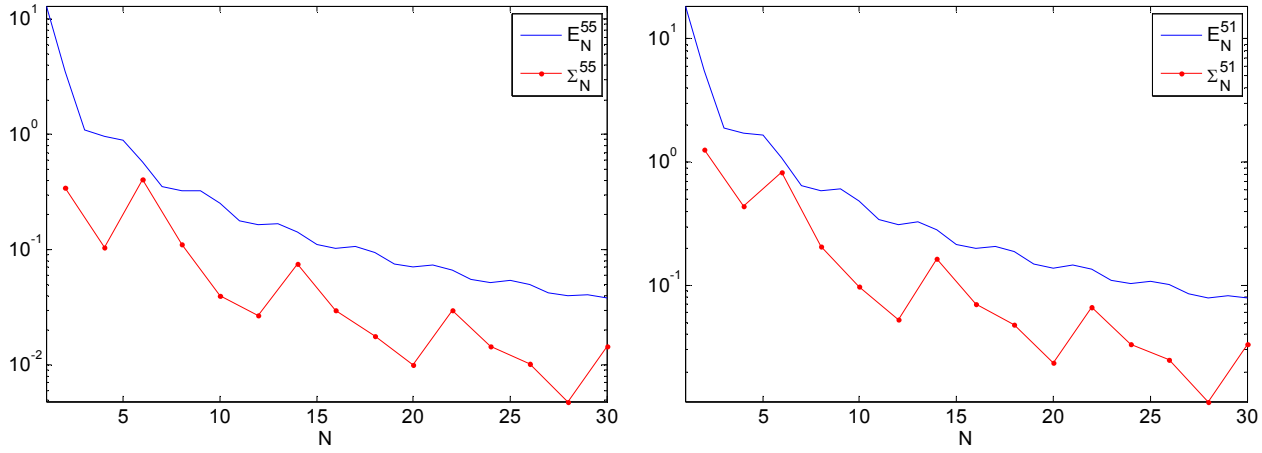

Figure 7-4: Richardson error enhancement compared to regular summation at $m_0 = 1$, $a = 0.5$ and $d = 0.75$ for the pitch (left) and coupled pitch-surge (right) problems

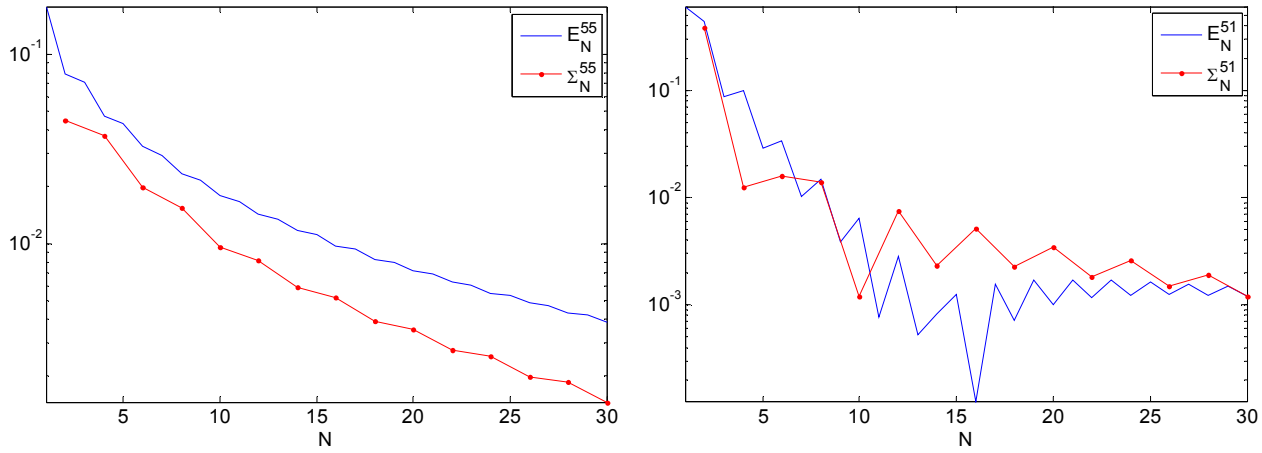

Figure 7-5: Richardson error enhancement compared to regular summation at $m_0 = 1$, $a = 1$ and $d = 0.5$ for the pitch (left) and coupled pitch-surge (right) problems

7.3 Choosing the Number of Required Harmonics

An important question to ask when running the program is how many terms should be kept in the series given by (7-3, 4) or any similar equations? That is, what is the suitable value for N? Choosing a smaller than needed value means imprecise results while choosing a larger than needed value may be very expensive. To gain some insight, we consider what values of N are

required to achieve a specified precision for each case. Certainly we expect these values to depend on the specified geometry of the problem. Advanced work might even go into forming a model for the dependence of N on the geometry and then use that model in the code. Although this is fairly simple as a linear model will do just fine, we shall not go that far and will only consider using a fixed value.

Let us say we want the errors E_N^{5j} and Σ_N^{5j} to be less than 0.1%, then for each value of m_0, a and d, we would like to know the required value of N. Alternatively, a tolerance value for Λ_N^{5j} and Ω_N^{5j} may be set as a basis instead of the error. Table 7-1 shows the number of harmonics required to achieve the required precision. In this table, N_{5j} represents the number of harmonics required for direct summation while N_{5jr} represents those required when using the Richardson Extrapolation. The results show the advantage of using the Richardson extrapolation method. The mean N_{55} in this table is 7.69 while the mean N_{55r} is 5.91 and the mean N_{51} is 9.55 while that of N_{51r} is 6.28, which represents a reduction of computational effort.

Had we decided to choose an error of 0.01% instead, the results and mean values would have clearly shown the advantage of using the Richardson extrapolation. In that case, the mean N_{55} is 37.6 while the mean N_{55r} is 20.7 and the mean N_{51} is 28.6 while that of N_{51r} is 17.4, which represents a significant reduction of computational effort when considering that the computational time is expected to be of the order of N^2.

We can also note that a higher number of harmonics is required at the corners of the shaded 4×4 blocks (both white and dark ones) where this number may go up to 30 terms for extreme cases when the body is small in size ($a/d < 1$) or when the body is very big in size ($a/d \gg 1$). This is possibly because of the relatively short variation lengths available rendering the potential less smooth and therefore requiring a larger number of harmonics. The fastest convergence is seen at the lower ends of a and d. Finally, the maximum numbers N_{55}, N_{55r}, N_{51} and N_{51r} that might be required are 30, 18, 29 and 14 respectively. If these maximums were to be used for all computations to ensure a bounded error, the computational expense would be considerably lower using the series acceleration scheme.

Table 7-1: Required number of harmonics to achieve 0.1% error while using and not using Richardson extrapolation and for different a, d and m_0 values for the pitch and the coupled pitch-surge problems

		N_{55}				N_{55r}				N_{51}				N_{51r}			
m_0	a \ d	0.5	1	1.5	2	0.5	1	1.5	2	0.5	1	1.5	2	0.5	1	1.5	2
0.5	0.2	3	5	11	12	2	6	8	8	3	10	12	12	4	2	8	8
	0.4	5	1	1	5	4	2	4	4	11	2	10	11	4	4	8	8
	0.6	11	2	2	1	6	2	2	2	17	6	1	9	10	4	2	2
	0.8	19	3	3	3	12	4	4	2	29	13	3	4	14	8	4	6
1	0.2	2	1	15	21	2	2	8	12	3	10	12	12	2	8	8	8
	0.4	6	3	1	8	4	4	2	6	11	2	10	10	4	4	8	8
	0.6	12	1	4	2	6	2	2	2	17	7	1	7	10	4	2	2
	0.8	19	3	4	3	10	2	4	4	29	14	6	2	14	10	2	4
1.5	0.2	2	1	22	27	4	6	12	18	3	10	11	11	4	8	8	2
	0.4	4	5	6	16	4	4	6	14	10	2	8	10	4	6	8	8
	0.6	11	2	4	5	6	6	2	2	17	7	2	2	10	4	6	6
	0.8	19	3	4	3	10	2	6	4	29	14	8	6	14	10	4	2
2	0.2	2	10	27	30	4	8	18	18	2	10	12	14	4	8	2	2
	0.4	3	5	15	22	4	4	8	14	9	2	10	8	4	6	8	8
	0.6	10	2	1	12	4	8	2	10	17	6	3	2	6	4	8	8
	0.8	19	2	4	2	10	6	6	4	29	14	9	8	14	10	4	8

Table 7-2 shows the mean harmonic values for each frequency separately. What we notice from the table is that the number of required harmonics almost always increases with frequency. The variation is more pronounced for the pitch problem.

Table 7-2: Averaged number of harmonics required for each value of m_0

m_0	N_{55}	N_{55r}	N_{51}	N_{51r}
0.5	5.43	4.5	9.56	6
1	6.56	4.5	9.56	6.12
1.5	8.37	6.62	9.37	6.5
2	10.37	8	9.68	6.5

We can notice a pattern if we average for each d value instead in Table 7-3. The number of harmonics required is higher at the high and low limits of d because of the extreme case effect mentioned earlier. Averaging over a seems to produce similar results; although not as clear.

Table 7-3: Averaged number of harmonics required for each value of d

d	N_{55}	N_{55r}	N_{51}	N_{51r}
0.2	11.9375	8.5	9.1875	5.375
0.4	6.625	5.5	7.875	5.5
0.6	5.125	4	7.5625	5.5
0.8	7.0625	5.625	12.094	8

7.4 Limiting Cases

Since we are dealing with modified Bessel functions, one might face problems with the limiting cases of these functions when running the program. For example, the ratio $R_k(a)/R_k'(a)$ from (7.1) is defined using:

$$R_k(r) = \begin{cases} H_1^{(1)}(m_0 r) & (k = 0), \\ K_1(m_k r) & (k > 0). \end{cases} \tag{7.8}$$

The function $K_1(m_k a)$ decays to zero exponentially when a is large and so does its derivative. This causes a numerical problem as the program faces the ratio of two numbers close to zero. Instead, we can use the limiting form of this function at a large radius. Using the fact that:

$$\lim_{a\to\infty} K_n(m_k a) = \sqrt{\frac{\pi}{2m_k a}}\, e^{-m_k a}\,, \tag{7.9}$$

Then the ratio converges to:

$$\lim_{a\to\infty} \frac{K_1(m_k a)}{K_1'(m_k a)} = \lim_{a\to\infty} \frac{-K_1(m_k a)}{\frac{m_k}{2}\left(K_0(m_k a) + K_2(m_k a)\right)} = \frac{-1}{m_k}. \tag{7.10}$$

Similarly, the limiting forms of the following ratios used in (4.31, 37) for instance is:

$$\lim_{a\to\infty}\frac{\psi_j'(a)}{\psi_j(a)}=\lim_{a\to\infty}\frac{I_1'(\lambda_k a)}{I_1(\lambda_k a)}=\lim_{a\to\infty}\frac{\frac{\lambda_k}{2}\left(I_0(\lambda_k a)+I_2(\lambda_k a)\right)}{I_1(\lambda_k a)}=\lambda_k\,, \tag{7.11}$$

$$\lim_{a\to\infty}\psi_k^*=\lim_{a\to\infty}a^2\frac{I_2(\lambda_k a)}{\lambda_k I_1(\lambda_k a)}=\frac{a^2}{\lambda_k}, \tag{7.12}$$

using the fact that:

$$\lim_{a\to\infty}I_n(\lambda_k a)=\frac{e^{\lambda_k a}}{\sqrt{2\pi\lambda_k a}}\left(1+\frac{(1-2n)(1+2n)}{8\lambda_k a}\right). \tag{7.13}$$

This has been found to be quite effective.

7.5 Finding the Roots of the Dispersion Relation

The dispersion relation was introduced in (2.41). For the evanescent modes, this relation is:

$$m_k\tan(m_k)-v=0. \tag{7.14}$$

This causes some problems if a regular root finding routine is used because the tangent function has discontinuities at the points $(2n+1)\pi/2$ and Matlab considers the points of discontinuities as zeros. Therefore these will be included with the roots. Instead, the root search must be carried out in the intervals in between (half of the interval actually were a single root lies). If a root finding routine is not available, one can simply take the minimum of the absolute value of the function in each interval which is approximately where the zero crossing point is.

7.6 Checking for the Quality of the Matching

Matching the potentials and normal velocities at the interface of the internal and external regions is done using a Galerkin method. This is an approximation off course as only the integrals of these potentials and velocities are truly matched. We would like to have an idea of how good is this approximation. A significant deviation from perfect matching may mean

inaccurate results for the forces and ultimately for the power output. So how good is the matching using this method?

Figures 7-6 and 7-7 present two cases that clearly show the quality of the matching method used. The potentials are found to match almost perfectly for $z < d$, even for a small number of harmonics which is quite remarkable. This is important as the pressure is proportional to the potentials. The velocities are seen to match well but somewhat not as much. The external velocity tends to equal z in a well behaved manner for $z > d$.

The overshoots that appear in the velocity plots at $z = d$ are the result of the so called Gibbs phenomenon which arises when harmonic components of a function are summed. These are inevitable in this case because of the sudden change occurring at the buoy edges; the edge effects. The Gibbs phenomenon is found to be more severe at higher frequencies (the matching is slightly better though) or at higher buoy radii. The increase of the overshoot with N is typical.

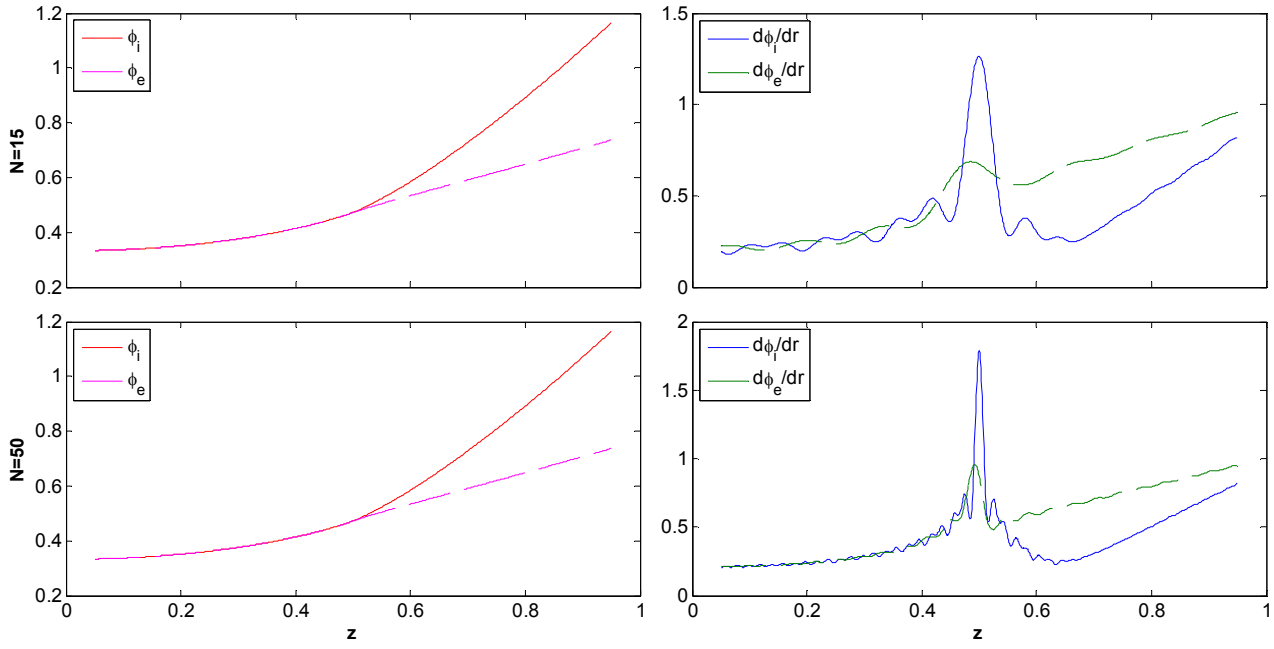

Figure 7-6: Matching the potentials (column 1) and normal velocities (column 2) for the pitch case with $a = 1, d = 0.5, m_0 = 1$ as a function of the altitude z showing the effect of the number of harmonics (15 harmonics in row 1 and 50 in row 2)

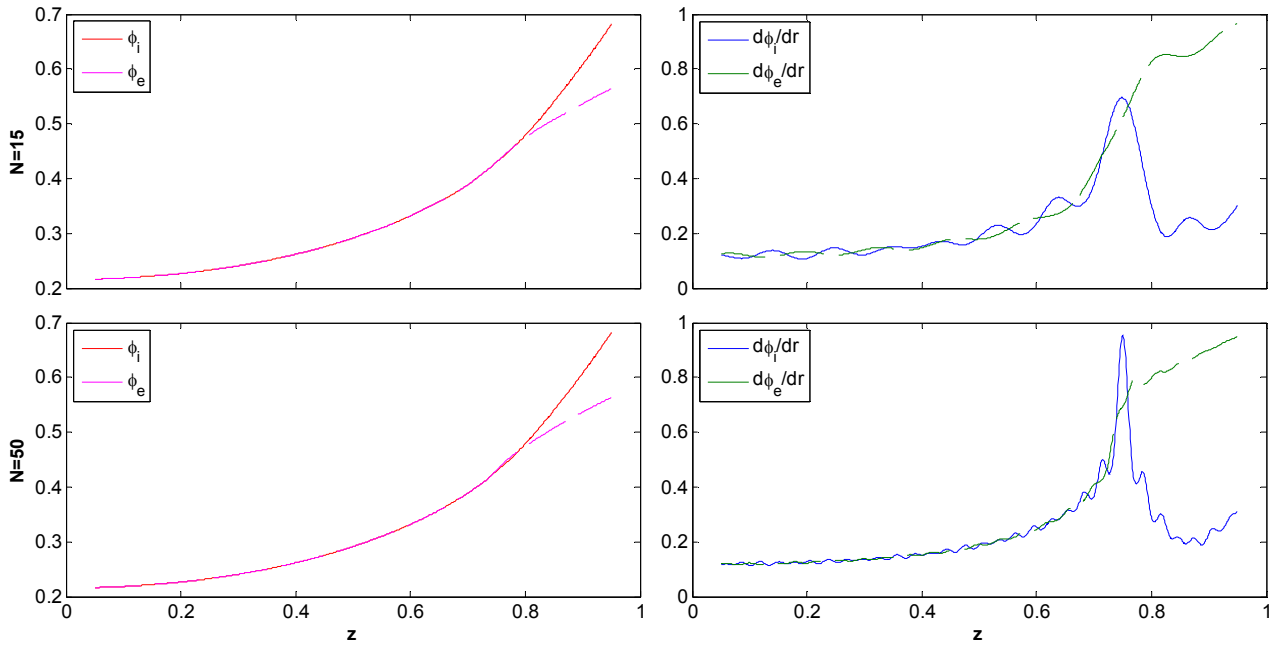

Figure 7-7: Matching the potentials (column 1) and normal velocities (column 2) for the pitch case with $a = 1, d = 0.75, m_0 = 1$ as a function of the altitude z showing the effect of the number of harmonics (15 harmonics in row 1 and 50 in row 2)

Chapter 8 Conclusion

This work dealt with the analysis of three different configurations of a basic element wave energy converter. The element is a truncated circular cylinder in water of finite depth. A frequency domain matched eigenfunction expansion procedure developed by Yeung [13] was extended to compute the hydrodynamic forces on the bodies of interest. The work studied the possibilities of extracting energy from the different configurations and possible improvements in terms of cost and performance.

The first part assessed the effect of a circular pole concentric to a floating cylinder on the wave power extraction characteristics of the system. For a fixed frequency, the results show that the same power values can be achieved with the absence or presence of the pole by simply increasing the radius of the buoy for the latter case. An interesting result is that higher peak power density values that are possible by employing the pole for certain buoy radii and drafts. The optimum geometrical parameters that achieve the highest power and power density values were also presented. The pole effect was also studied in irregular waves. In those conditions, the power density was found to be higher when the pole is present, a fact that is subtle for small pole radii but becomes quite evident for large ones. This is because of the mass that was replaced by the comparably massless pole indicating the substantial amount of "dead mass" being used in floating point absorbers. The power does decrease with the increasing pole thickness but the volume of the buoy decreases faster. The results presented thus far provide a valuable starting point for designing experiments to validate these results as well as to design similar wave energy converters.

The second part of the work had the goal of showing to what extent the power output is increased when the pitch mode is allowed. The results in regular wave indicate that the contribution from the pitch mode is highest at high incident wave frequencies and buoy radii where the heave power drops sharply. For a given submergence level, shorter buoys were found to produce more power while increasing the submergence (density) of the buoy shifts the peak power to lower frequencies, increases this peak and narrows the operable spectrum. The results for irregular waves indicate that flatter and lighter bodies perform better in terms of power extracted (theoretically at least). The power density results indicate a contrary behavior peaking

for slender buoys that are more submerged mainly because of the low optimal radii required in these situations.

Comparing the power results with those of a cylinder restricted to heave, we can tell that employing the added pitch mode can be useful in areas with a concentration of high frequency waves. This is usually associated with a high peak frequency of the spectrum which means that this system is most suitable in areas generally poor with the wave resource having low significant wave heights as indicated by the relation. Both, considering the added pole of part one or the pitch mode of part two, have the effect of increasing the power density of the buoy which will definitely decrease its capital cost. However, the cost of the pole itself or the added PTO equipment required in either case and their installation costs need to be considered as well. The information provided in the text is a helpful starting point for any design initiative.

The third part of this thesis dealt with the case of the Archimedes Wave Swing (AWS) and the effect of an added internal mass-spring system on its general performance. The goal was to make use of the added degree of freedom to design the system in a way so that the motion of the external floater is reduced and all the energy absorbed is transmitted to the internal mass. The results indicate that this is not possible to achieve and, at best, the two motions in question are of the same order. This is because of the difficulty of transmitting energy from the waves to the internal oscillator without significantly moving the external frame. The power output was compared with the case when the oscillator was absent and a small decrease in power resulted for the former case. This is mainly because of the constraints set on the springs used in the design; two for the case with internal mass instead of one. This shows that there is no real improvement associated with the scheme as it is. The system can be optimized to produce maximum power though and higher power outputs may potentially result as compared to the one mass system even with the added constraints. This matter is not pursued here though.

The effect of distributing the masses in a different manner (which is a design parameter) was found to have little effect being more beneficial as the internal mass becomes smaller, i.e. as it tends to the case without the oscillator inside. The results did show, however, that a significant enhancement to the performance (particularly at low frequencies) can be achieved by designing the system to have an average density close to that of the fluid.

It is interesting to note that the power output results for the AWS (Figure 6-9) compare quite well with those for the floating buoy (Figure 5-1 for instance). This shows the great potential for this device which is completely submerged and is therefore less vulnerable to storms. It is important to point out as well that for the cases when the density of the AWS system is close to that of the fluid, higher power outputs can be achieved as compared to the floating buoy at low frequencies. We have to remember, however, that slack mooring was assumed for the floating buoy which limits the power output to the values presented. Had the right spring been used, the theoretical maximum could have been achieved. This is difficult in practice though.

The work in Chapter 7 was an account of the numerical characteristics of the solutions or of the problems that may arise when implementing those solutions in computer codes. The case of the radiation forces of the multi DOF cylinder was considered. The convergence of the different series solutions was very good and can be modeled to be exponential. Use of the convergence acceleration method called Richardson Extrapolation was shown to significantly reduce the computational effort required. The work also tackled some of the problems that arise such as limiting values of the series components. The quality of the solution presented was reflected in the degree of matching of the potentials and normal velocities at the interface of the two regions considered and it was found to be quite satisfactory.

Future work includes diverse matters that still need to be considered. The individual effects of the radiation and diffraction forces on the general outcome are important when considering the sensitivity of the power extracted on the changes of these forces. These changes may arise because of the imperfections of the body shape, nonlinear effects and extreme conditions or geometries were linear models usually fail. Experimental results are needed to confirm any findings presented here and to provide real life proof of how efficient these models can be. Off course better models for the power takeoff mechanisms can be developed than the simple linear ones used here. Finally, the effect of second order forces and moments may be important and the routine to calculate these needs to be developed for the cases presented.

References

[1] R. Pelc and R. M. Fujita, "Renewable energy from the ocean," *Marine Policy*, vol. 26, no. 6, pp. 471-479, Nov. 2002.

[2] J. W. Tester, E. M. Drake, M. J. Driscoll, M. W. Golay, and W. A. Peters, *Sustainable Energy: Choosing Among Options*. The MIT Press, 2005.

[3] J. Ringwood, "Practical Challenges in Harvesting Wave Energy," in *ECOR Symposium*, St. John's, Newfoundland, 2008.

[4] K. Burman and A. Walker, *Ocean Energy Technology Overview*. U.S. Departement of Energy, 2009.

[5] C. C. Mei, M. Stiassnie, and D. K. P. Yue, *Theory and Applications of Ocean Surface Waves (Advanced Series on Ocean Engineering) 2 Vol. Set*, Expanded Ed. World Scientific Publishing Company, 2005.

[6] A. F. de O. Falcão, "Wave energy utilization: A review of the technologies," *Renewable and Sustainable Energy Reviews*, vol. 14, no. 3, p. 899, Jan. 2010.

[7] J. Falnes, "A review of wave-energy extraction," *Marine Structures*, vol. 20, no. 4, pp. 185-201, Oct. 2007.

[8] M. E. McCormick, *Ocean Wave Energy Conversion*. Dover Publications, 2007.

[9] D. V. Evans, "Power From Water Waves," *Annual Review of Fluid Mechanics*, vol. 13, no. 1, pp. 157-187, Jan. 1981.

[10] J. Cruz, *Ocean Wave Energy: Current Status and Future Prespectives*, 1st ed. Springer, 2008.

[11] K. Budal and J. Falnes, "A resonant point absorber of ocean-wave power," *Nature*, vol. 256, no. 5517, pp. 478-479, 1975.

[12] R. V. Chaplin and G. A. Aggidis, "An Investigation into Power from Pitch-Surge Point-Absorber Wave Energy Converters," in *2007 International Conference on Clean Electrical Power*, Capri, Italy, 2007, pp. 520-525.

[13] R. W. Yeung, "Added mass and damping of a vertical cylinder in finite-depth waters," *Applied Ocean Research*, vol. 3, no. 3, pp. 119-133, Jul. 1981.

[14] T. Sabuncu and S. Calisal, "Hydrodynamic coefficients for vertical circular cylinders at finite depth," *Ocean Engineering*, vol. 8, no. 1, pp. 25-63, 1981.

[15] P. Kjellgren and J. Hyvarinen, "An Arbitrary Lagrangian-Eulerian finite element method," *Computational Mechanics*, vol. 21, no. 1, pp. 81-90, Feb. 1998.

[16] H. Eidsmoen, "Hydrodynamic parameters for a two-body axisymmetric system," *Applied Ocean Research*, vol. 17, no. 2, pp. 103-115, 1995.

[17] M. Alves, H. Traylor, and A. J. N. A. Sarmento, "Hydrodynamic Optimization of a Wave Energy Converter Using a Heave Motion Buoy," in *Proceedings of the 6th Int. Conf. on Wave and Tidal Energy*, Porto, Portugal, 2007.

[18] B. J. Wu, Y. H. Zheng, Y. G. You, D. S. Jie, and Y. Chen, "On diffraction and radiation problem for two cylinders in water of finite depth," *Ocean Engineering*, vol. 33, no. 5-6, pp. 679-704, Apr. 2006.

[19] J. Falnes, *Ocean Waves and Oscillating Systems: Linear Interactions Including Wave-Energy Extraction*. Cambridge University Press, 2002.

[20] J. Miles and F. Gilbert, "Scattering of Gravity Waves by a Circular Dock," *Journal of Fluid Mechanics*, vol. 34, no. 4, pp. 783-793, 1968.

[21] C. J. R. Garrett, "Wave Forces on a Circular Dock," *Journal of Fluid Mechanics*, vol. 46, no. 1, pp. 129-139, 1971.

[22] J. L. Black, C. C. Mei, and M. C. G. Bray, "Radiation and Scattering of Water Waves by Rigid Bodies," *Journal of Fluid Mechanics*, vol. 46, no. 1, pp. 151-164, 1971.
[23] Q. W. Ma, G. X. Wu, and R. Eatock Taylor, "Finite element simulation of fully non-linear interaction between vertical cylinders and steep waves. Part 1: methodology and numerical procedure," *International Journal for Numerical Methods in Fluids*, vol. 36, no. 3, pp. 265-285, Jun. 2001.
[24] P. Ricci, J.-B. Saunier, and A. F. de O. Falcao, "Point-absorber arrays: a configuration study off the Portuguese West-Coast," in *Proc of the 7th European wave and tidal energy conf*, Porto, Portugal, 2007.
[25] A. J. N. A. Sarmento, A. M. Luis, and D. B. S. Lopes, "Frequency-domain analysis of the AWS device," in *Proceedings of the European Wave Energy Conference*, Patras, Greece, 1998.
[26] J. Sá da Costa, A. J. N. A. Sarmento, F. Gardner, P. Beirão, and A. Brito-Melo, "A time domain model of the Archimedes Wave Swing wave energy converter," in *Proceedings of the 6th European wave and tidal energy conference*, Glasgow, Scotland, 2005, p. 91–97.
[27] J. M. B. P. Cruz, A. J. N. A. Sarmento, and F. Gardner, "AWS pilot plant tests: wave characteristics," in *Proceedings of the 6th European Wave and Tidal Energy Conference*, Glasgow, Scotland, 2005, pp. 105-112.
[28] H. Polinder, M. E. C. Damen, and F. Gardner, "Design, modelling and test results of the AWS PM linear generator," *European Transactions on Electrical Power*, vol. 15, no. 3, pp. 245-256, May. 2005.
[29] M.-H. Kim and D. K. P. Yue, "The Complete Second-Order Diffraction Solution for an Axisymmetric Body Part 1. Monochromatic Incident Waves," *Journal of Fluid Mechanics*, vol. 200, pp. 235-264, 1989.
[30] M.-H. Kim and D. K. P. Yue, "The Complete Second-Order Diffraction Solution for an Axisymmetric Body Part 2. Bichromatic Incident Waves and Body Motions," *Journal of Fluid Mechanics*, vol. 211, pp. 557-593, 1990.
[31] Z. Yu and J. Falnes, "State-space modelling of a vertical cylinder in heave," *Applied Ocean Research*, vol. 17, no. 5, pp. 265-275, Oct. 1995.
[32] J. Falnes, "Optimum control of oscillation of wave-energy converters," *International Journal of Offshore and Polar Engineering*, vol. 12, no. 2, p. 147–154, 2002.
[33] Y. Masuda, "OCEAN WAVE ELECTRIC GENERATOR," U.S. Patent 3,204,11031-Aug-1965.
[34] V. Baudry and A. Babarit, "Assessment of the annual energy production of a heaving wave energy converter sliding on the mast of a fixed offshore wind turbine," in *Proceedings of the World Renewable Energy Congress XI*, Abu Dhabi, UAE, 2010.
[35] C. C. Mei, *Mathematical Analysis in Engineering: How to Use the Basic Tools*. Cambridge University Press, 1997.
[36] R. Shaw, *Wave Energy: A Design Challenge*. Ellis Horwood Ltd , Publisher, 1982.
[37] Y. Goda, *Random Seas and Design of Maritime Structures*, 2nd ed. World Scientific Publishing Company, 2000.
[38] A. Tabaei and M. Hariri Nokob, "Energy Capture Assessment of a Point Absorber Wave Energy Device," in *Proceeding of the World Renewable Energy Congress XI*, Abu Dhabi, UAE, 2010.
[39] R. H. Stewart, *Introduction to Physical Oceanography*, Online Book. Texas: Texas A&M University, 2005.

[40] T. Bjarte-Larsson and J. Falnes, “Laboratory experiment on heaving body with hydraulic power take-off and latching control,” *Ocean Engineering*, vol. 33, no. 7, pp. 847-877, May. 2006.
[41] A. F. de O. Falcão, “Phase control through load control of oscillating-body wave energy converters with hydraulic PTO system,” *Ocean Engineering*, vol. 35, no. 3-4, pp. 358-366, Mar. 2008.
[42] P. A. Martin and L. Farina, “Radiation of water waves by a heaving submerged horizontal disc,” Apr-1997. [Online]. Available: http://adsabs.harvard.edu/abs/1997JFM...337..365M. [Accessed: 21-Apr-2011].